The limits imposed in primate vision by transduction in cone photoreceptors

Juan M. Angueyra-Aristizábal

A dissertation
submitted in partial fulfillment of the
requirements for the degree of

Doctor of Philosophy

University of Washington
2014

Reading Committee:
Frederick M. Rieke,Chair
Bertil Hille
Greg Horwitz

Program Authorized to Offer Degree:

Physiology and Biophysics

University of Washington

Abstract

The limits imposed in primate vision by transduction in cone photoreceptors

Juan M. Angueyra-Aristizábal

Chair of the Supervisory Committee:
Professor Frederick M. Rieke
Department of Physiology and Biophysics

Experientially, our ability to visually perceive the world seems extraordinary, yet we keep asking ourselves: “could perception be better?” This dissertation centers around this question, exploring how the biophysics of photoreceptors impose constraints on the visual system and dictate certain aspects of perception. The first chapter explores the sources of noise in cone phototransduction and identifies open-close transitions of the cGMP-gated channels as a dominant source of noise. This noise source also escapes the light-adaptation mechanisms that control gain, establishing a particular scenario that determines the shape of threshold-vs.-intensity curves in single cones and ultimately in humans. The second chapter investigates how cones adapt during eye movements, uncovering that adaptation has at least two different time scales that influence the encoding of mean luminance and modulation around the mean luminance separately. This will lead to the construction of a biophysical model that only when endowed with two separate light-adaptation mechanisms is able to reproduce responses to a wide array of stimuli. It is my hope that this model can be used as a tool to explore the constraints imposed by cone signals on the rest of the retinal circuitry and that it can help clarify how computations are implemented in downstream neural circuits.

TABLE OF CONTENTS

LIST OF FIGURES

LIST OF TABLES

PREFACE

The work presented in Chapter 2 has been published as a separate manuscript:

Angueyra JM, Rieke F (2013) Origin and effect of phototransduction noise in primate cone photoreceptors. *Nature Neuroscience* 16 (11): 1692 - 1700

ACKNOWLEDGEMENTS

It is obvious that the work presented here wouldn't be possible without all the support, help and love I have received from people all around me.

Without the support of Enrico Nasi and Maria del Pilar Gomez, I would have never made it here. I told them once I felt indebted to them for all their mentorship and support; Enrico said that my debt would have to be repaid to the future generations. This is probably some of the best advice I have been given in my life.

Fred has been an incredible mentor, leading both through example and advice: when I joined the lab I really enjoyed learning how to record from Fred directly, then I was glad to do my own recordings and analysis, yet lately, I have a deep appreciation on the parallel work, which has been crucial to finish this dissertation in time. The rest of the lab is also impossible to replace: Mark Cafaro, Paul Newman and Shellee Cunnington support our work so much that we collapse whenever they are not around. Progress would have been impossible without all the teachings from Petri Ala-Laurila, the suggestion of Jon Cafaro to try the two-electrode recordings or Tony Azevedo's patience on hearing the smallest improvements and advances I made. Greg Schwartz, Will Grimes and Sid Kuo have taught me lot throughout the years both inside and outside the lab. Although the overlap with Max Turner, Ali Weber, Jacob Baudin and Phil Mardoum has been shorter, they probably have had to stand most of my continual yapping.

I think it has been more than a decade already that I have been following Felice Dunn around: from melanopsin-expressing cells, to primate photoreceptors and now to the immediate downstream synapse. It is always good to know that there's someone you'll never catch up to, and it was an honor to have her nearby for most of my PhD.

The whole Rieke lab but especially me is indebted to Mike Manookin, Christian Puller and Toni Haun. Without them, about a tenth of this work would have seen the light of day. I guess there goes another debt to the future generations…

Finally, thanks to all my family: Chantal, Ale and Tefilú las quiero mucho. And my "keep on swimming" fishy, Amber Trout, thanks for your support. I love you.

DEDICATION

To hindsight

Chapter 1
INTRODUCTION

One of the basic goals of sensory physiology is to understand how physical stimuli from our environment are turned into perception and used to guide behavior. In the case of vision, our everyday experience tells us that our sensory system is extraordinary: we are able to differentiate millions of colors, to discern the finest details in scenes and images, to detect events that occur in just fractions of a second, or to navigate the world under moonlight or in a clear sunny day. In a broad sense, this dissertation centers around how such sensitivity is achieved and how it is maintained as lighting conditions rapidly change. I will specifically tackle this question in primate cone photoreceptors, striving to elucidate how quantitative properties of the phototransduction process, like absolute sensitivity or light adaptation, impose constraints on visual processing. I propose that the results presented here establish a fair and biological basis to make comparisons with perception, and for some particular issues give clues on why our seemingly extraordinary daylight vision is not better.

1.1 Photoreceptors as a bottleneck for transmission of information

The history of modern vision science begins with the investigations into the physical basis of light, where a key finding was made by Newton in some of his earliest experiments on the subject. By dispersing light through prisms and recombining "individual rays", Newton revealed that a single hue could be recreated by the combination of very different subsets of narrow band lights (Shevell, 2003). Newton was convinced that this was a property of light itself, as during the XVIIth century, it was thought that rays of light fed directly into the optic nerve. But in fact, this is actually a property of our sensory system: in the very first stage of vision, three types of cone photoreceptors (figure 1.1a and b) detect light and produce signals that are relayed to the rest of the system. Each cone type has a wide and unique sensitivity to different wavelengths of light (figure 1.1c) (Baylor *et al.*, 1987) and can be classified as an L, M or S cone for being maximally sensitive to either long, middle or short wavelengths. The signals arising from the different cone types are then combined and compared in

particular ways by the visual system to create our perception of color (Shevell, 2003). The perception of a single hue can then be recreated with very different physical lights as long as photon absorptions are matched at the level of the three different types of cones. For this reason, the perception of color in humans can be described with a set of three axes (corresponding to photon absorptions in the L, M and S cones), a property known as trichromacy. Trichromacy is an example of a constraint imposed by photoreceptors themselves, that is then inherited by the rest of the system. Similarly, it is important to consider two additional constraints photoreceptors impose. First, noise that arises in photoreceptors sets a fundamental limit to our ability to sense changes in the visual world, as information that is lost early in the system is impossible to recover downstream. Second, photoreceptors can signal only over a limited range of inputs, a constraint that is mitigated by adaptational mechanisms that adjust gain to match the ambient lighting conditions.

From moonlight to clear summer days, ambient illumination spans a range of more that 8 log units, far surpassing the limited biological range of a single neuron: for example, retinal ganglion cells, which convey all visual information from the retina to the central nervous system by the transmission of action potentials, can modulate their firing rate by a factor of ~100. Thus, to maintain sensitivity and encode information, there is a need to adapt, and the visual system has set diverse physiological adaptation mechanisms throughout the visual system to be able to remain effective under the various challenges imposed by the environment (Rieke and Rudd, 2009). Adaptational mechanisms are first found in photoreceptors; like other neurons, photoreceptors have a limited range of signaling and adapt to avoid saturation while still maintaining high sensitivity to small stimulus deviations, so that the rest of the system receives meaningful inputs. Psychophysical studies have tried isolating the impact of adaptation in the detection of colored stimuli (for example, Stiles, 1953) and have found that over a wide variety of experimental conditions, the magnitude of adaptation depends linearly on the background illumination (known as Weber's law); this endows vision with constant responses to equal contrast, independently of the background illumination (a property known as 'contrast constancy') (Graham and Hood, 1992, Rovamo *et al.*,

1999). It is thought that the decreases in gain due light-adaptation in cone photoreceptors directly contribute to Weber adaptation and thus to contrast constancy.

In addition to the ability to accommodate a large range of inputs, visual sensitivity to subtle changes in inputs is quantitatively impressive. For example, humans and other primates are able to detect less than 5 nm changes in the wavelength of light (De Valois and Jacobs, 1968, Pokorny and Smith, 1970) even though the spectral sensitivities of cones themselves are wide (the half-width of cone spectral sensitivities ranges is approximately 100 nm) (figure 1C). Humans are also able to detect displacements in bars of light of just 1 minute of arc (about 1/20th the width of a single cone photoreceptor) (Klein and Levi, 1985), or perceive flashes of light that elicit merely ~5 photon absorptions per cone (or R*, as in 'receptor activations') in a pool of just ~10 cones (Donner, 1992, Koenig and Hofer, 2011) or even only 5 to 7 R* distributed across a pool of 500 rods (Donner, 1992). The main issue about these claims is that they are not grounded in a reliable base of comparison: detection is a task that depends on the signal-to-noise ratio and, without the presence of noise, even small spectral or spatial shifts should be able to be detected; for this reason, the detection of such stimuli is limited by the amount of noise in the system and not by the width of spectral sensitivities or the size of photoreceptors. In this specific context, the work I present here is a quantitative exploration of biophysical factors that may limit visual performance.

1.2 The physical limits of vision

Before considering the constraints imposed by neural processing, extrinsic factors have to be taken into account. Since the retina lines the back of the eye and photoreceptors are the outermost layer of the retina, light has to travel through several layers of optic media, including including the cornea, the lens, the vitreous humor, the macular pigment and the retina itself, before reaching photoreceptors. These optical elements are imperfect causing blur of images (Westheimer, 1977) and chromatic aberrations that significantly attenuate short wavelengths over long wavelengths (Stiles and Wyszecki, 1974, Sharpe *et al.*, 1998). After taking these into account, the number of photoreceptors involved in particular tasks can be calculated based on estimates of photoreceptor densities (Curcio and Sloan, 1992). Additionally, the quantal nature of

light imposes random Poisson fluctuations in photon absorptions, constituting an irreducible source of extrinsic noise capable of degrading the encoding of information. The impact of these and other constraints can be assessed under the framework of ideal observer analysis: “an ideal observer is a hypothetical device that performs a given task at the optimal level possible, given the available information and any specified constraints” (Geisler, 2011). Ideal observers provide a direct and quantitative measure of the relevance of each constraint and how these constraints interact with each other, and allow direct comparisons to the performance of real observers: a good match would suggest that real observers, and the neural circuits involved in this task, are using the available information in a near optimal way; discrepancies would suggest inefficiencies in processing.

Ideal observer analysis has been successfully used to relate physiological findings in individual rod photoreceptors to perception. In dark-adapted conditions, primate rods are extremely sensitive: their high gain produces significant responses to the absorption of a single photon (figure 1.2a) that are easily distinguished from the baseline electrical noise (figure 1.2b). Nevertheless, rhodopsin, the protein that absorbs photons and initiates the phototransduction process (see below), can spontaneously activate in darkness, creating discrete events (figure 1.2c) that are indistinguishable from a single photon response (figure 1.2e) at a mean rate of 0.0034 ± 0.008 R*/rod/s (Field and Rieke, personal communication). Given that macaque rods are about half the size of human rods, this rate is expected to be ~0.007 R*/rod/s in human rods. The detection of dim-flashes in dark-adapted humans is a noise limited task (Barlow, 1956) and the total amount of noise, quantified as an equivalent background illumination (and called ‘dark-light’), reaches a rate of ~0.011 R*/rod/s (Donner, 1992). The close agreement between these rates implies not only that noise in individual rod photoreceptors is the main limiting noise source for this task, but also that the downstream circuit is extremely efficient and adds very little extra noise. On the other hand, because of their high sensitivity, rods are particularly susceptible to extrinsic noise caused by quantal fluctuations, which becomes the dominant source of noise under a wide range of background illuminations, and dictates the signal-to-noise ratio of individual rods (Schneeweis and Schnapf, 2000); for this reason, when measured

across a range of background illuminations, thresholds follow a “square-root law” (i.e., due to Poisson statistics, the signal-to-noise ratio is proportional to the square root of the background illumination). The same square-root law (also known as “Rose-DeVries law”) is found when thresholds are measured perceptually for scotopic vision as a function of background illumination under various conditions (Stiles, 1953).

To apply ideal observer analysis to tasks with spatial information, an additional factor that is not part of neural processing *per se* has to be considered: the spacing between photoreceptors. In primates, a specialized region of the retina, called the fovea, has tightly packed cone photoreceptors in a hexagonal lattice; the density of cones then drops towards the periphery, as the space between cones is filled with rod photoreceptors (figure 1.1a) (Curcio and Sloan, 1992). The cone density directly determines spatial acuity, which is maximal at the fovea and progressively drops towards the periphery. For this reason, primates have developed complex and tightly regulated eye movements in order to direct the fovea to regions of interest, where spatial details can then be better assessed (Harris and Wolpert, 2006, Najemnik and Geisler, 2009, Kuang *et al.*, 2012). Furthermore, not all cone types have the same distribution across the retina. S-cones follow a different pattern from L and M cones, with their lowest density at the center of the fovea and representing only ~8-10% of the total number of cones in the peripheral retina (Curcio and Sloan, 1992) (figure 1.1a).

However, ideal observers based on models that include all the constraints previously mentioned find that photopic vision is not limited by these pre-retinal factors. For example, foveal spatial acuity in humans is on average 20-fold worse than it should be given photoreceptor spacing and pre-retinal factors (Banks *et al.*, 1987); wavelength discrimination is at least 10-fold worse (Zhaoping *et al.*, 2011). This suggests that these tasks are then limited by neural processing, raising the possibility that signaling and noise in cones act as bottlenecks for the transmission of information. Past work, however, has not provided a sufficiently complete characterization of cone noise to allow a reliable comparison to behavioral sensitivity.

1.3 A primer on the cone phototransduction cascade

In vertebrates vision starts by the transformation of light into neural signals, in a process called phototransduction, that takes place in the outer segment of rod and cone photoreceptors (figure 1.1b) (and in a subset of retinal ganglion cells which are not the subject of this dissertation).

Phototransduction is a G-protein cascade of biochemical reactions that amplifies the events triggered by the absorption of photons, resulting in an electrical signal. In darkness, photoreceptors continuously synthesize cyclic-GMP (cGMP) through a guanylate cyclase (GC) (figure 1.3a). The cGMP gates channels in the outer segment membrane, producing a standing inward current (called the dark-current). Upon activation by light, the opsin molecules change conformation and activate transducin molecules (which are G-proteins, and are noted as Gt). The α-subunit of transducin is then able to relieve inhibition from a phosphodiesterase (PDE). Activated PDE degrades cGMP and decreases its concentration. This leads to the closing of a fraction of the cGMP-gated channels (figure 1.3b) and thus to a decrease in the inward current (figure 1.3c). With regard to the membrane voltage, the dark current maintains photoreceptors in a depolarized state, and the light-induced reduction in current produces a hyperpolarization; subsequently, changes in voltage are translated into changes in the release of glutamate at the synapses located in pedicles of the photoreceptor inner segments, that are then detected by downstream neurons. In principle, any of these processes could introduce noise, resulting in a loss of information.

Strikingly, rods and cones have the same phototransduction scheme, but show very different behaviors (figure 1.4): (1) cones are less sensitive due to both lower gain and higher noise, (2) light-responses are significantly faster in cones, (3) spontaneous activation of opsin molecules is not a dominant source of noise in cones (Schneeweis and Schnapf, 1999). These differences have to arise from quantitative differences in the phototransduction cascade (absolute and relative concentrations of components, affinities, reaction kinetics, expression of regulatory proteins, etc.), and indeed some of these differences (like calcium metabolism) have been elucidated in cones from other species, mainly fish cones (Korenbrot and Rebrik, 2002, Kawamura and Tachibanaki, 2008), but others still remain a mystery (reviewed by Korenbrot, 2012).

1.4 Exploring the limits of vision through photoreceptors

Unlike neurons that are embedded in complex and multilayered circuits, it is simple to describe the specific task that primary receptors like cones perform: cones convert light information into electrical and chemical signals that can then be relayed to the downstream retinal circuitry. Nevertheless, the details on how this transformation is performed are important, as information lost in this stage is impossible to recover afterwards. A simple example of this stems again from color vision. As mentioned previously, humans are trichromats, but mutations that interfere with the expression of a single type of opsin from cones produce dichromacy (commonly known as color blindness) (Neitz and Neitz, 2011).

Fortunately, phototransduction is the most studied G-protein coupled cascades and we know with high accuracy details of its intricate workings, most of the components involved and how they interact with each other. On the other end of the spectrum, psychophysicists have been studying the perceptual limits of vision for several centuries, establishing insightful models to infer the inner working of the underlying neural circuits. Given the solid bridges that have been built between rod phototransduction and perception, and the solid pillars of models and ideal observers that include all pre-retinal factors, I propose that the study of cone photoreceptors in primates is an advantageous setting to again establish connections between neural elements and perception.

In the following chapters, I will strive to relate how the biophysics of photoreceptors impose constraints on perception. The first chapter explores the sources of noise in cone phototransduction and identifies open-close transitions of the cGMP-gated channels as a dominant source of noise. This noise source also escapes the light-adaptation mechanisms that control gain, establishing a particular scenario that determines the shape of threshold-vs.-intensity curves in single cones and ultimately in humans. The second chapter investigates how cones adapt during eye movements, uncovering that adaptation has at least two different time scales that influence the encoding of mean luminance and modulation around the mean luminance separately. This will lead to the construction of a biophysical model that only when endowed with

two separate light-adaptation mechanisms is able to reproduce responses to a wide array of stimuli. It is my hope that this model can be used as a tool to explore the constraints imposed by cone signals on the rest of the retinal circuitry and that it can help clarify how computations are implemented in downstream neural circuits.

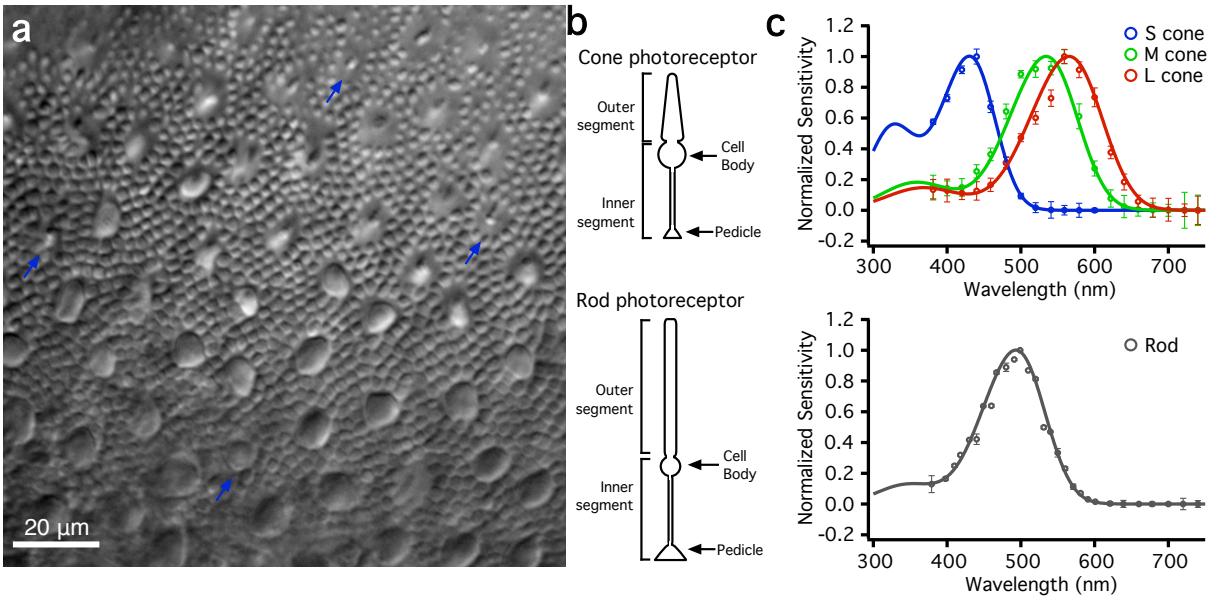

Figure 1.1 - Photoreceptors in the primate retina.

a. Rod and cone photoreceptors are intermingled in the peripheral primate retina. Cones cell bodies are easy to identify by their bigger size (~8 um in diameter) compared to the rod cell bodies and outer segments (~2 um) that surround them. Cone outer segments can be identified towards the top left corner of the image. S-cones have been identified previously and are marked with the blue arrows; the remaining 59 cones correspond to either L or M cones.

b. Diagram of cone and rod photoreceptor morphologies.

c. Primate cones can be classified based on their spectral sensitivities. **(Upper panel)** The cone spectral sensitivities {Baylor, 1987} have been reproduced and fitted with the Govadorvskii nomogram {Govardovskii, 2001}. L, M and S cones can be distinguished by the differences in wavelength of maximal sensitivity, but all cone types are sensitive to a wide range of wavelengths. **(Lower panel)** The rod spectral sensitivity {Baylor, 1984} has also been reproduced and fit with the Govadorvskii nomogram for comparison.

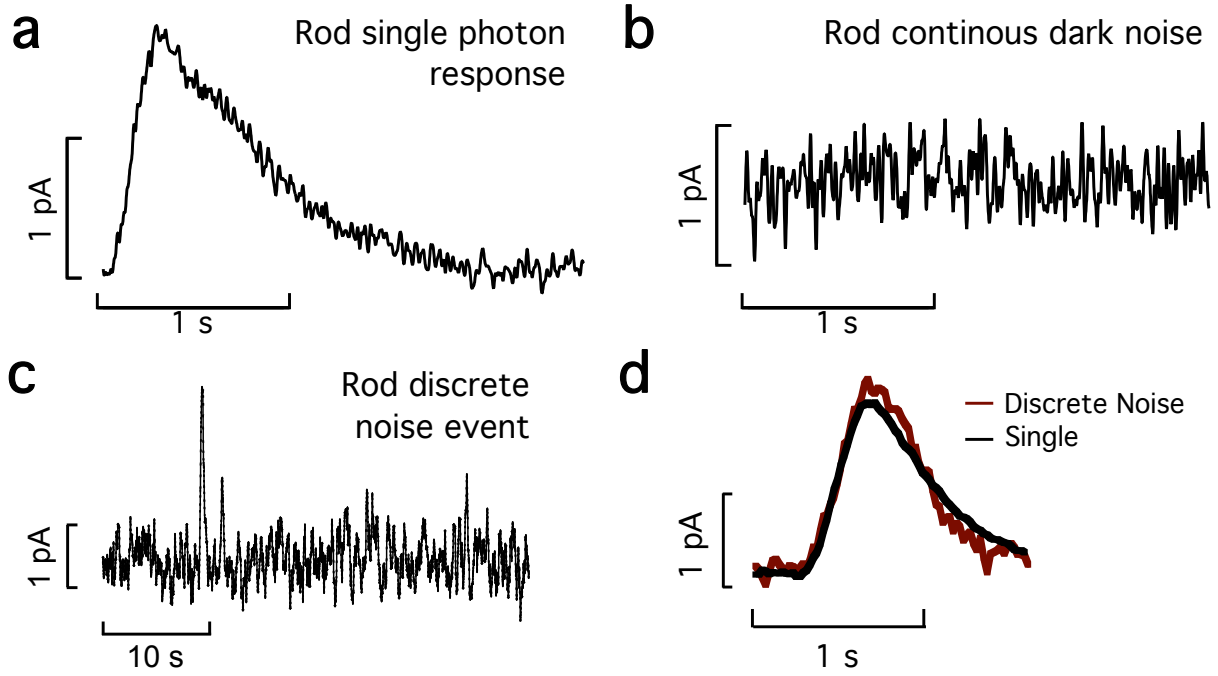

Figure 1.2 - Primate rods are extremely sensitive due to a high gain and low noise.

a. Estimated single photon current response in a primate rod (obtained by dividing the average response to a dim flash by the flash intensity) in darkness

b. Corresponding current dark noise.

c. The spontaneous activation of rhodopsin produces discrete noise events that are indistinguishable from a single photon response.

d. Example of discrete noise event in a different primate rod and overlay with the estimated single photon response.

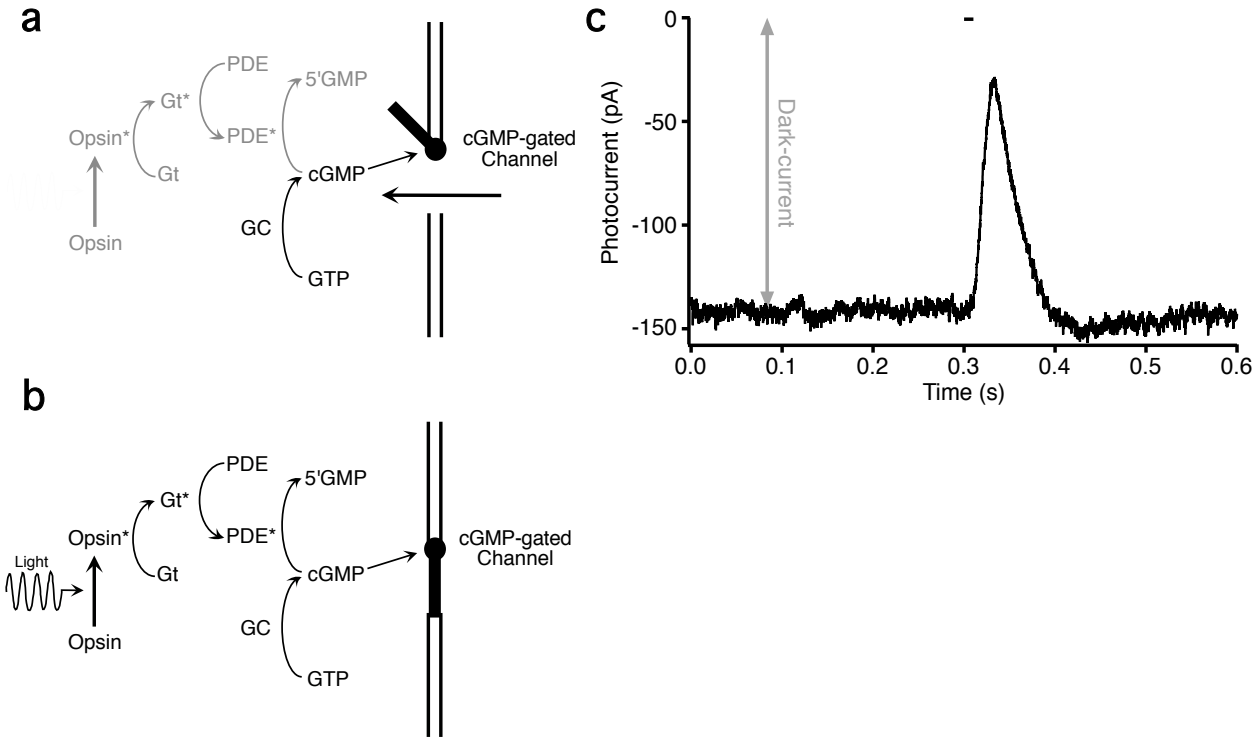

Figure 1.3. Phototransduction cascade in primate rods and cones.

a. In darkness, unstimulated photoreceptors maintain an inward dark-current through cGMP-gated channels that are maintained open by continual production of cGMP by a guanylate cyclase (GC).

b. Upon light-stimulation, opsin molecules are activated through the absorption of photons and activate the G-protein transducin (Gt), which in turns activates a phosphodiesterase (PDE), leading to a reduction in cGMP concentration and closure of channels in the membrane.

c. Example of cone response to a brief flash. Recording from a single-cone under voltage-clamp, shows a dark-current of ~148 pA, which is transiently reduced by stimulation with a brief (10 ms) flash of light.

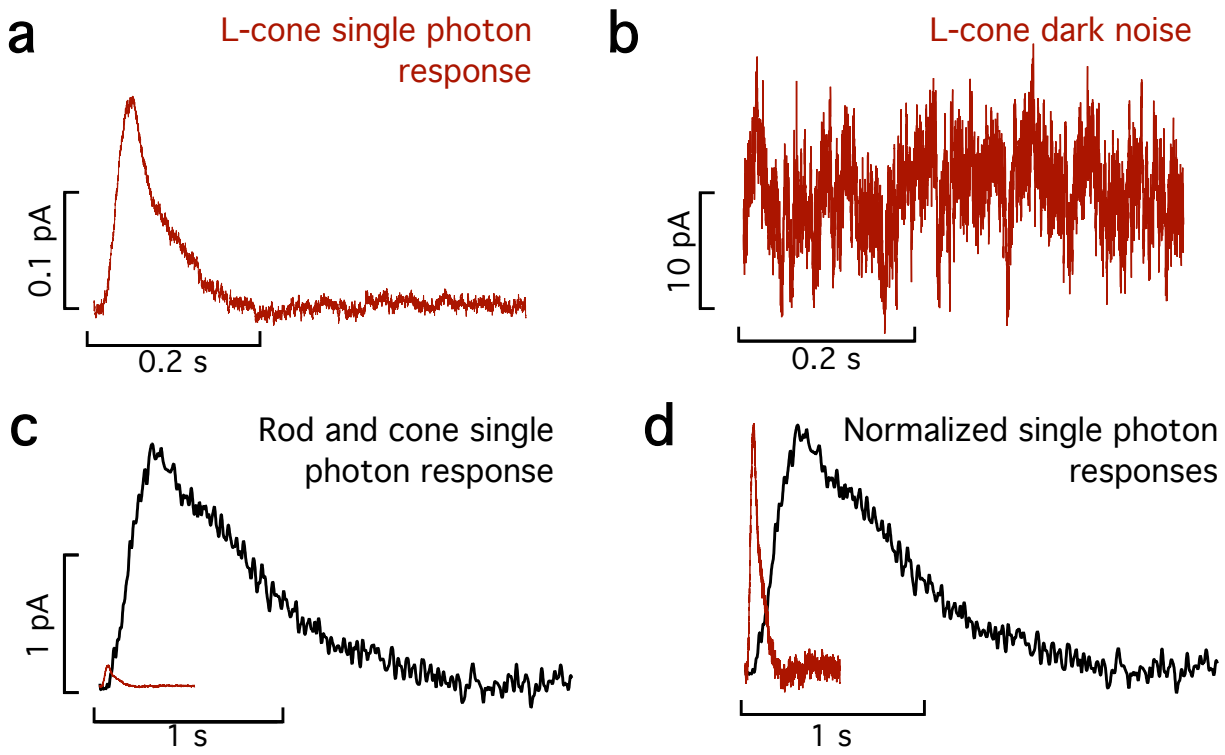

Figure 1.4 - Primate cones have a lower gain, higher noise and faster kinetics than primate rods.

a. Estimated single photon response in darkness in a primate L-cone.

b. Corresponding current dark noise. Notice the 100-fold difference in scales between (a) and (b).

c. Single photon responses from example cone in (a) (red trace) and from example rod (Figure 1.2) (black trace) have been overlaid to highlight the differences in gain evidenced by the differences in peak amplitude.

d. The same single photon responses have been normalized to highlight the faster kinetics in cones.

Chapter 2

Origin and Impact of Phototransduction Noise in Primate Cone Photoreceptors

2.1 Summary

Noise in the responses of cone photoreceptors sets a fundamental limit to visual sensitivity, yet the origin of noise in mammalian cones and its relation to behavioral sensitivity are poorly understood. Our work here on primate cones improves understanding of these issues in three ways. First, we find that, unlike the noise in rod photoreceptors, cone noise is not dominated by spontaneous photopigment activation or by quantal fluctuations in photon absorption but instead by other sources, namely channel noise and fluctuations in cGMP. Second, we find that adaptation in cones, unlike that in rods, affects the photosignal and the noise differently. This difference helps explain why thresholds for rod- and cone-mediated signals have different dependencies on background light level. Third, past estimates of noise in mammalian cones are too high to explain behavioral sensitivity. Our measurements indicate a lower level of cone noise, and thus help reconcile physiological and behavioral estimates of cone noise and sensitivity.

2.2 Introduction

Daylight vision relies on high sensitivity to subtle changes in the spatial pattern, contrast and chromaticity of light inputs. Noise in the responses of cone photoreceptors sets a fundamental limit to such sensitivity. Our goal here was to improve understanding of the magnitude, origin and properties of noise in the responses of primate cones, particularly with regard to the implications of cone noise for visual function.

Rods and rod vision provide a useful point of comparison. In darkness, noise in rods consists of occasional photon-like events originating from the spontaneous activation of the photopigment rhodopsin and continuous fluctuations originating from spontaneous activity of other components of the phototransduction cascade (Baylor *et al.*, 1980, Baylor *et al.*, 1984, Rieke and Baylor, 1996). The low level of rod noise permits detection of single absorbed photons (Fu and Yau, 2007). Dark-adapted behavioral sensitivity approaches limits set by rod noise and statistical fluctuations

associated with the division of light into discrete quanta (Donner, 1992, Field *et al.*, 2005). The similarity of rod and behavioral noise requires that the retinal readout of rod responses operate efficiently, a constraint that has guided investigation of the underlying circuitry (Field *et al.*, 2005). In the presence of dim backgrounds, quantal fluctuations dominate rod noise. As a consequence, the detection sensitivity of rod responses scales with the square root of the background light level (Schneeweis and Schnapf, 2000); this scaling is in close agreement with the classic Rose-DeVries region of behavioral threshold-versus-intensity curves (Rieke and Rudd, 2009).

The situation is much less clear for cones and cone-mediated vision. While the rate of spontaneous activation of cone photopigments is much higher than that of rhodopsin (Rieke and Baylor, 2000, Fu *et al.*, 2008), the kinetics of noise in primate cones suggests that most noise originates downstream of the photopigment (Schneeweis and Schnapf, 1999). However, measured noise in primate cones is too high to account for behavioral sensitivity, suggesting that one or both estimates are in error (Donner, 1992). Thus the impact of cone noise remains unclear. Further, over a wide range of backgrounds, behavioral thresholds for cone-mediated vision increase linearly with background (the classic Weber region), a property important for coding contrast independently of background light level (Fechner, 1860). It is unclear, however, how the Weber region relates to the background dependence of cone signal and noise.

Here we characterize signal and noise in primate cone photoreceptors and their dependence on background light level. Our measures of cone noise and detection thresholds are considerably lower than past estimates, helping reconcile cone physiology with behavioral measures of the sensitivity of cone vision. Further, we find that adaptation affects cone signal and cone noise very differently, providing a natural explanation for the Weber region of behavioral threshold-versus-intensity curves.

2.3 Methods

2.3.1 Tissue, cells and solutions

We made electrophysiological recordings from primate retinas (*Macaca fascicularis*, *nemestrina* and *mulatta* of either sex, ages 3 – 19 yrs) in accordance with the Institutional Animal Care and Use Committee at the University of Washington. We

obtained retina through the Tissue Distribution Program of the Regional Primate Research Center. We performed most enucleations under pentobarbital anesthesia. After enucleation, we rapidly separated the retina-pigment epithelium-sclera complex (< 5 min) from the anterior segment, drained the vitreous humour, and dark-adapted the retina for 1h in warm (32^{o} C) Ames medium bubbled with a mixture of 95% CO_2 - 5% O_2. We performed all subsequent procedures under infrared (> 900 nm) light. For recording, we separated a small piece of retina (~4mm^2) from the pigment epithelium and mounted it photoreceptor side up on a poly-lysine coated coverslip (BD Biosciences) forming the floor of a recording chamber. We continually superfused retinas with warm (~31° - 33° C) oxygenated Ames medium. Treatment with DNase I (Sigma-Aldrich) (30 units in ~250 µL of Ames for 4 min) facilitated access to the photoreceptor outer segments. For rod suction recordings, we shredded small pieces of retina with bent needles and transferred them to a recording chamber (Field and Rieke, 2002).

2.3.2 Recordings

We measured cone signals using whole-cell voltage-clamp recordings (holding potential –70 mV) with an internal solution containing (in mM): 133 potassium aspartate, 10 KCl, 10 HEPES, 1 $MgCl_2$, 4 ATP, 0.5 GTP; pH was adjusted to 7.2 with NMG-OH and osmolarity was ~280 mOSM. The internal solution did not contain any calcium buffer (or calcium), as even low concentrations of calcium buffer caused the light response to become increasingly biphasic during the course of a recording (not shown). We recorded rod photocurrents using suction electrodes as described previously (Field and Rieke, 2002). Holding potentials have been corrected for a –10 mV liquid junction potential.

In experiments with 8'-bromo-cyclic-GMP (8'Br-cGMP) we used modified internal solutions lacking ATP and GTP and supplemented with various concentrations of 8'Br-cGMP (from 0 µM to 200 µM). We added IBMX (final concentration of 1 mM) dissolved in DMSO (final DMSO concentration was less than 0.1%) to HEPES-buffered Ames and included it in a puffer pipette. For control experiments we used the same solution without IBMX.

We acquired data using Axoclamp 200B or Multiclamp 700B amplifiers. We low-pass filtered recorded currents at 3 kHz and digitized the data at 20 kHz. We analyzed recorded data through custom routines in Matlab (The Mathworks); we calculated power spectra using built-in fast Fourier transformations and represented them as two-sided power spectral densities (in pA^2/Hz). We excluded from analysis cones that showed unusually rapid run-down of light responses, low sensitivity or short-lived recordings. Sensitive cones had holding currents of at least 150 pA (up to 400 pA), and peak responses to bright flashes of similar magnitude.

2.3.3 Light Stimulation

We delivered light stimuli from blue, green and red LEDs (peak wavelengths 470, 510 and 640 nm), which permitted quick identification of cone types. The stimuli illuminated a ~150 µm diameter area centered and focused on the recorded cone. We converted photon densities (photons/μm^2) to R*/photoreceptor using a collecting area of 0.6 µm (Baylor *et al.*, 1984), previously measured cone spectral sensitivities (Baylor *et al.*, 1984) and the LED spectra.

2.3.4 Two-electrode technique

We performed two-electrode recordings by sealing simultaneously onto a single cone cell body with both a recording electrode and a drug delivery electrode. After breaking into the cell with the first electrode, we obtained a baseline recording to assess noise and light response in less than 30 s (in voltage-clamp mode). Then we obtained access with the drug delivery electrode (in current clamp with no holding current) while maintaining the original recording.

2.3.5 Fitting of cone noise

The fits to the noise power spectra presented in Figure 2.1 correspond to empirical fits (and are not unique) constructed as the sum of the power spectrum of the estimated single-photon response and two separate Lorentzian functions. In Fourier-space, a single Lorentzian function had the following form:

$$L(\omega) = \frac{\alpha}{1+\left(\frac{\omega}{\omega_c}\right)^2} \tag{2.1}$$

where ω_c corresponds to the corner frequency (frequency at which the power has dropped by half) and α is a scaling constant. We obtained fits on a logarithmic scale through built-in Matlab routines (*nlinfit* and *lsqcurvefit*) and we assessed the fits through the coefficient of determination (R^2). The fit to the average noise from L and M cones at a background illumination of 5000 R*/s (n=6) did not depart from the measured data by more than 1 SEM, and the R^2 value for the fit was 0.90, with 5 fitting parameters (Figure 2.1d). The same observation holds for the average noise from L and M foveal cones recorded in darkness (n=7) with an R^2 value for the fit of 0.99 (Figure 2.1e).

2.3.6 Pharmacology

We determined significance in pharmacological experiments through two-tailed, Student's t-tests with $\alpha \leq 0.05$, by integrating the average power ratios across the specified frequency ranges. We did not perform a sample size calculation prior to experiments. We chose sample sizes to either establish statistical significance of the effects measured (Figures 2.3 and 2.4) or to provide relative tight confidence intervals on key parameters. Also, we did not have a sufficient number of samples to test whether the data used in t-tests were indeed normally distributed.

For the experiments involving 8'Br-cGMP (Figure 2.3) we compared each concentration to the experiments lacking 8'Br-cGMP (Figure 2.2f-j) across the 10 – 600 Hz frequency range and found significant differences for all concentrations (18 μM: n = 10, p = 0.0009, df = 14; 27 μM: n = 4, p = 0.022, df = 8; 100 μM: n = 3, p = 0.00002, df = 7; 200 μM: n = 2, p = 0.001, df = 6; retinas were derived from 12 different animals).

For the experiments involving IBMX (n = 10) (Figure 2.4) we compared the changes in noise to those produced by a vehicle solution lacking IBMX (n = 4) and found significant differences for both the 10 – 50 Hz (p = 0.0004, df = 12) and the 100 –

600 Hz frequency range (p = 0.0068, df = 12; retinas were derived from 2 different animals).

2.3.7 Signal and noise adaptation

We restricted analysis of signal and noise adaptation to cones that passed several criteria: stability of the holding current, good and stable access resistance, minimal run-down of the light response and high sensitivity to flashes in darkness. We assume that the most sensitive cones we record from are most representative of cone responses *in vivo*. We estimated single-photon responses by delivering non-saturating flashes at a given background, then averaging the resulting responses and scaling by the nominal flash intensity; this procedure provides a linear estimation of the gain of the light response. We then fitted these estimated single-photon responses with the following equation (modified from Baylor, Nunn and Schanpf, 1984):

$$f(t) = \alpha \left(\frac{(\frac{t}{\tau_{rise}})^4}{1 + (\frac{t}{\tau_{rise}})^4} \right) \times e^{-\left(\frac{t}{\tau_{decay}}\right)} \times cos(\frac{2\pi t}{\tau_{osc} + \omega}) \tag{2.2}$$

We obtained the best-fit values through automatic fitting routines in Matlab (*nlinfit* and *lsqfit*). The changes in signal gain were virtually the same whether fits or directly estimated single-photon responses were used, but the fits eliminated uncertainty due to limited data, especially on mid- to high- frequencies (50 – 600 Hz). The changes in signal gain were also near identical when using the response integral or peak amplitude rather than relying on power spectra.

The fits for the changes in signal gain and noise had only a few parameters, which made them suitable for maximum likelihood estimation; the fit values reported are then the most likely values, bounded by values for which the likelihood of the fit dropped to 2.5% of the maximum, i.e. the 95% confidence intervals (95% CI). The fitting of the changes in cone noise (Figure 2.5c,d) did not include the highest background, where isolation of the remaining noise from noise in saturating light was difficult and unreliable.

The changes in high-frequency cone noise were described by a modified Weber-Fechner function, with an additional free exponent (η) that would accommodate a different slope:

$$\frac{\sigma_B}{\sigma_D} = \frac{1}{\left(1 + \frac{I_B}{I_0}\right)^{\eta}} \tag{2.3}$$

Here σ_B corresponds to the standard deviation of the noise at a given background (in pA), σ_D to the standard deviation of the noise in darkness (also in pA), I_B is the intensity of the background (in R*/s), and I_0 is the background illumination that halves the noise. The best fits for the data in Figure 2.5g were I_o = 17,500 R*/s (95% CI: 15,600 - 19,400 R*/s) and η = 0.29 (95% CI: 0.28 - 0.31).

2.3.8 Threshold-versus-Intensity Curves

We obtained threshold versus intensity curves shown in Figure 2.7 by first calculating the spectrum of the signal-to-noise ratio (SNR) for each background, using the corresponding power spectra of the signal and of the noise and assuming a 200 ms integration time. We then integrated the square root of this SNR spectrum between 0.4 and 8 Hz for rods and between 3 and 600 Hz for cones. The inverse of this integral corresponds to the flash response that matches the noise at a given background, expressed in R*, or in other words, the just-detectable flash or detection threshold.

2.4 Results

The results below are divided into four parts. First, we describe empirical properties of noise in primate cone photoreceptors. Second, we manipulate the cone phototransduction cascade to identify where noise originates. Third, we determine how light-adaptation affects the signal and noise of primate rod and cone responses. Fourth, we explore how detection thresholds for rod and cone responses depend on background light level.

2.4.1 Cone noise exhibits several distinct temporal components

We started by characterizing the amplitude and kinetics of noise in the responses of primate cones. Past work indicates that cones are noisy, with most noise originating downstream of the photopigment in the transduction cascade (Schneeweis and Schnapf, 1999). We felt it was important to begin with similar experiments given that past measures of cone noise exceed the noise inferred from behavior (Donner, 1992) and the properties of cone noise are a foundation for the remainder of the work here.

We recorded the current responses of voltage clamped long- (L) or middle- (M) wavelength sensitive cones to brief 100% contrast flashes (producing ~50 opsin isomerizations or R* per cone) in the presence of a moderate background (Figure 2.1a). Individual responses to such flashes are difficult to distinguish from baseline noise, but the response can be uncovered by averaging multiple trials (Figure 2.1a). The recorded current fluctuations include noise arising in the outer segment, noise arising from conductances in the inner segment, and noise produced by the recording itself (instrumental noise). Exposing cones to a near-saturating light step closed most of the cGMP-gated channels in the cone outer segment, decreasing the recorded current and markedly decreasing the current fluctuations (Figure 2.1a,b). Instrumental noise and noise from (voltage-clamped) inner segment conductances should not be light dependent; these sources account for the most of the noise remaining in bright light.

We characterized noise by calculating average power spectra from stretches of data without flashes (see Methods). Assuming that outer segment and inner segment/ instrumental noise are independent, we isolated outer segment noise by subtracting the spectrum in bright light from that in moderate light (Figure 2.1c). This process underestimates the total outer segment noise since bright light did not fully suppress the current; such errors were small, however, as the subtracted noise was 20 – 100-fold smaller than that measured in darkness or in the presence of moderate steady light (Figure 2.1b). In the remainder of this chapter, outer segment cone noise has been isolated similarly.

Both noise generated within the cone phototransduction cascade (intrinsic noise) and noise generated by quantal fluctuations in photon absorption (extrinsic noise) contribute to outer segment noise; extrinsic noise follows Poisson statistics and is

absent in complete darkness (see below). Assuming linearity of the cone response, both extrinsic noise and noise from spontaneous pigment activation should have a power spectrum similar to that of the cell's dim flash response (Figure 2.1c). As has been described previously (Schneeweis and Schnapf, 1999), cone noise instead extended to much higher frequencies, indicating a substantial contribution from events with faster kinetics than the single photon response. By recording noise in voltage clamp, we characterized outer segment noise up to high temporal frequencies (600 Hz); noise spectra had three clear components and were fit empirically as the sum of a low frequency component with the shape of the dim flash response, and two Lorentzian functions with distinct corner frequencies (equation 2.1). Adequate fits were obtained on a single-cell basis (Figure 2.1c), or by averaging over a population of L and M cones recorded with the same background illumination (5,000 R*/s; Figure 2.1d). Based on these fits, the lowest frequency component accounted for ~30% of the total variance, which corresponds to the maximal fraction of noise that could be attributed to both spontaneous and background opsin activation.

To separate phototransduction noise from extrinsic noise, we repeated these experiments in complete darkness, targeting foveal cones to eliminate possible contributions from rod photoreceptors coupled to cones via gap junctions (Hornstein *et al.*, 2005). The average noise showed less power at low frequencies (Figure 2.1e), such that at most ~10% of the total current variance could be attributed to spontaneous opsin activation. L and M cones exhibited similar noise, and in particular did not show the ~50-fold difference that would be expected from the scaling of spontaneous opsin activation rates with wavelength (Luo *et al.*, 2011).

Although most low-frequency noise is not associated with spontaneous pigment activation, we can still define a rate of pigment activation that would produce an equivalent level of noise. Experiments described below indicate that this equivalent dark noise is ~600 R*/s, substantially lower than previous estimates (Schneeweis and Schnapf, 1999). First, however, we describe experiments identifying the sources of noise within the transduction cascade.

2.4.2 Two dominant sources of noise: pharmacology

Rod and cone photoreceptors share the same basic phototransduction scheme, yet their light responses differ considerably in sensitivity and kinetics. Does noise in rods and cones also differ in origin? Rod noise is dominated by early events in phototransduction - namely spontaneous activation of rhodopsin and phosphodiesterase (PDE) (Baylor *et al.*, 1980, Baylor *et al.*, 1984, Rieke and Baylor, 1996). As shown below, cone noise is instead dominated by open/close transitions in the cyclic-GMP-gated channels and fluctuations in the cyclic-GMP (cGMP) concentration.

Because the low- and mid-frequency noise components we identified overlap spectrally (Figure 2.1), we focused on a frequency range (up to 20 Hz) that includes contributions mainly from both low- and mid-frequency components, and a range (100 – 600 Hz) that is dominated by the high-frequency component. To maximize sensitivity to pharmacological manipulations that produced modest changes in the phototransduction cascade, we used two approaches to compare noise before and after drug application in single cells: (1) We delivered membrane-impermeable drugs (specifically 8‘-bromo-cyclic-GMP or 8’Br-cGMP) using a two-electrode recording technique in which both a recording electrode and a drug-delivery electrode were sealed onto a single cone cell body. After attaining whole-cell mode with the recording electrode and getting baseline measurements of noise and light response (in under 30 s), we achieved access with the drug-delivery electrode and monitored noise and signal as the drug was introduced into the cytoplasm. (2) We delivered membrane-permeable drugs (specifically 3’-isobutyl-1’-methylxanthine or IBMX) using a puffer pipette located near the cone outer segment after recording baseline noise and light response.

2.4.2.1 Control experiments for two-electrode recordings

Because the two-electrode technique has not been used previously in cones, we started by checking for artifactual changes in noise. We first used a normal internal solution in both electrodes, keeping the phototransduction cascade as intact as possible (Figure 2.2a). Rupturing the membrane occluding the tip of the second electrode did not significantly change the holding current (Figure 2.2b) or the kinetics or amplitude of the light response (Figure 2.2c); some alterations in noise were apparent (Figure 2.2c,d).

We summarized the results across cells by computing the ratio, at each temporal frequency, of the noise spectra before and after rupturing the membrane at the tip of the second electrode (Figure 2.2e); only pharmacological manipulations that produced changes in this ratio larger than the control case were deemed significant.

Next, we tried to eliminate all outer segment noise pharmacologically. Since all phototransduction noise sources ultimately cause fluctuations in the current flowing through the cGMP-gated channels, one way to eliminate noise is to promote depletion of the internal cGMP, which will in turn cause the cGMP-gated channels to close (Figure 2.2f). Cyclic-GMP is produced from GTP by the guanylate cyclase (GC); thus we omitted GTP from the electrode solution. We also omitted ATP since transfer of its high-energy phosphate can produce GTP (Swarup and Garbers, 1983). Hydrolysis of cGMP by phosphodiesterase (PDE) via activation of the G-protein transducin (Gt) requires considerably lower concentrations of GTP than cGMP-synthesis (Rieke and Baylor, 1996, Rieke and Baylor, 1998), and hence will contribute to reducing the cGMP concentration. As expected, currents steadily decreased (i.e. cGMP-gated channels closed) in two-electrode recordings using internal solutions lacking both ATP and GTP (Figure 2.2g); this was accompanied by a loss in the light response and a marked attenuation of the current fluctuations (Figure 2.2h). The decrease in noise spanned all relevant frequencies (Figure 2.2i,j) and had the same spectral characteristics as the decrease in noise seen during exposure to near-saturating light steps, which also close the cGMP-gated channels (compare to Figure 2.1a,b). We obtained similar results in recordings with single electrodes filled with a solution lacking ATP and GTP (n = 3, data not shown).

This pharmacological manipulation served several purposes: (1) it confirms that most of the noise in our recordings originates in the cone outer segment; (2) it shows that manipulation of the electrode solutions can affect the phototransduction cascade; and, (3) the current changes provide a basis for evaluating experiments in the next section, where a synthetic agonist will be used to open the cGMP-gated channels.

2.4.2.2 Channel noise

The two-electrode experiments described in this section, isolated noise produced by cGMP-gated channels. Changes in cGMP were again suppressed by omitting ATP and GTP from the internal solution, and cGMP channels were activated with 8'Br-cGMP, a potent agonist of the cGMP-gated channels (Figure 2.3a). Because 8'Br-cGMP is also poorly hydrolyzed by PDE, it suppresses activity within the PDE arm of the phototransduction cascade. Introduction of 8'Br-cGMP through the second electrode would ideally occur only after the internal cGMP has been depleted, but this process can take up to 5 min (Figure 2.2g), and long recordings with two electrodes are technically difficult. Instead, we relied on shorter experiments in which we compared different concentrations of 8'Br-cGMP with the case where 8'Br-cGMP is absent (Figure 2.2j).

We empirically determined appropriate concentrations of 8'Br-cGMP and found that modest concentrations (27 μM) 'rescued' (and even overshot) the loss in holding current (Figure 2.3b) and noise (Figure 2.3c) produced by the omission of GTP and ATP alone (compare to Figure 2.2g-i). Under these conditions, measured currents and noise were dominated by channels opened by the added 8'Br'cGMP. Higher concentrations produced a further increase in holding current (Figure 2.3d) and noise (Figure 2.3e) compared to baseline.

The concentration of 8'Br-cGMP in the outer segment slowly approaches a steady level for two reasons: (1) the 8'Br-cGMP is delivered in the inner segment, and has to diffuse to the outer segment; (2) PDE can still hydrolyze 8'Br-cGMP at a slow rate. Together, these issues cause a slow drift in holding current and artifactual increases in noise below 10 Hz, making changes in noise in that frequency range uninterpretable. Thus, we focus on changes in noise between 10 and 600 Hz (Figure 2.3c,e).

With activity of the transduction cascade suppressed, activation of the cGMP-gated channels produced fluctuations in current extending from low frequencies to at least 600 Hz. The increase in noise scaled with the concentration of 8'Br-cGMP (Figure 2.3f). High frequency noise was similar under control conditions (without 8'Br-cGMP) and with a concentration of 8'Br-cGMP that matched the initial dark current (Figure 2.3b,c). These results indicate that the component of cone noise that extends from low

to high temporal frequencies originates from gating transitions in the cGMP-gated channels.

2.4.2.3 Noise due to fluctuations in cGMP

The experiments described above indicate that channel fluctuations produce noise extending from low to high temporal frequencies. To test for other sources of low- to mid-frequency noise, we puffed the membrane-permeable PDE inhibitor IBMX onto the outer segments of voltage-clamped cones. IBMX has two effects: (1) it decreases baseline hydrolysis of cGMP, leading to an increase in [cGMP] and further opening of cGMP-gated channels; and, (2) it decreases the fluctuations in [cGMP] produced by dark activation of any of the transduction components upstream of (and including) PDE (Figure 2.4a). We performed recordings in darkness to avoid extrinsic noise and again focused on frequencies above 10 Hz to avoid artifacts induced by current drift.

Inhibition of PDE, as expected, reversibly increased the holding current (Figure 2.4b) and slowed the light response (not shown). This was accompanied by an increase in high-frequency noise, consistent with an increase in channel noise; additionally, noise in the low- to mid- frequency range (10-50 Hz) decreased (Figure 2.4c,d). These changes in noise were significantly different from those elicited by puffing a vehicle solution lacking IBMX (Figure 2.4e) in the two relevant frequency ranges.

This experiment serves several purposes. First, it corroborates the 8'Br-cGMP experiments, showing that the opening of extra cGMP-gated channels leads to an increase in high-frequency channel noise. Second, it unveils a noise source that is suppressed when PDE is inhibited and that, therefore, normally causes fluctuations in the cGMP concentration. Notably, this noise source has significant power in the 10-50 Hz range, where opsin noise makes little or no contribution (see Figure 2.1c-e). This noise component resembles continuous noise in rods (Rieke and Baylor, 1996) and fish cones (Holcman and Korenbrot, 2005) (see Discussion).

2.4.3 Impact of adaptation on photoreceptor signal and noise

The impact of adaptation on detection of light stimuli depends on how it alters both signal and noise. For example, over a substantial range of backgrounds rod signal

and noise are equally affected by adaptation, such that the signal-to-noise ratio is independent of adaptation (Schneeweis and Schnapf, 2000). As a consequence, the detection threshold for such backgrounds is limited by the Poisson statistics of photon absorption. This provides a simple explanation for the Rose-DeVries regime of behavioral threshold-versus-intensity curves, since the standard deviation of a Poisson process scales as the square root of the mean (Rieke and Rudd, 2009). Since much of cone noise originates late in the transduction cascade, it may be less affected by adaptation than cone signals. Thus, the relationship between photoreceptor adaptation and behavioral threshold-versus-intensity curves may be fundamentally different for rods and cones. The experiments described in the next two sections show that this is indeed the case.

2.4.3.1 Rods

We begin by characterizing the dependence of rod signal and rod noise on background. While our overall conclusions are consistent with previous studies (Schneeweis and Schnapf, 2000), we felt that inclusion of the rod data was important to provide a direct comparison with the cone results described below.

We measured rod flash responses and noise across a range of backgrounds using suction electrodes (Field and Rieke, 2002). Background light abbreviated and decreased the amplitude of the estimated single-photon response (Figure 2.5a); adaptation was pronounced for backgrounds exceeding 8 R*/s. To facilitate direct comparison, we quantified both signal and noise adaptation using spectral analysis. We integrated the power spectra of fits to the single-photon response at each background (Figure 2.5a) between 0.5 and 4 Hz (Figure 2.5b) and quantified changes in gain as the square root of this integral, normalized by the value in darkness (Figure 2.5c). Gain changes were well described by a Weber-Fechner function:

$$\frac{\gamma_B}{\gamma_D} = \frac{1}{\left(1 + \frac{I_B}{I_0}\right)} \tag{2.4}$$

where γ_B corresponds to the gain at a given background (in pA/R*), γ_D to the gain in darkness (in pA/R*), I_B to the intensity of the background illumination (in R*/s) and I_0 to the background illumination that halves the gain. The best fit for I_0 was 7.1 R*/s (95% confidence interval (CI) 6.0 – 8.2 R*/s).

We estimated rod noise at the same backgrounds. Noise in darkness was low and composed of continuous noise and rare discrete events (not present in the example trace) (Figure 2.5d). Noise increased in dim backgrounds due to current fluctuations produced by random photon absorptions (Figure 2.5d,e), peaking at ~8 R*/s with an almost 5-fold increase relative to darkness; higher backgrounds produced a subsequent decrease in noise (Figure 2.5f).

These changes in noise can be predicted based on two assumptions: (1) intrinsic phototransduction noise and extrinsic noise are independent and additive; and, (2) extrinsic and intrinsic noise are subject to the same light adaptation mechanism that affects the rod signals. These assumptions are summarized in the following equation, in which the first term represents the decrease in noise produced by adaptation and the second term corresponds to the increase in noise produced by quantal fluctuations in photon arrival:

$$\frac{\sigma_B}{\sigma_D} = \frac{1}{\left(1 + \frac{I_B}{I_0}\right)} \times \sqrt{\left(1 + \frac{I_B}{I_D}\right)} \tag{2.5}$$

Here σ_B corresponds to the standard deviation of the noise at a given background (in pA), σ_D to the standard deviation of the noise in darkness (also in pA), I_B is the intensity of the background (in R*/s), I_D represents the intrinsic noise expressed as an equivalent “dark light” (in R*/s; see Donner, 1992), and the half-desensitizing background, I_0 = 7.1 R*/s, was fixed from fits to the background-dependence of signal gain (Figure 2.5c and equation 2.4). The best fit was found for a dark light I_D of 0.062 R*/s (95% CI: 0.055 -

0.070 R*/s), which is within 30% of previously published values (Schneeweis and Schnapf, 2000). The success of this simple model indicates that, in agreement with previous work (Schneeweis and Schnapf, 2000), rod signals and noise are subject to the same adaptational mechanisms. This in turn is simply explained if rods are dominated by extrinsic noise across a wide range of backgrounds.

2.4.3.2 Cones

Adaptation affected cones quite differently, as a substantial component of cone noise evaded adaptation. To quantify signal adaptation in cones we estimated and fit single-photon responses (Figure 2.6a) and calculated their power spectra (Figure 2.6b); gain was estimated as the square root of the integrated power between 1 and 10 Hz across a range of backgrounds (Figure 2.6c). Changes in gain were also well described by a Weber-Fechner function (equation 2.4); the best fit was found for a half-desensitizing background of I_0 = 4,500 R*/s (95% CI: 3,900 - 5,200 R*/s), consistent with previous work[19].

We estimated cone noise at the same backgrounds by integrating power spectra across a low (1 – 10 Hz) and a high (100 – 600 Hz) frequency range (Figure 2.6d,e) and calculated the square root of these integrals across backgrounds (Figure 2.6f). The background dependence of low- and high-frequency noise differed. Like rod noise, low-frequency cone noise initially increased and then began to fall with further increases in background (Figure 2.6f). This initial increase was modest (compare to the rod noise in Figure 2.5f) and apparent only for backgrounds exceeding 1,000 R*/s. The dependence of low-frequency noise on background could be fit with equation 2.5, using the half-desensitizing background for the signal gain (I_0) derived above (4,500 R*/s) and a best-fit value for an equivalent dark light of I_D = 620 R*/s (95% CI: 480 - 835 R*/s). Thus, low-frequency cone noise can also be described as the sum of intrinsic and extrinsic noise, both subject to the same adaptational mechanism as the cone signals. High-frequency cone noise, however, was little affected by dim backgrounds and began to decline only at much higher backgrounds (Figure 2.6f). Furthermore, this decline in high frequency noise was shallow and not proportional to the inverse of the background. Changes in noise at intermediate frequencies (20 – 100 Hz) showed a mixed behavior.

The background dependence of rod and cone signals and noise differed in two important ways. First, rod dark noise is ~100 times smaller than the backgrounds required for substantial adaptation, whereas in cones this ratio is less than a factor of 10. Second, the majority of noise in rods is affected by adaptation, whereas a large component of noise in cones evades adaptation. Taken together, these factors mean that extrinsic noise contributes significantly to total cone noise only over a narrow range of backgrounds (~1,000 – 5,000 R*/sec). At lower backgrounds, cone noise is dominated by intrinsic noise from both cGMP fluctuations and cGMP channels, whereas at higher backgrounds the relative contribution of noise from cGMP channels increases.

2.4.4 Threshold vs. background behavior of rod and cone responses

The differences in the effect of adaptation on signal and noise in rods and cones predicts differences in the background-dependence of detection threshold. This in turn relates to how adaptation in the photoreceptors could contribute to behavioral threshold-versus-intensity curves.

We calculated detection thresholds, defined as the flash strength (in R*) required to match the noise in a 200 ms integration time at a given background, from the power spectra exemplified in Figure 2.5 and 2.6. First, we calculated the signal-to-noise ratio (SNR) as a function of frequency by dividing the signal power spectrum by the noise power spectrum; this SNR spectrum has very little power at high frequencies, and such frequencies contribute negligibly to detection. We integrated the SNR spectrum between 0.4 and 8 Hz for rods and 3 and 600 Hz for cones; the inverse of the square root of this integral corresponds to the detection threshold.

Rod and cone detection thresholds have a different dependence on the intensity of the background illumination (Figure 2.7), as the shape of these curves is determined by how both signal and noise adapt. Given that rod noise and signal adapt identically, the rod thresholds follow (derived from equations 2.4 and 2.5):

$$Threshold_B = \left(\sqrt{1 + \frac{I_B}{I_D}}\right) \times Threshold_D$$

(2.6)

with I_D = 0.062 R*/s (derived from the noise adaptation in Figure 2.5f). This curve closely follows the Poisson statistics of the background illumination for backgrounds exceeding the dark noise.

Cone threshold increased more steeply with background. The lack of dependence of threshold on backgrounds < 1000 R*/s reflects the relatively high cone dark noise, which obscures extrinsic noise. Once signal gain is reduced by adaptation (I_B > 4,500 R*/sec), cone channel noise, which is relatively unaffected by adaptation, becomes dominant and hence the increase in threshold directly reflects the decreased signal gain. Thus, the curve is well fit with a Weber-like function:

$$Threshold_B = \left(1 + \frac{I_B}{I_0}\right) \times Threshold_D$$

(2.7)

with a best fit for the threshold-doubling background of I_0 = 11,700 R*/s (95% CI: 7,700 - 24,400 R*/s). The dark threshold was $Threshold_D$ = 10.9 R*/cone (95% CI: 6.8 - 14.9 R*/cone).

Rod and cone threshold *vs.* intensity curves differed in at least three ways. First, as expected, the absolute threshold was higher in cones due to noise sources that preclude detecting absorption of single photons. Second, higher backgrounds were required to produce changes in cone threshold compared to rod threshold. Third, cone thresholds scaled linearly with background (i.e. Weber behavior), whereas rod thresholds scaled with the square root of the background (i.e. Rose-DeVries behavior).

2.5 Discussion

Our aim was to improve understanding of the origin and functional impact of noise in the responses of primate cone photoreceptors. Our experiments support three main conclusions: (1) most cone noise originates downstream of the photopigment, with a sizable component from gating transitions in cGMP-gated channels; (2) cone noise and detection threshold are consistent with those inferred from behavior; and, (3) much

of cone noise evades adaptation, helping provide a simple explanation for how the classic Weber region of behavioral threshold-versus-intensity curves could originate. We discuss these points below.

2.5.1 Origin of cone noise

We identified two primary sources of noise in the responses of primate cones: gating transitions in the cGMP-gated channels produce noise that extends from low to high temporal frequencies (up to 600 Hz), and fluctuations in the concentration of cGMP produce noise restricted to low to mid temporal frequencies (below 50 Hz).

Several observations indicate that most of the noise from cGMP fluctuations is not generated by dark activation of the cone opsin: (1) the dim flash response, which reflects the activity directly caused by opsin activation, lacks significant power at frequencies above 10 Hz (Figure 2.1c-e), whereas noise due to cGMP fluctuations extends well beyond 10 Hz (Figure 2.4c); (2) the spontaneous isomerization rate of the L-cone opsin, estimated by its expression in mouse rods (Fu *et al.*, 2008), is ~10 R*/s , a factor of ~60 less than the rate needed to match the cone dark noise measured here; and, (3) preliminary recordings in S cones (where opsin noise should be almost negligible since short-wavelength sensitive opsins are very stable in comparison to middle- and long-wavelength sensitive opsins) (Rieke and Baylor, 2000, Luo *et al.*, 2011) show very similar dark noise to that reported here for L and M cones. Thus, fluctuations in the cGMP concentration originate from another source - such as activity of the non-isomerized photopigment due to chromophore dissociation (Kefalov *et al.*, 2005), spontaneous transducin activation, or spontaneous PDE activation. Spontaneous PDE activation accounts for substantial noise in the responses of rods (Rieke and Baylor, 1996), salamander S cones (Rieke and Baylor, 2000), and fish cones (Holcman and Korenbrot, 2005) and thus is a likely culprit here.

2.5.2 Impact of cone noise on retinal signals

In the guinea-pig retina, sensitivity has been assessed by measuring thresholds for the detection of contrast modulation at cone light-levels. Comparison of the sensitivity of the cone-mediated signals at several retinal locations indicates that most

noise originates early in the retinal circuitry (Borghuis *et al.*, 2009). Specifically, a substantial loss of sensitivity was observed between photon capture in the cones and the responses of horizontal cells, consistent with noise intrinsic to the cones or their output synapse. Smaller, but still substantial, losses in sensitivity were observed between horizontal and ganglion cells, consistent with a source of additional noise within the retinal circuitry. Recordings from primate midget and parasol ganglion cells indicate that most noise in their synaptic inputs at cone light levels originates from the cones and has more rapid kinetics than the cone light response (Ala-Laurila *et al.*, 2011). These past studies highlight the importance of noise intrinsic to cones or their output synapses. Our results, particularly the high level and rapid kinetics of the cone noise, suggest that much of the noise limiting the sensitivity of the cone-mediated output signals from primate retina originates in the cone transduction cascade itself.

2.5.3 Bridging physiological and behavioral estimates of cone noise and sensitivity

How close does cone vision come to limits imposed by cone noise? The answer to this question is an important constraint on the retinal and cortical circuits that read out the cone signals. However, noise estimates derived from behavioral sensitivity are substantially lower than past measures of noise in primate cones (Donner, 1992); this discrepancy has hindered our understanding of the relationship between retinal mechanisms and the sensitivity of cone-mediated behavior.

Recent behavioral work provides the lowest estimates of threshold and dark noise for cone vision (Koenig and Hofer, 2011), indicating that humans can detect ~200 photons delivered at the cornea or equivalently ~2 – 5 R*/cone in a region containing ~10 cones. Assuming that cone signals are pooled linearly, sensitivity should improve as the square root of the number of cones conveying the signal; thus the inferred single-cone threshold estimate in darkness would be 6 – 15 R*, agreeing well with our single cone dark thresholds (7 – 15 R*) (Figure 2.7).

Dark-noise estimates require additional assumptions about spatial pooling and integration time of the visual system. Assuming spatial pooling across the entire area of the flash and an integration time equal to the flash duration (34 ms), behavioral sensitivity indicates a dark noise of 180 – 550 R*/s (Koenig and Hofer, 2011).

Uncertainties in foveal cone density could further extend this range. This is again consistent with our estimate of ~600 R*/s. Thus, our measures of cone sensitivity and dark noise are consistent with behavior, providing a potential resolution to a long-standing discrepancy. Assuming the most sensitive cones we recorded from (Figure 2.6 and 2.7) are similar to those *in vivo*, our results leave little room for noise or inefficiencies introduced by the circuits reading out the cone signals.

2.5.4 Impact of adaptation on threshold vs. intensity curves

The impact of adaptation on the detection of sensory signals depends on how it affects both signal and noise. This is a key issue for how adaptational mechanisms relate to the rich history of measurements of the dependence of behavioral threshold on background light level (Donner, 1992, Schneeweis and Schnapf, 2000, Field *et al.*, 2005, Rieke and Rudd, 2009).

Consistent with past work (Schneeweis and Schnapf, 2000), we found that adaptation equally affected rod signal and noise. This observation, along with the low level of intrinsic noise in rods, caused the detection threshold to be limited by extrinsic noise from quantal fluctuations in photon arrival across a wide range of backgrounds. Since quantal fluctuations follow Poisson statistics, the noise they contribute increases as the square root of the background intensity, consistent with the psychophysical Rose-deVries region of rod vision (Barlow, 1956). It has been difficult to explain why cone vision does not similarly exhibit a clear Rose-deVries region; our results here suggest that the lack of a prominent Rose-deVries region occurs because extrinsic noise makes a relatively small contribution to cone noise except in a narrow range of backgrounds.

Classic work shows that cone-mediated behavioral thresholds across a wide range of backgrounds increase linearly with increases in background intensity (Weber-law behavior) (Fechner, 1860). The mechanistic basis of this behavior, however, is unclear. The gain of cone signals decreases proportionally with backgrounds (Tranchina *et al.*, 1984, Schnapf *et al.*, 1990, Burkhardt, 1994, Schneeweis and Schnapf, 1999). This decrease in gain, together with a post-adaptation, background-independent source of noise, could explain Weber-law behavior (Donner *et al.*, 1990). Here, we find that

channel noise in cones accounts for a substantial fraction of cone dark noise; furthermore, channel noise is little affected by adaptation and thus becomes the dominant source of cone noise across a broad range of backgrounds. The weak dependence of channel noise on background and the decrease in gain of cone signals proportional to the background gives rise to an extended region over which the cone detection threshold follows Weber behavior. If noise downstream of the cones is small relative to cone noise, adaptational mechanisms in the retinal circuitry (Demb, 2008, Rieke and Rudd, 2009) would equally affect signal and noise. In this case, human threshold-*vs.*-intensity curves could be dominated by the signal and noise adaptation properties of individual photoreceptors. A complete explanation of human threshold versus intensity curves will require understanding where gain controls operate relative to key sources of noise in the circuit.

2.6 Acknowledgements

We thank Chip Asbury, Felice Dunn, Greg Horwitz and Raunak Sinha for helpful comments on an earlier version of the paper, and Mark Cafaro and Paul Newman for excellent technical assistance. Color scales were developed and made freely available for Matlab by Matteo Niccoli. Support provided by HHMI (FR) and the National Eye Institute of the National Institutes of Health (R01EY11850 to FR). Retinas were obtained from the Washington National Primate Research Center at the University of Washington, NIH grant RR00166, and from the National Center for Research Resources and the Office of Research Infrastructure Programs (ORIP) of the National Institutes of Health through Grant Number P51 OD 010425. The content is solely the responsibility of the authors and does not necessarily represent the official views of the National Institutes of Health.

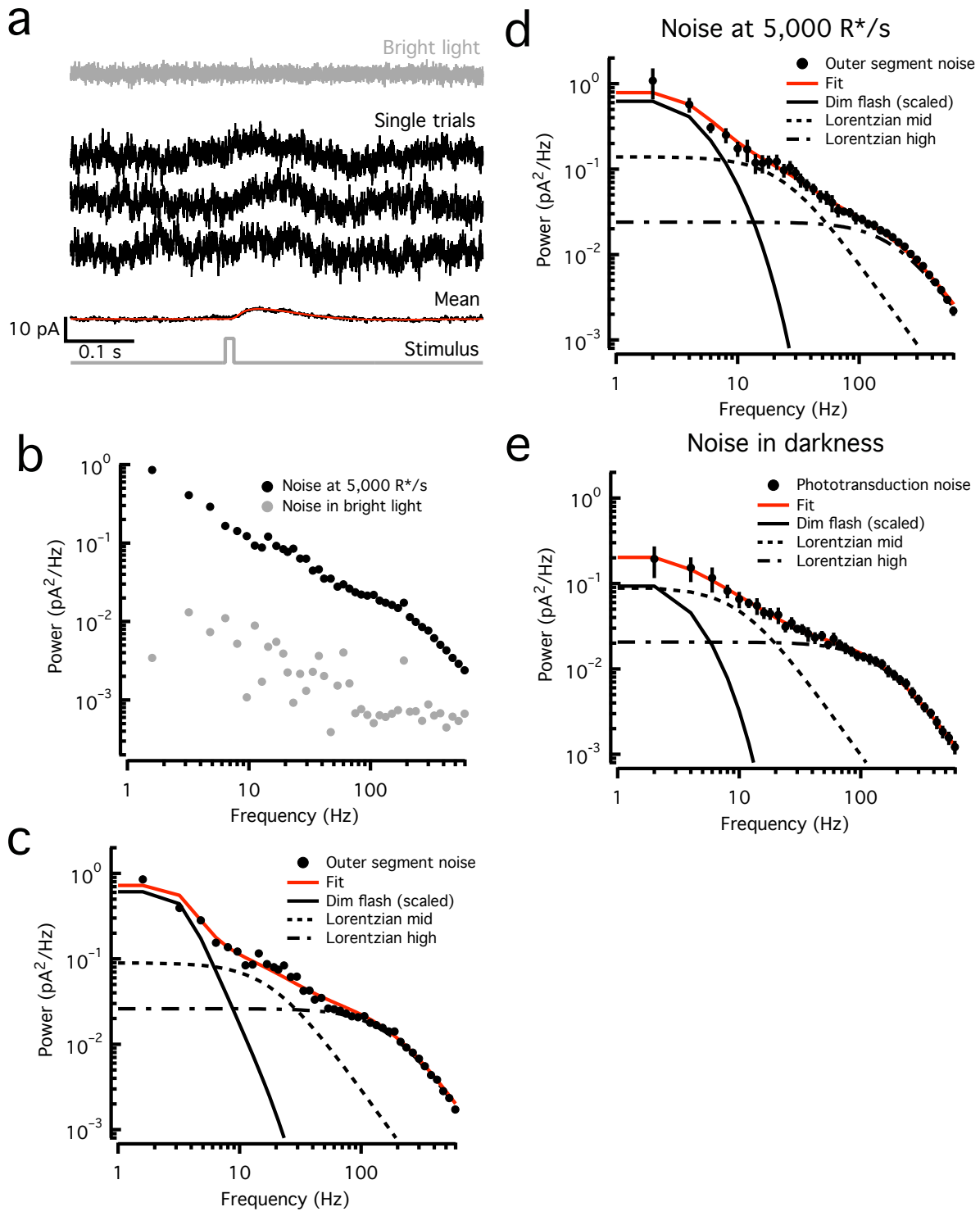

Figure 2.1 - Temporal components of cone outer segment noise

a. Cone current responses to 10 ms flashes producing ~50 opsin activations (R*) delivered on a 5,000 R*/s background (black traces). The mean of ~50 responses is at

the bottom, fitted (red) with equation 2.2 with the following parameters: $\alpha = 0.1993$, $\tau_{rise} = 20.2$ ms, $\tau_{decay} = 75.6$ ms, $\tau_{osc} = 397.1$ ms and $\phi = -79.5$ degrees. Current recorded in bright light is at the top (gray trace).

b. Power spectra of noise in constant and bright light from cone in (a).

c. Power spectrum of the outer segment cone noise (black circles, noise in background minus that in saturating light from b) and fit (red trace) obtained by summing a scaled version of the power spectrum of the fitted average dim flash response and two Lorentzian functions (equation 2.1) with distinct corner frequencies (18 Hz and 170 Hz) (black lines).

d. Average outer segment cone noise measured at 5,000 R*/s (n = 6, black circles, mean ± SEM) and fit as in (c) (red trace). Corner frequencies of Lorentzian functions are 24 Hz and 200 Hz.

e. Average outer segment cone noise measured in darkness from foveal cones (n = 7, black circles, mean ± SEM) and fit as in (c) (red trace). Corner frequencies of Lorentzian functions are 10 Hz and 150 Hz.

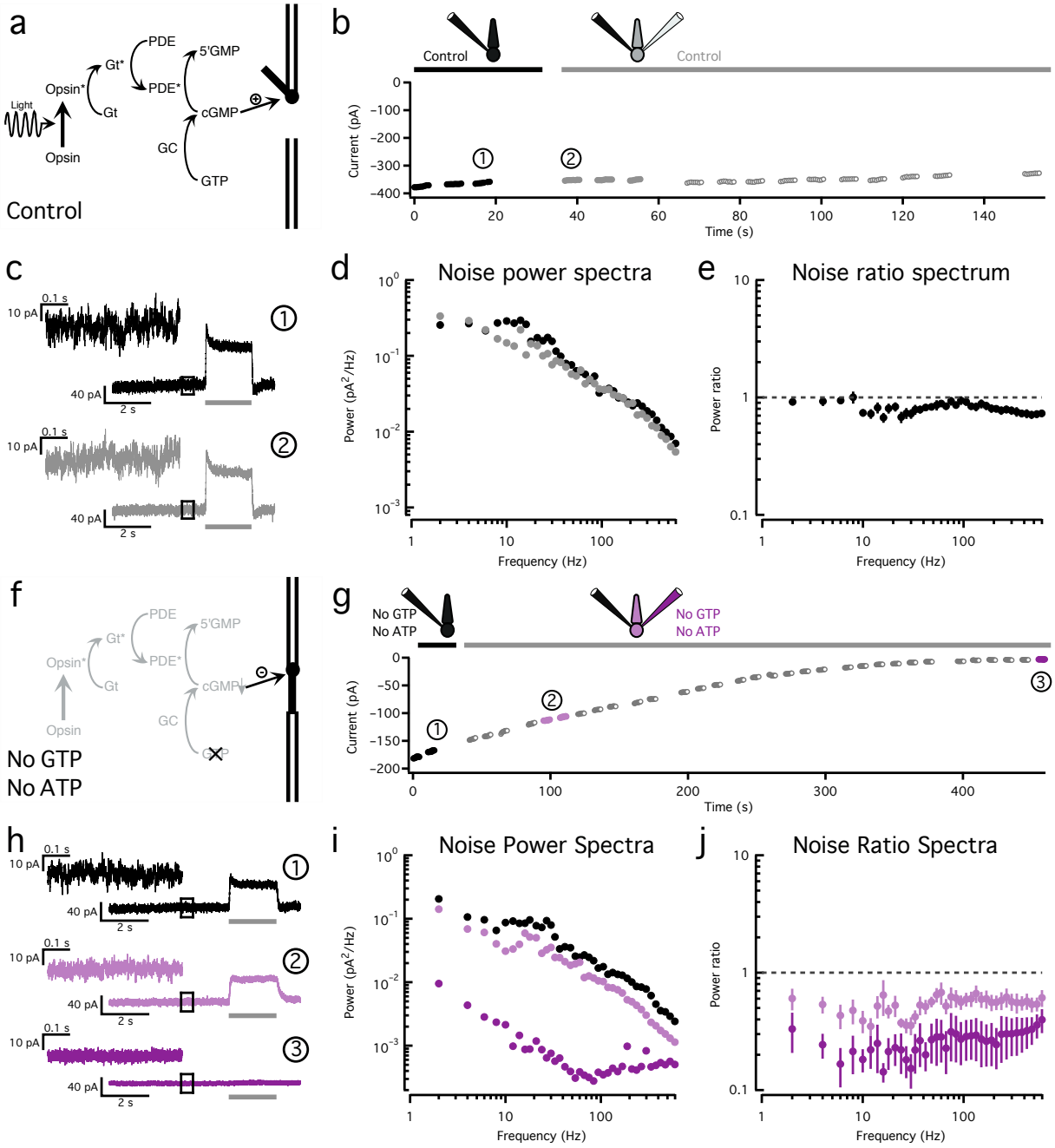

Figure 2.2 - Two-electrode recordings allow pharmacological manipulation of cone phototransduction

a. Phototransduction cascade. Light-activated Opsin activates transducin (Gt), which then activates phosphodiesterase (PDE). Active PDE reduces the cyclic-GMP (cGMP) concentration, closing membrane channels. Cyclic-GMP is restored by guanylate cyclase (GC).

b. Changes in holding current before (black) and after (gray) introduction of a second electrode; both electrodes contained control internal solution. Filled black and gray circles represent 500 ms stretches of noise used to calculate the spectra in (d).
c. Light responses and noise before (black) and after (gray) introduction of the second electrode (time points noted in (b)). Upper left shows expanded examples of noise used to calculate the power spectra in (d).
d. Power spectra before (black circles) and after (gray circles) the introduction of the second electrode.
e. Average (± SEM, n = 16) ratio between power spectra calculated before and after introduction of the second electrode.
f. Omission of both ATP and GTP from the internal solution shuts down the phototransduction cascade, causing cGMP-gated channels to close.
g. Changes in holding current during a two-electrode recording in which both electrodes contained a solution lacking ATP and GTP. Filled black and purple circles represent 500 ms stretches of noise used to calculate the spectra in (i).
h. Examples of light responses and noise recorded before (black) and after (purple) the introduction of a second electrode (time points noted in (g)).
i. Power spectra before (black) and after (purple) the introduction of the second electrode.
j. Average (± SEM, n = 6) ratio of power spectra before and after the introduction of the second electrode. Conditions as in (g).

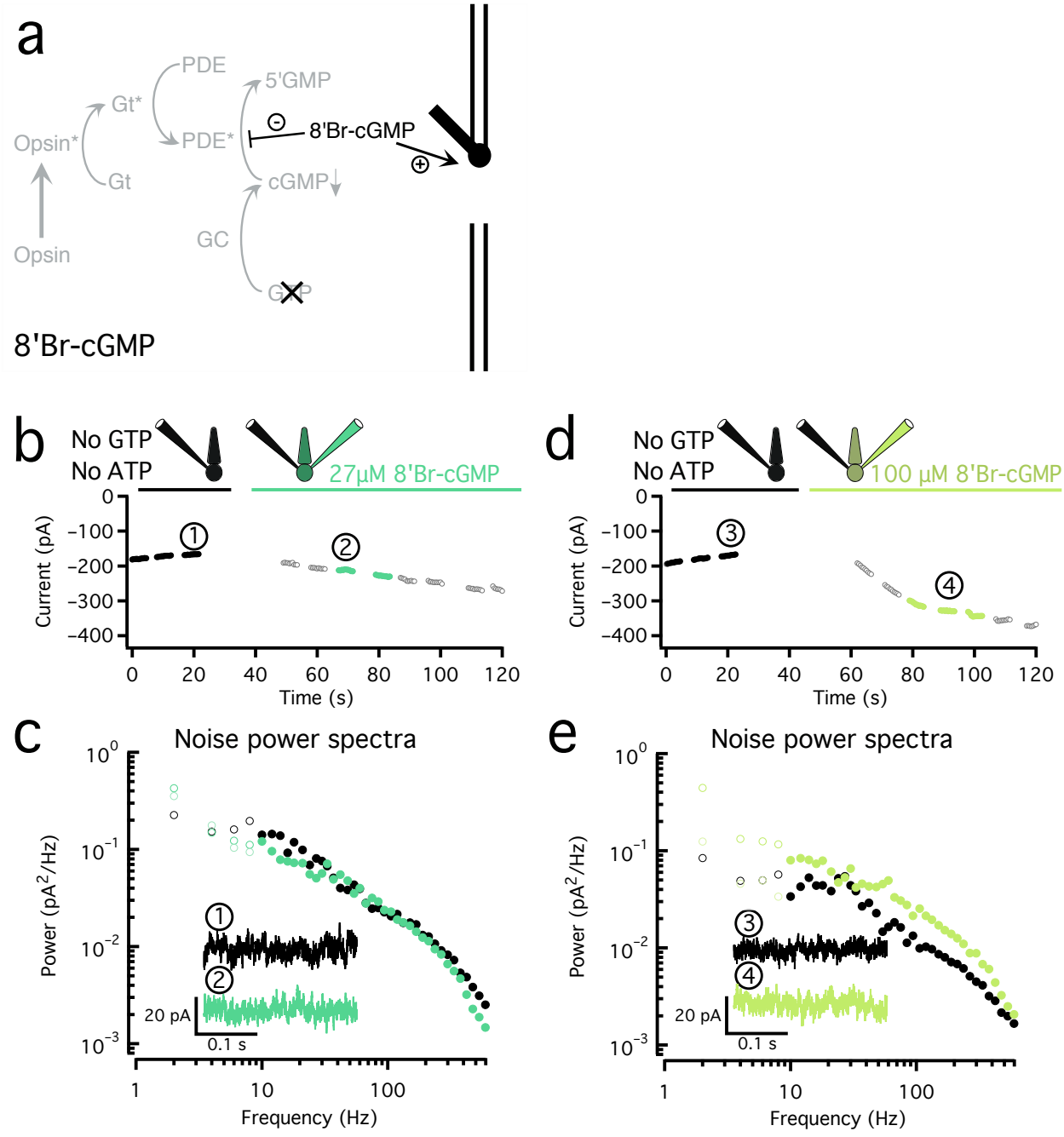
a
PDE
5'GMP
Gt*
Opsin*
PDE*
8'Br-cGMP
Gt
cGMP
GC
Opsin
8'Br-cGMP
b
No GTP
No ATP
27μM 8'Br-cGMP
Current (pA)
Time (s)
d
No GTP
No ATP
100 μM 8'Br-cGMP
Current (pA)
Time (s)
c
Noise power spectra
Power (pA²/Hz)
Frequency (Hz)
20 pA
0.1 s
e
Noise power spectra
Power (pA²/Hz)
Frequency (Hz)
20 pA
0.1 s

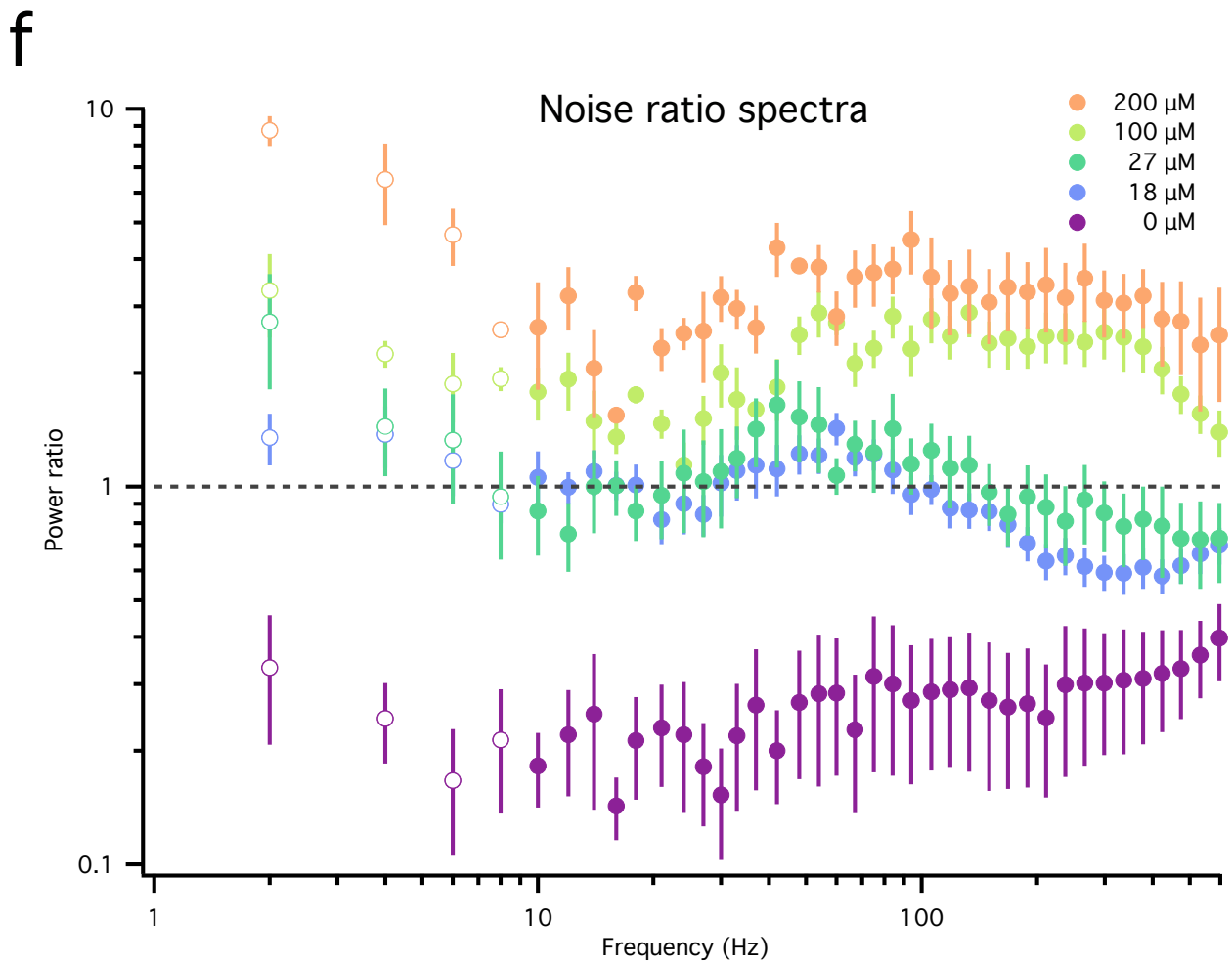

Figure 2.3 - High frequency noise arises from open/close transitions in the cGMP-gated channels

a. Channel noise was separated from sources causing fluctuations in [cGMP] by suppressing cGMP synthesis by omitting ATP and GTP from the internal solutions in a two-electrode recording. Different concentrations of the cGMP-channel agonist 8'-bromo-cyclic-GMP (8'Br-cGMP) were added to the second electrode.

b. Changes in holding current before (black) and after (green) the introduction of a second electrode containing 27 µM 8'Br-cGMP. The filled black and green circles represent 500ms stretches of noise used to calculate the spectra in (c).

c. Average noise power spectra for the cone in (B) before (black) and after (green) the introduction of a second electrode containing 27 µM 8'Br-cGMP. Insets show example noise traces in each condition corresponding to (1) and (2) in (b).

d and e. Same as in (b) and (c) for an 8'Br-cGMP concentration of 100 µM.

f. Average (± SEM) ratio of power spectra before and after introduction of 8'Br-cGMP. The color scale corresponds to the concentration of 8'Br-cGMP (18 μM: n = 10; 27 μM: n = 4; 100 μM: n = 3; 200 μM: n = 2). Changes in noise below 10 Hz are unreliable due to slow drift in the measured current and are displayed as open circles. The increase at high frequencies (100 Hz – 600 Hz) is significant across all concentrations.

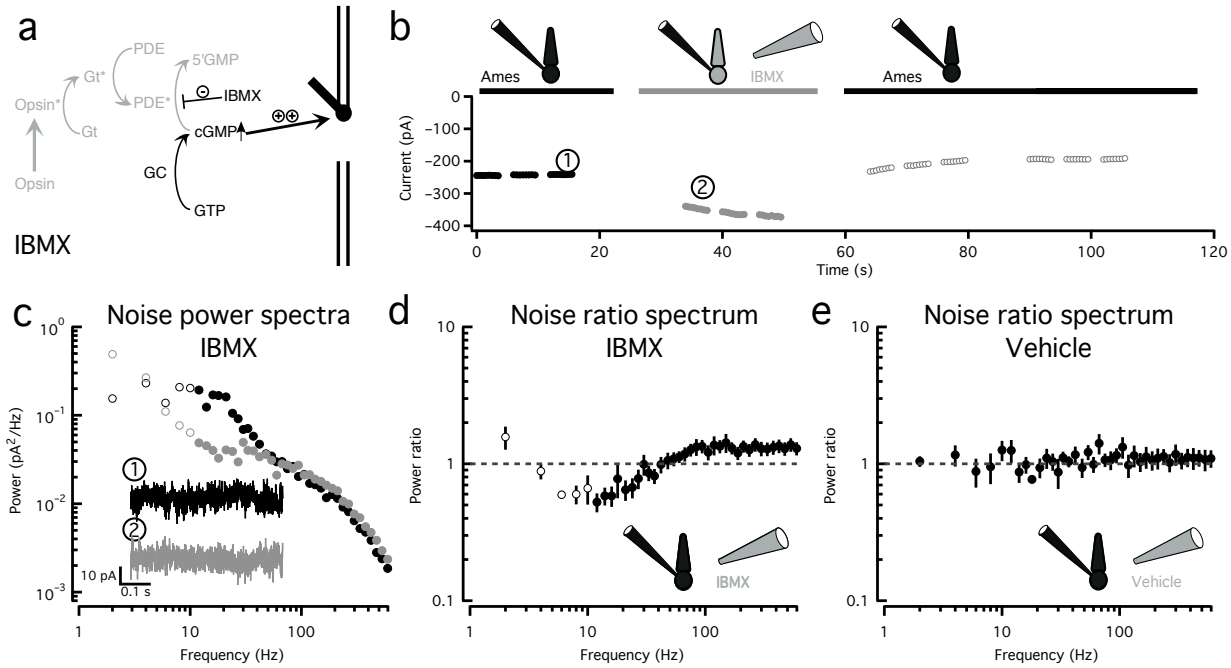

Figure 2.4 - An additional noise source with power in the low to mid frequency range causes fluctuations in cGMP

a. The membrane-permeable and fast acting PDE inhibitor IBMX increases the cGMP concentration and therefore the number of open channels and inhibits any noise source upstream of (and including) PDE.

b. Changes in holding current in the absence (black) and presence (gray) of IBMX. The filled black and gray circles represent 500 ms stretches of noise used to calculate the spectra in (c). Recordings were performed in complete darkness to avoid extrinsic noise.

c. Corresponding power spectra in the absence (black circles) and presence (gray circles) of IBMX. Insets show example noise traces in each condition corresponding to (1) and (2) in (b). Changes in noise below 10 Hz (open circles) are unreliable due to slow drift in the measured current.

d. Average (± SEM) ratio of power spectra in the presence and in the absence of IBMX (n = 10) showing a decrease in noise in the 10 to 50 Hz range and an increase in noise at high frequencies (100 to 600 Hz)

e. Average (± SEM) ratio of power spectra before and after puffing a vehicle solution lacking IBMX (n = 4). The increase in noise at the high frequencies (100 – 600 Hz) and

the decrease at low frequencies (10 – 30 Hz) seen with IBMX were significantly different than the changes with vehicle.

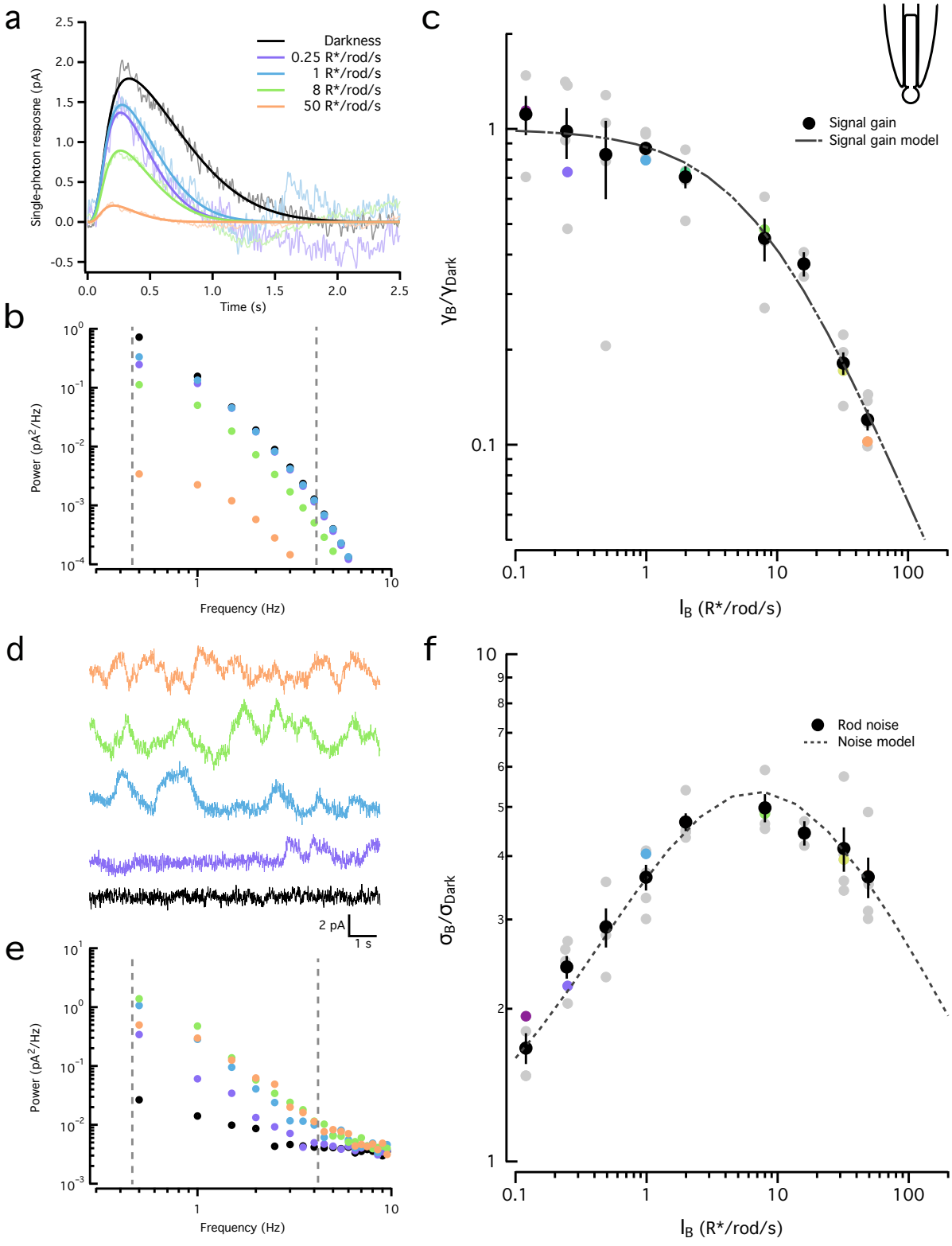

Figure 2.5 - Adaptation similarly affects rod signal and noise.

a. Linear estimates of the rod single photon responses for a range of backgrounds. Increasing backgrounds resulted in faster and smaller responses. Fits were obtained using equation 2.2. Correspondence between light levels and color scale is maintained throughout the figure.
b. Power spectra of the fitted single photon responses in (a). Dashed lines show integration limits.
c. Square root of the integrated signal power (0.5 Hz – 4 Hz) normalized by that in darkness for the example rod in (a) and (b) (colored circles) and for a population of rods (gray circles). The population data (black circles, mean ± SEM, n = 5) was fit with equation 2.4 with I_0 = 7.1 R*/s.
d. Examples of noise traces for the same rod and backgrounds as in (a).
e. Power spectra of the noise traces in (d). Dashed lines show integration limits.
f. Square root of the power spectrum integral (0.5 Hz – 4 Hz) of the noise normalized by darkness for the example rod in (a) and (d) (colored circles) and for a population of rods (gray circles). The population (black circles, mean ± SEM, n = 5) was fit with equation 2.4 with I_D = 0.062 R*/s.

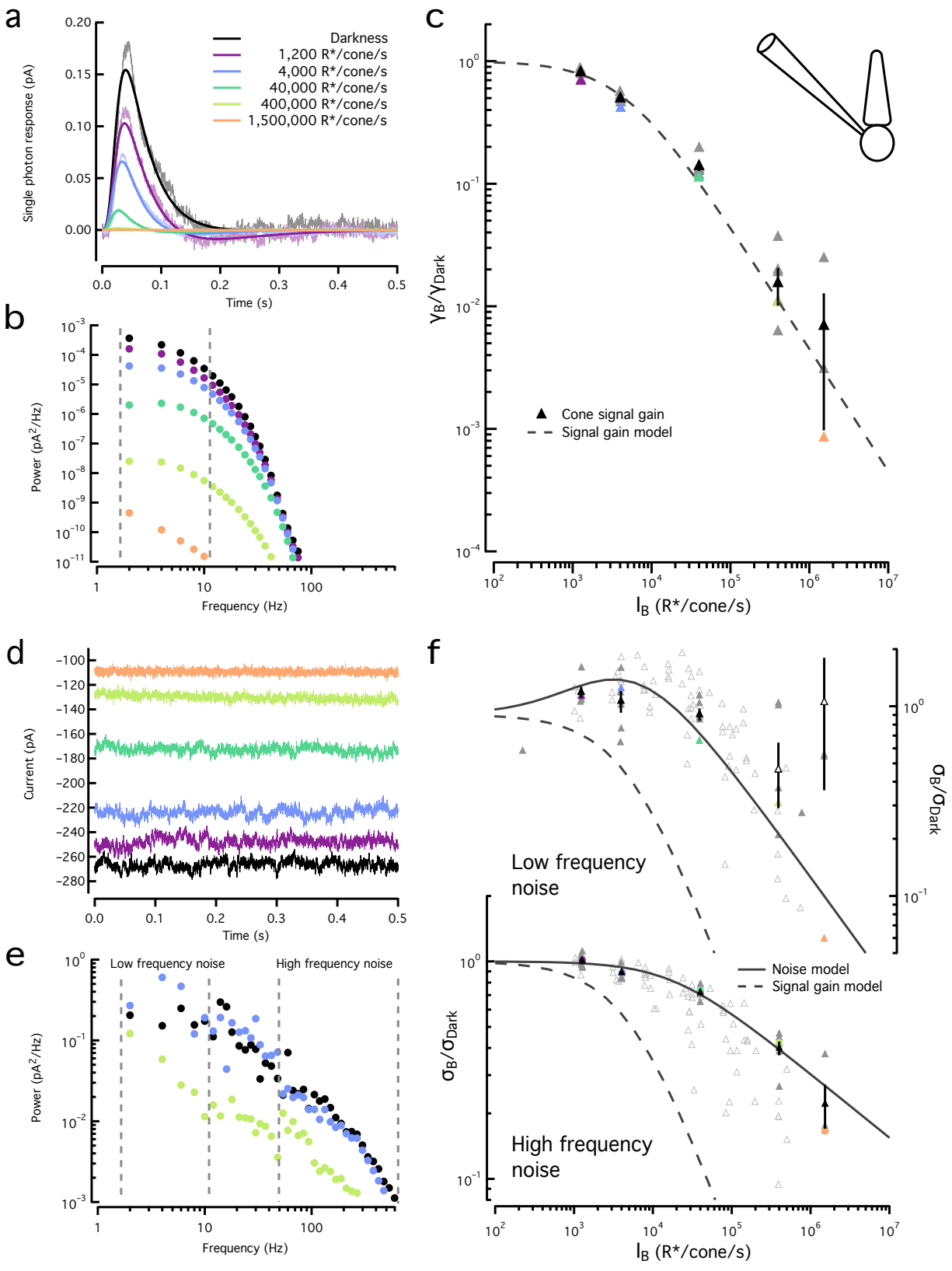

Figure 2.6 - Adaptation affects cone signal and noise differently.

a. Estimated cone single photon responses for a range of backgrounds, fit with equation 2.2. Color scale is maintained throughout the figure.
b. Power spectra of the fitted single photon responses in (a). Dashed lines show integration limits.
c. Square root of the integrated signal power (2 – 10 Hz) normalized by that in darkness for the example cone in (a) and (b) (colored triangles) and for a population of cones (gray triangles). Population data (black triangles, mean ± SEM, n = 6) was fit with equation 2.4 with I_0 = 4,500 R*/s.
d. Example noise traces for the same cone and backgrounds as (a).
e. Example noise power spectra for the same cone as (a).
f. *Top*, Square root of the integrated noise power at low frequencies (2 – 10 Hz) normalized by that in darkness for the example cone in (a) (colored triangles) and for a population of cones (gray triangles). Dashed line shows signal gain curve from (c). Noise below 10 Hz at the highest backgrounds (black open triangles) was unreliable and was excluded from fitting. Population (black triangles, mean ± SEM, n = 6) was fit with equation 2.5 with I_D = 620 R*/s. *Bottom*, Square root of the integrated noise power at high frequencies (50 Hz to 600 Hz) as in top panel. The population data was fit with equation 2.3 with I_o=17,500 R*/s and η = 0.29. Open grey triangles show noise from cones in which signal adaptation was not assessed (n = 6); fit to low frequency noise used I_D = 1,200 R*/s and I_0 = 9,950*/s and fit to high frequency noise used I_o = 13,360 R*/s and η = 0.34.

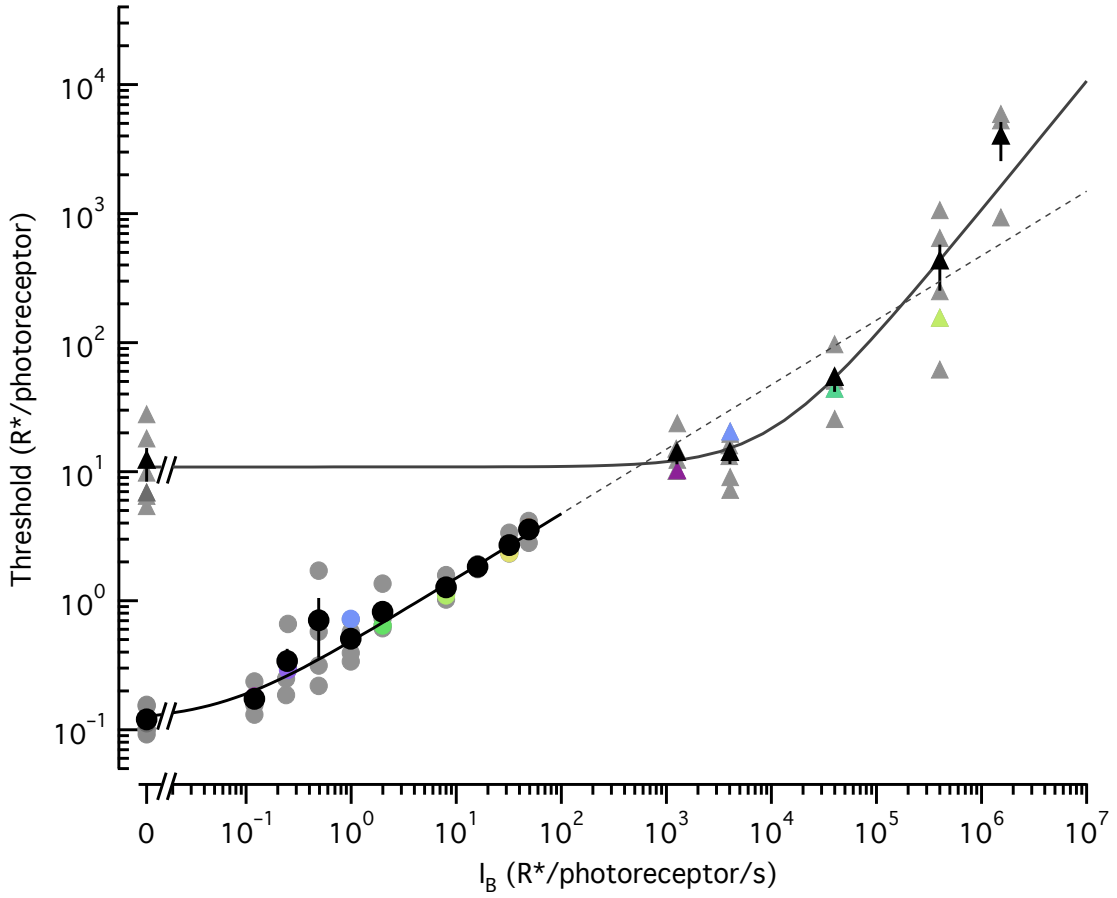

Figure 2.7 - Background dependence of rod and cone detection thresholds. Detection thresholds were derived for both photoreceptor types from the data shown in Figure 2.5 and 6 (see Methods). Colored symbols correspond to thresholds for the example rods and cones from Figure 2.5 and 6, while gray symbols correspond to population data (5 rods, 6 cones). The rod thresholds (black circles show mean ± SEM) were well described by equation 2.6, with a dark threshold < 1 R*/rod. The cone thresholds (black triangles show mean ± SEM) were well described by a Weber-like function (equation 2.7) with a dark threshold of 10.9 R*/cone, and a threshold-doubling background, I_o = 11,700 R*/s. The fit to the rod thresholds was extended to higher backgrounds to directly compare the slopes; in this log-log plot, the slope for rods is 0.5 corresponding to a “square-root” behavior while the slope for cones is 1, corresponding to a Weber behavior.

Chapter 3

Fast light adaptation in primate cone photoreceptors permits encoding of information during eye movements

3.1 Summary

The visual exploration of natural scenes in primates relies on sophisticated eye movements that point the fovea to relevant regions. The wide and fast changes in inputs during visual exploration pose a challenge for the encoding of information requiring fast and local adaptation to the input statistics. The work presented here explores how cones adapt and encode information during eye movements. First, we find that responses in cones to naturalistic stimuli are highly nonlinear due to light adaptation. Second, we show that these responses can be captured with biophysical models of the phototransduction cascade. Third, we show how light adaptation shapes the encoding of information in cones during eye movements, finding differences in the encoding of mean luminance compared to the encoding of temporal contrast. The findings and model presented here are crucial to explore encoding during eye movements in the rest of the visual system.

3.2 Introduction

Most of our everyday visual activities, like reading or exploring details in a visual scene, start with signaling in the fovea, a small and specialized patch of the retina where cone photoreceptors are most densely packed and spatial acuity is best (Curcio and Sloan, 1992). Visual cues detected in the periphery, where spatial acuity and cone density are lower, cause ballistic eye movements, or *saccades*, to direct and fixate the fovea to the region of interest. During free visual exploration of natural scenes, humans make two to six saccades every second that can span several degrees of visual angle (Harris *et al.*, 1988). On the spatial scale of saccades, natural scenes can exhibit thousand-fold differences in both local luminance (measured as the mean light intensity in patches of <1 min of arc) and local spatial contrast (measured as the root mean square of light intensities in the same patches) (Frazor and Geisler, 2006).

Reliable encoding of visual information during the fixations occurring between saccades imposes several challenges on the visual system: first, given that the dynamic range of neural signals is small compared to the range of inputs encountered during exploration of a scene, the visual system has to be able to adjust its gain to match the inputs; second, given that fixations last about 200 to 600 ms, adaptation mechanisms must operate quickly; third, given the weak correlations between local luminance and local spatial contrast in natural images (Mante *et al.*, 2005, Frazor and Geisler, 2006), adaptation to these two input properties should be independent.

The need to adapt to local statistics of an ever changing environment is general across sensory systems. For example, adaptation allows bacteria to follow molecular gradients across a >10,000-fold range of concentrations (Bialek and Setayeshgar, 2005, Neumann *et al.*, 2014), and the kinetics of adaptation govern the ability to follow these gradients (Segall *et al.*, 1986). Similar challenges arise in the tracking of odor plumes in insects, where turbulent flow creates enormous variations in odorant concentrations (Carde and Willis, 2008) or in the auditory system, where signals are embedded in highly variable levels of background noise. In these two latter systems, adaptation at the primary receptor (odorant receptor neurons and hair cells) is fundamental to maintain sensitivity (Fettiplace and Ricci, 2003, Kelliher *et al.*, 2003).

Vision also relies on adaptation in the primary receptors - the rod and cone photoreceptors. Indeed, for typical daytime light levels, most of the adaptation in the retinal output to changes in luminance occurs in the cones themselves (Dunn *et al.*, 2007). Adaptation operates by light-dependent changes in internal calcium concentration, which affect both the gain and kinetics with which light inputs are converted to electrical signals (Krizaj and Copenhagen, 2002). Here we explore how adaptation allows primate cones to encode information during eye movements. We find: (1) cone responses to inputs such as those encountered during eye movements are highly non-linear due to adaptation within the phototransduction cascade; (2) cone responses to simulated eye movements can be captured by a biophysical model of the cone phototransduction cascade; and (3) adaptation differentially affects the encoding of mean luminance and of temporal contrast.

3.3 Methods

3.3.1 Animals, tissue and solutions

We made electrophysiological recordings from primate retinas (*Macaca fascicularis*, *nemestrina* and *mulatta* of either sex, ages 3 – 19 yrs) in accordance with the Institutional Animal Care and Use Committee at the University of Washington. We obtained retina through the Tissue Distribution Program of the Regional Primate Research Center. We performed most enucleations under pentobarbital anesthesia. After enucleation, we rapidly separated the retina-pigment epithelium-sclera complex (< 5 min) from the anterior segment, drained the vitreous humor, and dark-adapted the retina for 1h in warm (32^{o} C) Ames medium bubbled with a mixture of 95% CO_2 - 5% O_2. In some young animals, we drained the vitreous after incubation in plasmin (~ ???g/mL in ~5mL of solution for 15 to 30 min). We performed all subsequent procedures under infrared (> 900 nm) light. For recording, we separated a small piece of retina (~4mm^2) from the pigment epithelium and mounted it photoreceptor side up on a poly-lysine coated coverslip (BD Biosciences) forming the floor of a recording chamber. We continually superfused retinas with warm (~31° - 33° C) oxygenated Ames medium. Treatment with DNase I (Sigma-Aldrich) (30 units in ~250 µL of Ames for 4 min) facilitated access to the photoreceptor inner segments.

3.3.2 Recordings and light-stimulation

For whole-cell voltage-clamp recordings (holding potential –70 mV) we measured cone signals with an internal solution containing (in mM): 133 potassium aspartate, 10 KCl, 10 HEPES, 1 $MgCl_2$, 4 Mg-ATP, 0.5 Tris-GTP; pH was adjusted to 7.2 with NMG-OH and osmolarity was ~280 mOSM. The internal solution did not contain any calcium buffer (or calcium), as even low concentrations of calcium buffer caused the light response to become increasingly biphasic during the course of a recording. For current-clamp recordings (without any current-injection) under perforated patch, we used an internal solution with 30 μg/mL gramicidin and with EGTA buffering to be able to detect inadvertent whole-cell access; it contained (in mM): 125 potassium aspartate, 10 KCl, 10 HEPES, 5 EGTA, 1$MgCl_2$, 0.5 $CaCl_2$, 4 Mg-ATP, 0.5 Tris-GTP; pH was adjusted to 7.2 with NMG-OH and osmolarity was ~280 mOSM.

We delivered light stimuli from blue, green and red LEDs (peak wavelengths 405, 510 and 640 nm), which permitted quick identification of cone types. The stimuli illuminated a ~150 μm diameter area centered and focused on the recorded cone. We converted photon densities (photons/μm^2) to R*/photoreceptor using a collecting area of 0.6 μm^2 (Schneeweis and Schnapf, 1999), previously measured cone spectral sensitivities (Baylor *et al.*, 1984) and the LED spectra.

We acquired data using Multiclamp 700B amplifiers. We low-pass filtered recorded currents at 3 kHz and digitized the data at 20 kHz. We analyzed recorded data through custom routines in Matlab (The Mathworks). We excluded from analysis cones that showed unusually rapid run-down of light responses, low sensitivity or short-lived recordings. All cones presented here were either L or M cones. The best fit values for models and empirical descriptions were obtained through automatic fitting routines (Matlab's *nlinfit*, *fmincon* and *lsqcurvefit*). The quality of model fits were evaluated as the ration between the sum of squared errors of the model to the data and the sum of squared errors of the model to the mean response.

3.3.3 Model of fixation duration and saccades

The model to generate naturalistic stimuli was based on a statistical approximation from measurements of eye movements made in humans (Harris *et al.*, 1988). In this model, fixation times follow an exponential distribution with a refractory period, such that the probability, of two saccades following each other is given by:

$$\begin{cases} \frac{1}{\beta} \times e^{\frac{-(t-\alpha)}{\beta}} & \text{if } t \geq \alpha \\ 0 & \text{if } t < \alpha \end{cases} \tag{3.1}$$

where α = 100 ms is the refractory period (Harris *et al.*, 1988); the time constant of the exponential distribution (β = 200 ms) was elected to generate on average 3 saccades every second (range: 2 to 5). This model did not include any fixational eye movements.

Saccades where then inserted between fixations, with a duration (D_S), proportional to a random amplitude (A_s), and dictated by:

$$D_s = \frac{A_s - a_s}{v_s} + d_s \tag{3.2}$$

where the velocity, v_s, was drawn from a uniform distribution between 0.4 and 0.6°/ms, a_s = 10° and d_s = 40 ms (Rucci *et al.*, 2000). This generated saccades that lasted ~15 ms. At each fixation the luminance was drawn from distributions constructed from individual natural images taken from the van Hateren database (van Hateren and van der Schaaf, 1998). During saccades, the transitions between luminances were linear.

3.3.4 Linear and linear-nonlinear model

To construct a linear filter, we recorded cone photocurrent responses to dim flashes in darkness and divided them by the strength of the flash, to obtain a linear estimation of the single photon response. The single-photon responses were then fitted with the following equation (Baylor *et al.*, 1987, Angueyra and Rieke, 2013):

$$f(t) = \alpha \left(\frac{(\frac{t}{\tau_{rise}})^4}{1 + (\frac{t}{\tau_{rise}})^4} \right) \times e^{-\left(\frac{t}{\tau_{decay}}\right)} \times cos(\frac{2\pi t}{\tau_{osc} + \omega}) \tag{3.3}$$

The parameters obtained for the example cell in figure 3.1c are: α = 831, τ_{rise} = 28.1 ms, τ_{decay} = 24.3 ms, τ_{osc} = 2x10^3 s and ω = 89.97°.

The linear filter was then convolved directly with the light stimulus to obtain a linear estimate of the responses. Given that the linear filter was obtained in darkness, where gain is maximal, we allowed rescaling of the linear model by a single factor. The rescaling factor was chosen to match the current at the end of the highest fixation, and had a value of 0.01 for the example cone presented in figure 3.1.

The relationship of real and linear model currents were fitted with the following function:

$$i_{data} = aC\left[b(i_{lin.model}) + d\right] + e$$

(3.4)

where C[ ] is the cumulative density of a normal function with zero mean and standard deviation of 1 (Chichilnisky, 2001). The parameters for the fit shown in figure 3.1d were a = 1217.62, b = 0.0284, d = 1.7405 and e =-1174.08.

3.3.5 Biophysical model with a single feedback mechanism

The biophysical model of the phototransduction cascade briefly presented here (figure 3.6) follows a model of phototransduction for toad rods (Rieke and Baylor, 1996, Rieke and Baylor, 1998), but is largely equivalent to other biophysical models successfully used in the past in rods and cones from other species (Pugh and Lamb, 1993, Nikonov *et al.*, 1998, Endeman and Kamermans, 2010), and as the first component of a primate horizontal cell model (van Hateren, 2005).

In the first step of the model, the activity of light-activated opsin molecules (R) decays with a time constant σ:

$$\frac{dR(t)}{dt} = -\sigma R(t)$$

(3.5)

Active opsin molecules activate phosphodiesterase (PDE) molecules through transducin (a delay we assume is negligible) (Pugh and Lamb, 1993), so that the activity of PDE (P) follows:

$$\frac{dP(t)}{dt} = \sigma R(t) - \phi P(t) + \eta$$

(3.6)

where ϕ is the decay time constant of PDE and η is the PDE dark activity.

The concentration of cGMP in the outer segment (G) depends on the PDE-mediated hydrolysis and the rate of synthesis (γ) by the guanylate cyclase (GC) :

$$\frac{dG(t)}{dt} = \gamma(t) - P(t)G(t)$$

(3.7)

The outer segment current carried by the cGMP-gated channels depends on G approximated by:

$$I(t) = kG(t)^h$$

(3.8)

where k is the product of the maximal current and the channel affinity for cGMP (fixed to 10^{-3} pA/μM) and h is the apparent cooperativity (Rieke and Baylor, 1996).

A fraction of the outer segment current (q) is carried by calcium, and therefore calcium concentration (Ca) decreases upon exposure to light; calcium extrusion, mainly through the Na^+/K^+, Ca^{2+} exchanger. We simplify this process as a single exponential process with time constant β:

$$\frac{dCa(t)}{dt} = qI(t) - \beta Ca(t)$$

(3.9)

The calcium concentration then regulates γ (the rate of cGMP synthesis) following a Hill-curve such that:

$$\gamma(t) = \frac{\gamma_{max}}{1 + \left(\frac{Ca(t)}{K_{GC}}\right)^m}$$

(3.10)

where γ_{max} is the maximum synthesis rate, and K_{GC} and *m* are the affinity and cooperativity constants respectively.

We independently fit this model to the data in figure 3.1 and figure 3.2. The best fit parameters are summarized in Table 3.1.

3.3.6 *Biophysical model with two separate feedback mechanisms*

For this model (figure 3.7), we added a second calcium-dependent feedback (with slower kinetics than the feedback to the cyclase) that decays with a time constant β_{slow} following:

$$\frac{dCa_{slow}(t)}{dt} = \beta_{slow}\left(Ca_{slow}(t) - Ca(t)\right) \tag{3.11}$$

with $\beta_{slow} < \beta$, and acting directly on the cGMP-gated channels such that equation (3.8) becomes:

$$I(t) = \frac{kG(t)^h}{1 + \dfrac{Ca_{slow}(t)}{Ca_{dark}}} \tag{3.12}$$

We also independently fit this model to the data in figure 3.1 and figure 3.2. The best fit parameters are summarized in Table 1.

3.4 Results

The results are divided into three sections. First, we show that accounting for the responses of primate cones to stimuli that emulate saccades and fixations requires models incorporating time-dependent (e.g. adaptive) non-linearities. Second, we develop a biophysical model with two kinetically-distinct feedback mechanisms that is able to account for cone responses to the wide array of stimuli presented here. Third, we show how two distinct adaptational mechanisms separately govern the time scale of luminance and contrast discrimination during eye movements.

3.4.1 Primate cone responses to naturalistic stimuli

3.4.1.1 A simplified model of luminance changes during saccadic eye movements

To explore how cones behave during eye movements, we generated stimuli that approximated the luminance changes during free viewing for single cones (figure 3.1a). We ignored fixational eye movements (microsaccades, tremor and drift), and modeled the duration of fixations as an exponential distribution with a minimum intersaccade interval (Harris *et al.*, 1988); the exponential time constant was chosen to produce ~3 saccades every second. The light intensity for each simulated fixation was determined by randomly sampling from an intensity distribution taken from natural images (van Hateren and van der Schaaf, 1998). Saccades lasted ~15 ms, during which the intensity changed linearly (see methods for details). The resulting stimuli captured the wide, rapid and variable changes in light-intensity characteristic of cone inputs under free-viewing conditions (figure 3.1b).

3.4.1.2 Cone responses to naturalistic stimuli

Cone current responses to naturalistic stimuli showed several complex behaviors (figure 3.1d). First, responses following increases or decreases in luminance exhibited kinetic changes on several time scales, but the responses were not antisymmetric as would be expected for a linear system. Second, gain was not constant; instead, high intensities produced considerable response compression; for example, the difference in responses to the two highest intensities (closed arrows in figure 3.1d) were similar to those produced by >10-fold smaller intensity changes (open arrows). Third, responses depended on the previous intensities; for example, identical luminances with different preceding luminances elicited responses that differed in both peak amplitude and kinetics (figure 3.1d, asterisks and figure 3.1c).

3.4.1.3 Cone responses can't be captured by linear models nor linear-nonlinear models

How well do simple models capture the cone responses to naturalistic stimuli? We started by using the average response to dim flashes in darkness (figure 3.1e) to construct a linear prediction of the response. Because the gain in darkness is high, we imposed a single scaling factor (~1/100) that matched the linear prediction to the mean current at the end of the fixation for the brightest luminance. The resulting prediction

failed to capture the peak or final currents during other fixations and did not match the pronounced dynamical changes during each fixation (figure 3.1f). These shortcomings, particularly the transient current changes at the start of each simulated fixation, cannot be corrected by other choices of the scale factor for the linear prediction. The quality of the model fit to the data was evaluated by comparing the sum of squared errors between the model and the individual responses to the stimulus with the sum of squared errors between the mean response and the individual responses; a ratio (R) of these errors close to 1 would mean that the model captures the data as well as the mean. For the linear model $R_{linear} = 2.39$ - i.e. measured as squared error, the linear model was 2.39-fold worse than the mean at capturing the data.

We next tested whether a time-independent nonlinearity could improve the predicted response. We constructed such nonlinearity by fitting the relationship between the linearly predicted and measured currents at the end of each fixation (figure 3.1g). The resulting linear-nonlinear model (LN model) largely resolved the discrepancies in currents obtained at the end of fixations (which is not surprising since it was fitted directly to them) and significantly improved the quality of fit ($R_{LNmodel} = 1.70$) but was still not able to capture either the history-dependence of the currents (e.g. two fixations marked by asterisks in figure 3.1d) or the transient current changes at the start of a fixation.

Linear and linear-nonlinear models lack a time-dependent nonlinearity like light adaptation, which is known to be pronounced in cones from many species (such as salamander (Soo *et al.*, 2008) and bass (Korenbrot, 2012)) including primate (Schnapf *et al.*, 1990, Angueyra and Rieke, 2013, Cao *et al.*, 2014). Thus, we sought to quantify the magnitude and time course of light adaptation to understand how it shapes the encoding of luminance changes encountered during eye movements.

3.4.2 Speed of information encoding in primate cones is governed by the kinetics of light adaptation

3.4.2.1 Light adaptation produces fast and asymmetric changes in gain

To determine the speed of adaptation, we probed gain as a function of time following an increase or decrease in mean light-level. To achieve this, we recorded cone photocurrents in response to a combination of five brief flashes and a step of light. Three of the probing flashes were kept fixed in time across trials (before the step, during but late after the step onset and late after the step offset), while the other two were delivered with variable intervals near step onset and near step offset; to counteract the decreases in gain produced by light-adaptation, flashes during the step were brighter than the ones delivered from darkness (figure 3.2a). Subtracting the response to the step alone (gray trace in figure 3.2b) isolated responses to the individual flashes (figure 3.2c).

The fixed flashes before the step and late after step offset elicited near-identical responses, corresponding to unadapted flash responses; the fixed flash during but late after step onset produced a completely light-adapted response, characterized by lower amplitude and faster kinetics. The responses to the flashes delivered near step onset or offset corresponded to transitional states between the unadapted and the light-adapted responses (figure 3.2c).

The response gain or sensitivity (in units of pA/R*) was estimated by dividing the isolated flash responses by the flash strength (in R*). Changes in gain had reached steady state by 200 ms but with striking asymmetries, being faster at step onset than at step offset (figure 3.2d and e). An approximate time constant was extracted by fitting the gain changes with single exponential functions (gray lines in figure 3.2d and e). Across a population of cells (n = 15) and light intensities of the step (ranging from 1,500 to 100,000 R*/s), the extracted time constants of gain changes at step onset were on average 3 to 4 times faster than at step offset (mean ± sem: τ_{onset} = 23 ± 2 ms; τ_{offset} = 94 ± 5 ms) (figure 3.2f). We did not find strong correlations between the time constants and the intensity of the step (data not shown). Since the time to peak of the response to the step alone is ~40ms, most of the gain changes occurred during the rising phase of the step response. Changes in the mean current (gray trace in figure 3.2b) were much slower than changes in gain. This dissociation between gain and mean current was less pronounced at step offset.

These marked asymmetries suggest that the dynamical changes in the cone responses arise from differences in kinetics associated with the engagement and disengagement of light adaptation.

3.4.2.2 Rapid light-adaptation causes On/Off asymmetries in primate cones

The asymmetries in the kinetics of adaptation following increases and decreases in mean light level suggests that responses to increments and decrements in light-level could also be asymmetric (Endeman and Kamermans, 2010). This is an important issue because increment-decrement asymmetries observed in downstream cells are often attributed to differential processing in On and Off circuits rather than asymmetric cone inputs (see discussion). To test for such asymmetries in cones, we delivered positive and negative steps of equal Weber contrast relative to a mean light level, while recording cone photocurrent (figure 3.3a), cone voltage (figure 3.3c) or horizontal cell voltage (figure 3.3D). Responses to Weber contrasts < 25% were near-linear, but for higher contrasts responses to decrements were consistently larger than to corresponding increments. We quantified the increment/decrement asymmetry from the ratio of mean currents at the end of the steps at 100% contrast. The ratio of decrement to increment responses exceeded one across all light levels probed (figure 3.3e). At the lowest luminances (< 5,000 R*/s) the asymmetry was less pronounced; at higher luminances, where light-adaptation is more pronounced, this asymmetry was more robust and easier to detect (compare figure 3.3a and 3b).

The experiments described so far have shown that cone responses are highly dynamic, with fast gain changes and asymmetric responses produced by light adaptation. Linear and LN models, lacking any time-dependent nonlinearities, fail to reproduce these responses (figure 3.1). For this reason, we turned our attention to biophysical models able to incorporate dynamical light adaptation.

3.4.3 A biophysical model of cone responses

3.4.3.1 A model with only fast gain changes does not capture responses to naturalistic stimuli

Biophysical models have been successful in capturing rod responses in amphibians and mammals (Rieke and Baylor, 1996, Younger *et al.*, 1996, Nikonov *et al.*, 2000), responses in fish cones (Endeman and Kamermans, 2010, Korenbrot, 2012) and responses from primate horizontal cells (van Hateren, 2005). Despite small implementation nuances, these models follow the same basic structure; for this reason we decided to specifically follow the implementation used in rod photoreceptors in toad (Rieke and Baylor, 1996) to try to account for the outer segment current responses of primate cone photoreceptors (figure 3.4a). In this biophysical model the different biochemical reactions that compose the phototransduction cascade are represented as a nonlinear set of first-order differential equations, and adaptation is largely implemented through calcium feedback to the guanylate cyclase (Nikonov *et al.*, 2000, van Hateren, 2005) (see methods for a detailed explanation). This model has ten parameters, which include the time constants of the different reactions, affinities, cooperativity and concentration of different components; we fixed the values of four of these parameters and varied the remaining six to fit different data sets (summarized in Table 1).

We first fit this model to the responses to the combined steps and flashes (figure 3.4b). The model exhibited fast gain changes similar to the real data (figure 3.4c), that also were slower at step offset that at step onset (blue triangle in figure 3.2d). However, the model failed to capture the slow kinetics to the step response itself, produced flash responses with slow recovery kinetics and did not entirely match the degree of adaptation seen in the data (figure 3.4b and c).

When used to fit cone responses directly to naturalistic stimuli, the best-fit model was a significant improvement over the linear and LN models($R_{biophys.model}$=1.65) (for example, this model does show some history-dependence); nevertheless, the model was unable to capture the final current of every fixation and the dynamic changes in current produced by each transition in luminance simultaneously (figure 3.4d). The inability of the model to fit these data is not surprising: the model lacks a slow adaptational mechanism that could account for the slow changes in mean current following a change in luminance.

3.4.3.2 A biophysical model with fast changes in gain and slower changes in current captures responses to naturalistic stimuli

We added to the model presented above a slow feedback mechanism that regulated the activity of cGMP-gated channels directly; we chose to implement this feedback as a calcium dependent mechanism (Korenbrot, 2012, Rebrik *et al.*, 2012, Korenbrot *et al.*, 2013) (see discussion), but similar models with different mechanistic implications would yield similar results (figure 3.5a). This model includes the additional reaction time constant of this calcium feedback, for a total of 11 parameters, 4 fixed and 7 free. The best fits of the model to the different data sets were not unique, but small changes in parameters (up to 5%) did not significantly alter the quality of the fit, suggesting the model is robust to modest changes in parameters.

This model provided good fits to the responses to combined steps and flashes, capturing both the slow dynamics of the step response and the fast gain changes probed by the flashes (figure 3.5b), with a good match to the kinetics (figure 3.5c and red point in figure 3.2d). We also obtained good fits to responses to naturalistic stimuli, getting good matches to the dynamic changes in current and to the final current at the end of all fixations (figure 3.5d), with a closer agreement to the data ($R_{biophys.model2}$=1.12) (see table 1 for the different set of parameters obtained for each data set).

When presented with the other stimuli presented in previous sections, the model continued to respond similarly to real cones. These responses included: (1) the asymmetric responses to contrast increments and decrements; (2) the voltage responses to luminance steps (model included a linear current to voltage conversion, see methods); and, (3) the voltage responses to sinusoidal modulation superimposed to luminance steps (data not shown).

In summary, while linear or LN models fail to capture the full range of cone responses, models that incorporate two distinct dynamical light-adaptation mechanisms that differ in kinetics and sensitivity have the ability to capture the responses to the wide array of stimuli presented here, suggesting that these light-adaptation mechanisms are the main contributors shaping these responses. This led us to explore how this two separate feedback mechanisms shape the encoding of information during eye movements.

3.4.4 Luminance and contrast encoding during eye movements follow different time-courses and have different sensitivities

During eye movements, saccades produce changes in the mean luminance experienced by individual cones; once a saccade has been completed, fixational eye movements combined with fine spatial structure in a natural scene (spatial contrast), will produce a temporal modulation of luminance in individual cones, which we will refer as temporal contrast (Frazor and Geisler, 2006). How do the kinetics of adaptation in cones limit or allow the discrimination of differences in luminance, or the detection of temporal contrast, immediately after a saccade? Below we describe a set of experiments that show that the discrimination of mean luminance is relatively sluggish and follows the slow changes in mean current, while the detection of temporal contrast immediately after a change in mean luminance follows a faster time course that tracks the fast gain changes characterized in figure 3.2.

We constructed stimuli designed to probe luminance discrimination and temporal-contrast detection independently. In the first set of experiments, we emulated changes in mean luminance when a saccade is made from a bright region of a natural scene to a darker region and then back to the same bright region (figure 3.6a, left and 6b). In the second set of experiments, we emulated temporal contrast produced by fixational eye movements under these same changes in mean luminance by superimposing a sinusoidal modulation (figure 3.6a, left and 6c). On the third and fourth set of experiments, we followed the same logic, but emulating changes in mean luminance (figure 3.7b) and temporal contrast (figure 3.7c) when saccades are made from a dark region of a natural scene to a bright region and back to the same dark region (figure 3.7a). The experiments presented in this section required longer and more stable recordings; for this reason, we used perforated-patch current-clamp recordings to measure the membrane potential from single cones.

3.4.5 Luminance discrimination and temporal-contrast detection follow different time courses

The kinetics of mean-luminance discrimination were first tested by recording voltage responses to steps from a single high light intensity (~18,000 R*/s) to one of four lower light intensities (~350 R*/s, ~700 R*/s, ~1,400 R*/s, or ~2,800 R*/s) (figure 3.6b). To isolate the dependence of the voltage trajectory on light intensity, we subtracted the response to the 2,800 R*/s step from the others. Following a decrease in light intensity, the responses initially follow a similar trajectory, diverge after ~50 ms, and reach a maximal difference after ~200 ms. The differences in response were graded with the value of the low light intensity. The return to the high light intensity produced clear differences between responses that depended on the past low luminance and that decayed over ~200 ms (figure 3.6c).

Noise in the responses was, at most, weakly stimulus dependent (figure 3.6d). Hence, the discriminability of the different low light intensities (measured in terms of d' [d prime], a signal-to-noise ratio measurement obtained by taking the absolute difference between the step responses and dividing it by the mean of the noise in both responses) follows the same time course as the response differences: at luminance decrease, discriminability is maximal after ~200 ms; upon return to a high luminance, the loss of discriminability (i.e. the loss of history-dependence) slowly decays (figure 3.6e). The time course of the differences in response was consistent across cells (n = 4) (figure 3.4f).

To probe the kinetics of detection of temporal contrast under the same mean-luminance changes, we superimposed a 5 Hz sinusoidal modulation to the light intensity steps (figure 3.6a, middle). To elicit comparable responses, sine contrast was 100%-Weber contrast at the low light intensity and 30%-Weber contrast at the high light intensity. Sinusoidal modulation of the cone voltage was isolated by subtracting the corresponding response to the luminance steps alone (figure 3.4g). Subtracting the sine responses at 2,800 R*/s from the rest of the sine responses revealed that the responses to temporal contrast were smaller at the lowest light intensities (figure 3.4h). Upon return to the high light intensity, however, sinusoids elicited indistinguishable responses (figure 3.4i). Specifically, the return to the high light intensity did not elicit responses to temporal contrast that showed history dependence. Noise across responses, like that for steps alone, did not show strong stimulus dependence (figure 3.4j).

We calculated the detectability of the isolated sine responses using the peak responses to four different sinusoid phases (raw data shown previously only contains one phase) (figure 3.4j). At the low light intensities, only the earliest peak response showed a reduced amplitude, with steady state already reached rapidly, by the second half cycle (figure 3.4g and j). At the high luminance, maximum detection was reached even faster, and already possible at the time of the first peak response (figure 3.4j). These observations were consistent across cells (figure 3.4k), suggesting that, in cones, the detection of temporal contrast follows a separate time scale than the discrimination of mean luminance

3.4.6 Luminance discrimination and temporal-contrast detection have different sensitivities

We also stimulated cones with abrupt changes from a low light intensity (~750 R*/s) to one of three high light intensities (~18,500 R*/s, ~21,000 R*/s or ~24,000 R*/s) and back (figure 3.7a) and tested the discriminability of the responses to such stimuli. Although in absolute terms the three high light-intensity values were quite different (14% to 29%), the mean responses differed very little (figure 3.7b). Differences between responses and therefore discriminability was marked only transiently, at the peak of the response (figure 3.7c,d and e). The sinusoidal modulation at the high light intensities again produced responses that settled quickly (steady state reached by the first peak) (figure 3.7g) and were indistinguishable across light intensities, even though in absolute terms the sinusoids themselves differed also by 14% to 29% in intensity (figure 3.7h); in other words, at the high light intensities, cones showed responses that are constant with respect to contrast (and independent of the mean light level). These observations were also consistent across cells, with small differences in steady-state mean current to 29% differences in luminance (figure 3.7f) but robust and indistinguishable responses to 30% contrast modulation at the high light intensities(figure 3.7k), suggesting that the detection of temporal contrast is more sensitive than the discrimination of luminance.

Taken together, these results suggest that, during the changes in inputs experienced during eye movements, adaptation in primate cones follows at least two different time scales and has two different sensitivities. A fast adaptational mechanism

rapidly controls gain (figure 3.2) and allows fast encoding of temporal contrast (figure 3.6g-k), while a slower and less sensitive mechanism adjusts the steady-state response to the mean luminance more gradually, producing lingering effects that impair the speed of luminance encoding (figure 3.6b-f). Interestingly, at transitions to high light intensities, luminance discrimination is less sensitive than the detection of temporal contrast (which shows signs of contrast constancy expected from Weber behavior) (figure 3.7) (Angueyra and Rieke, 2013). At transitions to low luminances, where gain changes are less than Weber, luminance discrimination is more reliable (albeit slow) but responses are not contrast-constant (figure 3.6).

3.5 Discussion

The need to adapt to the statistics of the natural environment is common among sensory systems and especially crucial for the visual system, since it has to support behavior in ambient light levels that can span a range of more than 9 log units. Some of these adaptation mechanisms are tuned to integrate information slowly, tuning circuits and controlling sensitivity in the course of hours (e.g.circadian regulation of retinal gap junctions (Bloomfield and Volgyi, 2009)) to minutes or seconds (e.g. pupillary reflex). Nevertheless, during free viewing, cones experience light changes that are fast and widely dissimilar even within different regions of the same scene. To be able to make use of small patches of retina efficiently, there is a paramount necessity for fast and local adaptation to the local statistics of inputs, capable of balancing high sensitivity with the risk of saturation (Abrams *et al.*, 2007). The magnitude of this challenge, and the high cost of poor tuning, is made especially apparent when trying to take pictures with current digital cameras: the selection of a single exposure feels far too slow, requires several tries and ends up being very far from optimal to capture more than one region of a scene. The results presented in this work suggest that the visual system deals with a significant fraction of these challenges upfront, by imposing fast local adaptation at every “pixel” or photoreceptor.

3.5.1 Information encoding during eye movements

We find here that the light-adaptation mechanisms in cones are well set to deal with the main challenges imposed by eye movements. First, as light falling on a cone transitions from bright to dim or vice versa, cones show fast changes in gain that occur within a single fixation, helping to preventing saturation of cone responses. Second, these gain changes cause responses to follow Weber's Law (Angueyra and Rieke, 2013), so that at moderate to high mean luminances, responses encode contrast rather than absolute luminance; such encoding is a key aspect of visual perception, allowing us, for example, to see text on a piece of paper as black on white under a huge range of lighting conditions. Third, the rapid gain control is distinct from the slower control of changes in mean current. These slower adaptational changes govern the discrimination of luminances and are important in preserving the biological dynamic range.

Because local luminance and local contrast are near-independent in natural images, luminance and contrast adaptation should ideally operate independently (Frazor and Geisler, 2006). To our knowledge, this is the first time that independent mechanisms of this type have been described in photoreceptors, the first stage of the visual system. Additionally, we have provided evidence that, given the different time scales of the adaptation mechanisms, information about temporal contrast may be available sooner than information about the mean luminance, suggesting that this could be present in downstream neurons and potentially in perception.

3.5.2 Origin of increment/decrement asymmetries

Asymmetries to contrast increments and decrements could arise within the circuitry or directly from light-adaptation in photoreceptors. Psychophysically, threshold for rapid contrast decrements (thought to isolate the Off-pathway) are lower than those for rapid contrast increments (thought to isolate the On pathway) (Bowen *et al.*, 1989). Given that detection of this stimulus requires just a few percent contrast (where cone responses are near linear), the difference in sensitivity has to arise in the circuitry. At higher contrasts, V1 responses in humans and monkeys are still larger for decrements than increments (Kremkow *et al.*, 2014) and detection of 100% contrast decrements embedded in binary noise is better than for 100% contrast increments (Komban *et al.*, 2014); both studies suggest the existence of a nonlinearity early in the visual pathway to

explain these results, which parallels the cone On/Off asymmetries we have shown here. Similarly, asymmetries in cone responses may contribute to other observations made downstream neurons, including the fast gain control (Yeh *et al.*, 1996) and kinetic differences to On and Off contrast (Chichilnisky and Kalmar, 2002) found in primate retinal ganglion cells.

3.5.3 Past evidence for complex nonlinear responses in the primate outer retina

Primate horizontal cells exhibit complex nonlinear responses that include asymmetric responses to symmetric positive and negative contrast and fast gain changes to abrupt changes in luminance *(*Smith *et al., 2001,* Lee *et al., 2003)*. Yet, the location and mechanism of such richness was not explored, and it was unclear if these nonlinearities arise from horizontal cell feedback, properties of the cones synapse or membrane, or in phototransduction itself.

A biophysical model developed to capture horizontal cell responses included three sequential dynamic components (van Hateren, 2005): cone outer segment current, cone inner segment current to voltage conversion, and horizontal cell feedback. The cone outer segment current component of this model included a single feedback mechanism with fast kinetics and is almost identical to the first biophysical model presented above (figure 3.6); this model alone fails to capture the cone current response to naturalistic stimuli. Thus, even though the full model is able to capture most of the characteristics of horizontal cell responses to light steps, flashes and sinusoids, its components are mechanistically misplaced. This hinders the model's ability to infer the relative and specific contributions of each component, especially the transformation performed by horizontal cells.

3.5.4 Mechanistical implications of a second feedback mechanism

Incorporating a slow feedback into a biophysical model for cone transduction allowed us to capture cone responses to steps, flashes and naturalistic stimuli. This slow light-adaptation mechanism likely corresponds to calcium-mediated feedback directly to the cGMP-gated channels for several reasons. First, we have previously shown that in primate cones, the gain changes of the light response caused by light

adaptation do not affect the activity of the cGMP-gated channels. Instead, the modulation of channel activity is relatively weak and requires higher light intensities (Angueyra and Rieke, 2013), suggesting a mechanism that acts directly on the cGMP-gated channels. Second, to recapitulate the cone responses shown here, models need to include a fast and more sensitive adaptation mechanism located upstream of a slower and less sensitive one; models that do not follow this pattern are unable to match the data. Third, and more importantly, *eml*-1*,* a calcium-dependent protein capable of directly modulating cGMP-channel activity has been recently described in bass cones (Rebrik *et al.*, 2012) and genetically identified in zebrafish cones (Korenbrot *et al.*, 2013), providing a compelling mechanistic basis for such feedback. Preliminary experiments suggest that the expression of *eml-1* in primate cones is restricted to the outer segments.

3.5.5 Limits and relevance of the model

Our model does not include any feedback to the opsin or activity of bleached pigment, which are probably not dominant features of the responses shown here. Attempts to include these mechanisms in biophysical models have been described before (Lamb and Pugh, 2004, van Hateren and Lamb, 2006) and are probably important to capture response at higher light levels, where bleaching may be an issue. Nevertheless, the model provided here captures well the characteristics of responses and light adaptation within the range of luminances we tested (up to ~100,000 R*/s for short periods of time).

During the last 15 years, several laboratories have made great efforts to understand what information retinal ganglion cells provide to central targets; among other things, better models of ganglion cell coding could lead to improved retinal prosthetics (Nirenberg and Pandarinath, 2012). Current models can capture RGC responses to specific stimuli well, but fail to generalize, especially to naturalistic stimuli (Lorach *et al.*, 2013). Such models lack dynamic adaptation in individual cones, which we have shown to be important to shape photoreceptor responses. In this context, irrespective of the mechanistical basis of feedback or match between fitted parameters and real parameters, we propose that the model we presented here could help improve

such models, and clarify how computations are implemented by the downstream circuitry.

3.6 Acknowledgements

We thank Greg Horwitz and Bertil Hille for helpful comments, and Mark Cafaro, Shellee Cunnington and Paul Newman for excellent technical assistance. Color scales were developed and made freely available for Matlab by Matteo Niccoli. Support provided by HHMI (FR), the National Eye Institute of the National Institutes of Health (R01EY11850 to FR) and the Computational Training Grant (5R90DA03346103). Retinas were obtained from the Washington National Primate Research Center at the University of Washington, NIH grant RR00166, and from the National Center for Research Resources and the Office of Research Infrastructure Programs (ORIP) of the National Institutes of Health through Grant Number P51 OD 010425. The content is solely the responsibility of the authors and does not necessarily represent the official views of the National Institutes of Health.

Symbol	Parameter	Units	Free	Fit values Fig 6B	Fit values Fig 6D	Fit values Fig 7B	Fit values Fig 7D
σ	Opsin decay time constant	s^{-1}	Free	50	81.06	45.95	71
ϕ	PDE decay time constant	s^{-1}	Free	45	81.06	45.95	65
η	PDE dark activation	s^{-1}	Free	116	123.4784	99.73	116.65
k	cGMP to current constant	μM	Fixed	10^{-3}	10^{-3}	10^{-3}	10^{-3}
h	cGMP channel cooperativity	–	Fixed	3	3	3	3
β	Ca^{2+} extrusion time constant	s^{-1}	Free	180	37.7948	150	180
q	Fraction of current carried by calcium	–	Derived	-	-	-	-
γ_{max}	Maximal cGMP synthesis rate by GC	s^{-1}	Derived	-	-	-	-
K_{GC}	Ca^{2+} GC-affinity	μM	Free	0.235	0.0061	0.2267	0.1759
m	Ca^{2+} GC-cooperativity	–	Free	3.9	4	4	3.3759
β_{Slow}	Ca^{2+} channel decay time constant	s^{-1}	Free	n.a.	n.a.	20.94	7.7242
C_{dark}	Ca^{2+} concentration in darkness	μM	Fixed	0.5	0.5	0.5	0.5
$cGMP_{dark}$	cGMP concentration in darkness	μM	Derived	32.7	24.1	41.2	30.1
I_{dark}	dark current	pA	Measured	-350	-130	-350	-130

Table 3.1. Summary of biophysical model parameters and best fit values

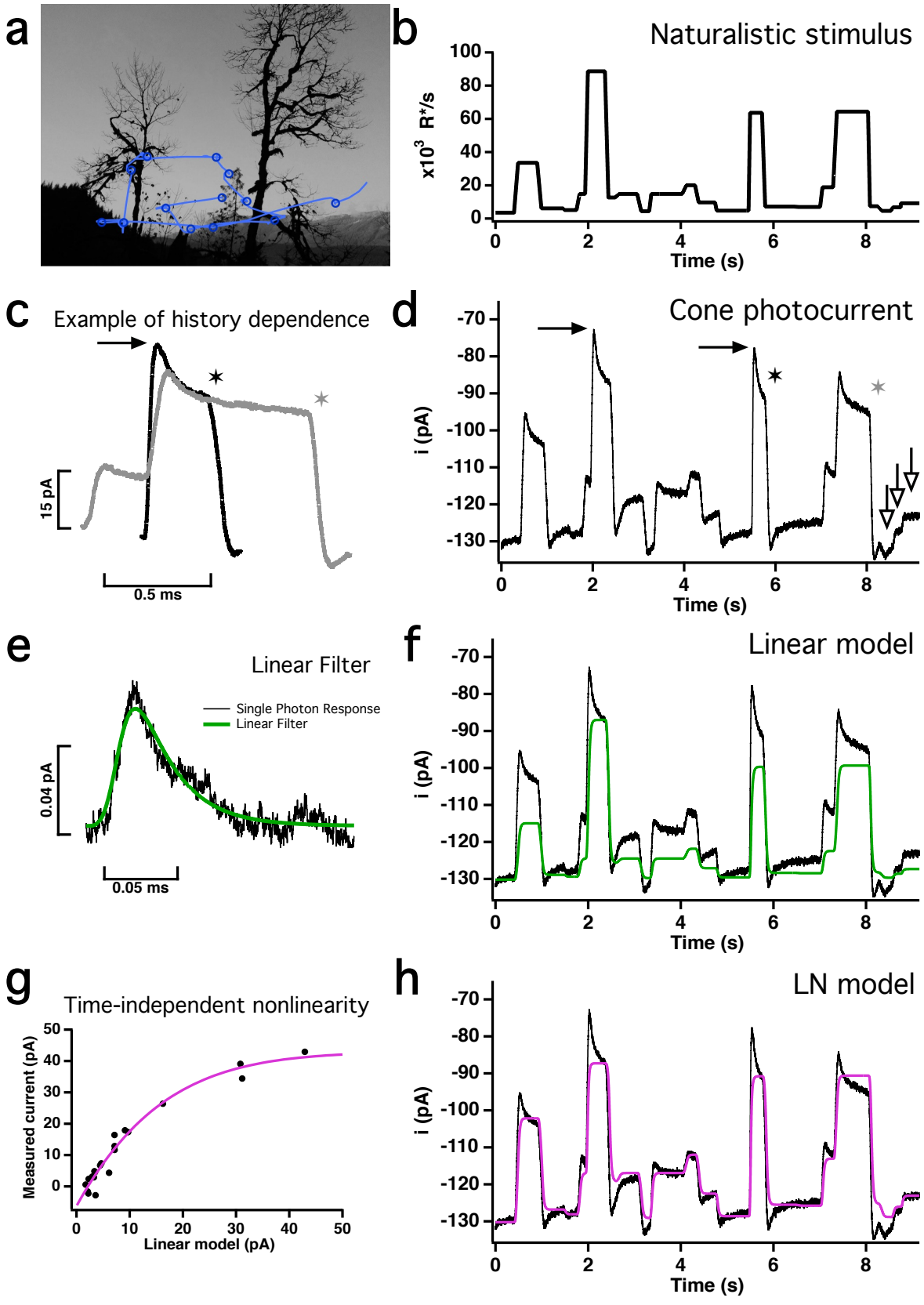
a
b
Naturalistic stimulus
x10^3 R*/s
Time (s)
c
Example of history dependence
15 pA
0.5 ms
d
Cone photocurrent
i (pA)
Time (s)
e
Linear Filter
Single Photon Response
Linear Filter
0.04 pA
0.05 ms
f
Linear model
i (pA)
Time (s)
g
Time-independent nonlinearity
Measured current (pA)
Linear model (pA)
h
LN model
i (pA)
Time (s)

Figure 3.1. The complex responses of primate cones to naturalistic stimuli are not well captured by linear or linear-nonlinear (LN) models

a. Schematic of eye movements (blue line) and fixations (blue circles) during free-viewing of a natural scene.

b. Stimulus that emulates the rapid and frequent changes in mean light intensity experienced by single cones during free-viewing.

c. Responses to same light intensity (asterisks in (a)) were aligned to evidence the differences in peak response and kinetics that depend on the previous light-intensity (history dependence).

d. Photocurrent recording of single cone photoreceptor stimulated with the naturalistic stimulus shown in (a). Responses to such stimuli are highly dynamic and with continual changes in the dynamic range, as shown by the difference in response to the two highest light intensities (solid black arrows) being almost identical to differences in responses to 10-fold dimmer light intensities (open white arrows). Also, responses showed signs of history dependence (asterisks).

e. Linear filter constructed by fitting the estimated single-photon response for cone in (a) with a smooth function (see methods) and used to build a linear model.

f. The linear model (green trace) was rescaled to match the final current at the highest light intensity, but did not match the currents at the rest of light-intensities and did not capture the dynamics of the cone response.

g. Time-independent non-linearity constructed by fitting the relation between the currents at the end of fixations for the measured currents and for the linear model.

h. The nonlinearity in (g) was used to build an LN model (pink trace), which resolves most of the discrepancies of the currents at the end of fixations but does not capture the peak responses nor the dynamics of the cone response.

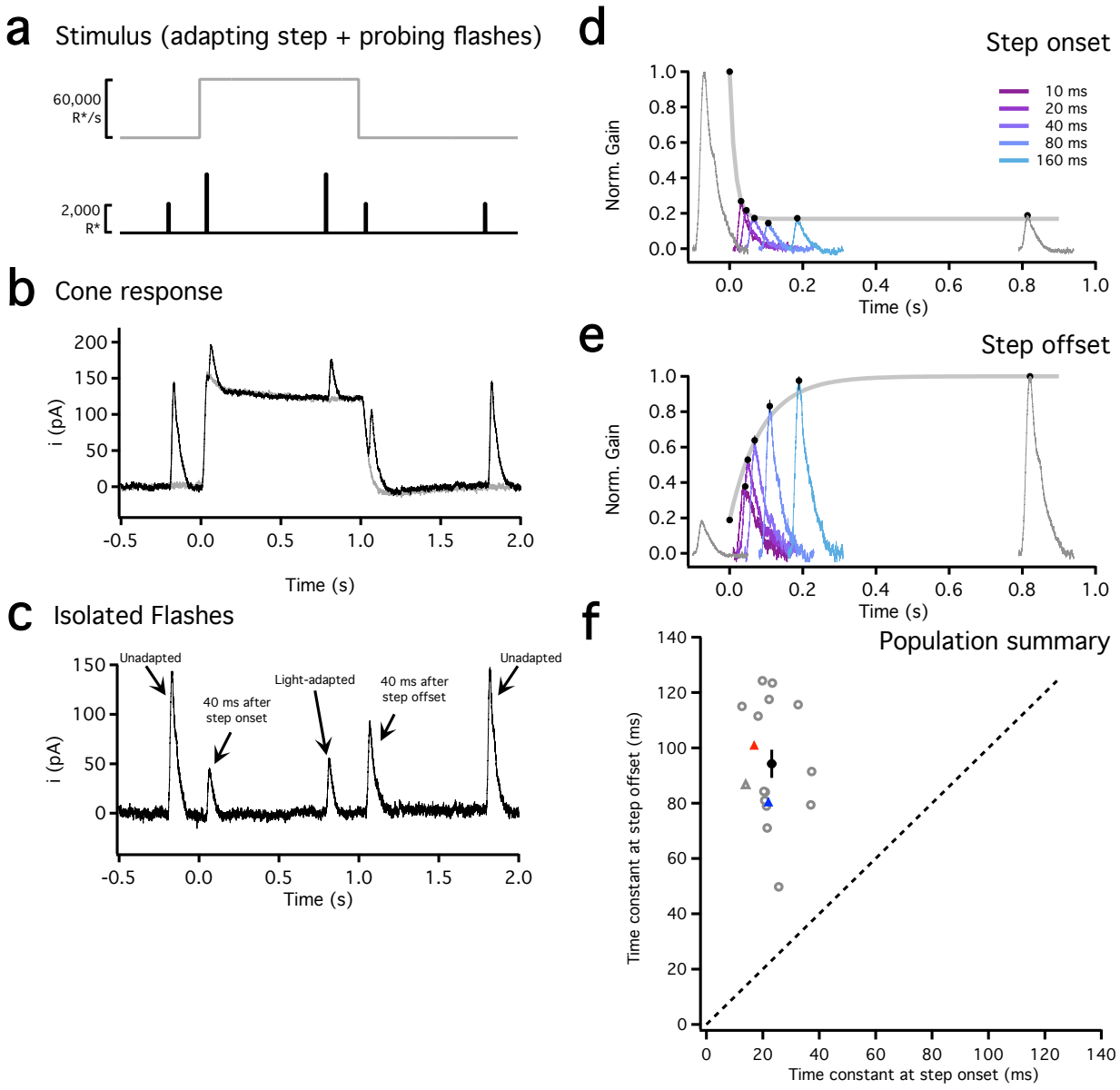

Figure 3.2. Gain changes during light-adaptation are fast and well-tuned to the duration of fixations

a. Stimulus used to probe the kinetics of gain changes during light adaptation, consisting of an adapting step of light (gray trace) and five flashes (black trace); the three flashes delivered before, during and after the light step were fixed in time, while the two other flashes were delivered with variable delays from step onset and offset. Flashes during the step were 2-fold brighter to counteract light-adaptation.

b. Example of mean responses to the adapting step alone (gray trace) or in combination with the five flashes (black trace) with a 40 ms delay for the variable flashes ($n_{trials} = 6$).
c. Flash responses were isolated by subtracting the response to the step alone and subsequently transformed into gain measurements, by dividing by the flash intensity. The flash before and late after the step produced unadapted responses, while the flash during the step produced a light-adapted response, with lower amplitude and faster kinetics. The flashes near step onset and near step offset produced responses that were in transition between the two states.
d. Gain changes at step onset follow very fast kinetics. Gain measurements were normalized to the gain in darkness; gray traces correspond to gain in darkness (leftmost trace) and steady-state adapted gain (rightmost trace). Colored traces correspond to the gain obtained by delivering flashes with a variable delay from the step onset. The speed of the gain changes was tracked by identifying the peaks and approximating their time course with an exponential function. The time constant of best fit was $\tau = 14$ ms (gray smooth line).
e. Gain changes at step offset are slower and more gradual. Gray traces correspond to steady state adapted gain (leftmost trace) and gain in darkness (rightmost trace). Colored traces correspond to the gain obtained by delivering flashes with a variable delay from the step offset. The time constant of best fit to an exponential function was $\tau = 86$ ms (gray smooth line).
f. Time constants at step onset were 3 to 4-fold faster than at step offset over a population of cells (n = 15). Mean and SEM are shown as black circle and error bars, individual cells are shown as gray open circles and example cell in (a-d) is shown as gray open triangle. All cells lie above the unity line (blacked dashed line). Notice that both onset and offset time constants are shorter the average duration of fixations during free-viewing (200 to 600 ms). The corresponding time constants for the biophysical models (figures 3.4 and 3.5) are shown as solid triangles (blue triangle for model with 1 adaptation mechanism, red triangle for model with 2 adaptation mechanisms).

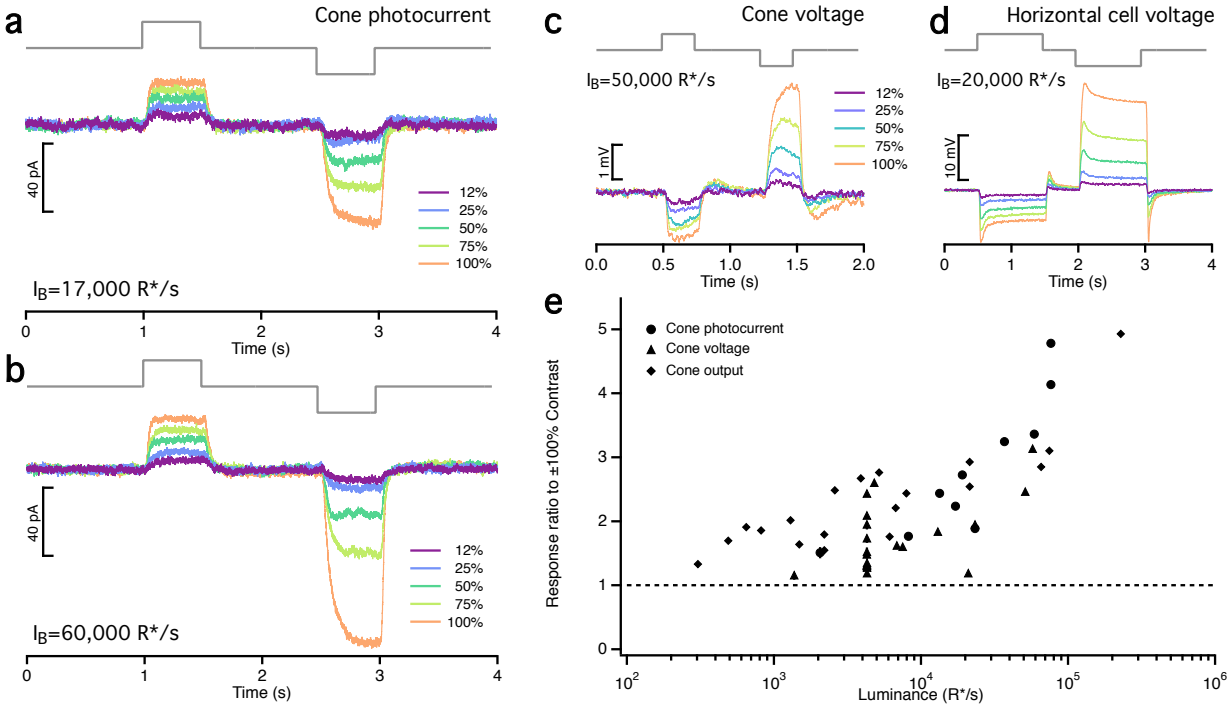

Figure 3.3. Cones exhibit On/Off asymmetries that arise within the phototransduction cascade and are transmitted downstream

a. Cone photocurrent recording at a background light intensity of 17,000 R*/s, with larger responses to luminance decrements compared to symmetric luminance increments, for Weber contrasts above 25%.

b. Same cone as in (a) but at a background light intensity of 60,000 R*/s. The asymmetry in responses gets larger as background light intensity (and light-adaptation) increases.

c. Cone voltage recording at a background light intensity of 50,000 R*/s also shows asymmetric responses with similar characteristics.

d. Voltage recording of horizontal cell at a background light intensity of 20,000 R*/s, shows that the asymmetries in cone responses are transmitted to downstream neurons.

e. Ratio of steady-state responses to 100% contrast for cone currents (circles), cone voltages (triangles) or horizontal cell voltage (diamonds) over a wide range of background light intensities. All cells showed larger responses to contrast decrements (all ratios are larger than 1).

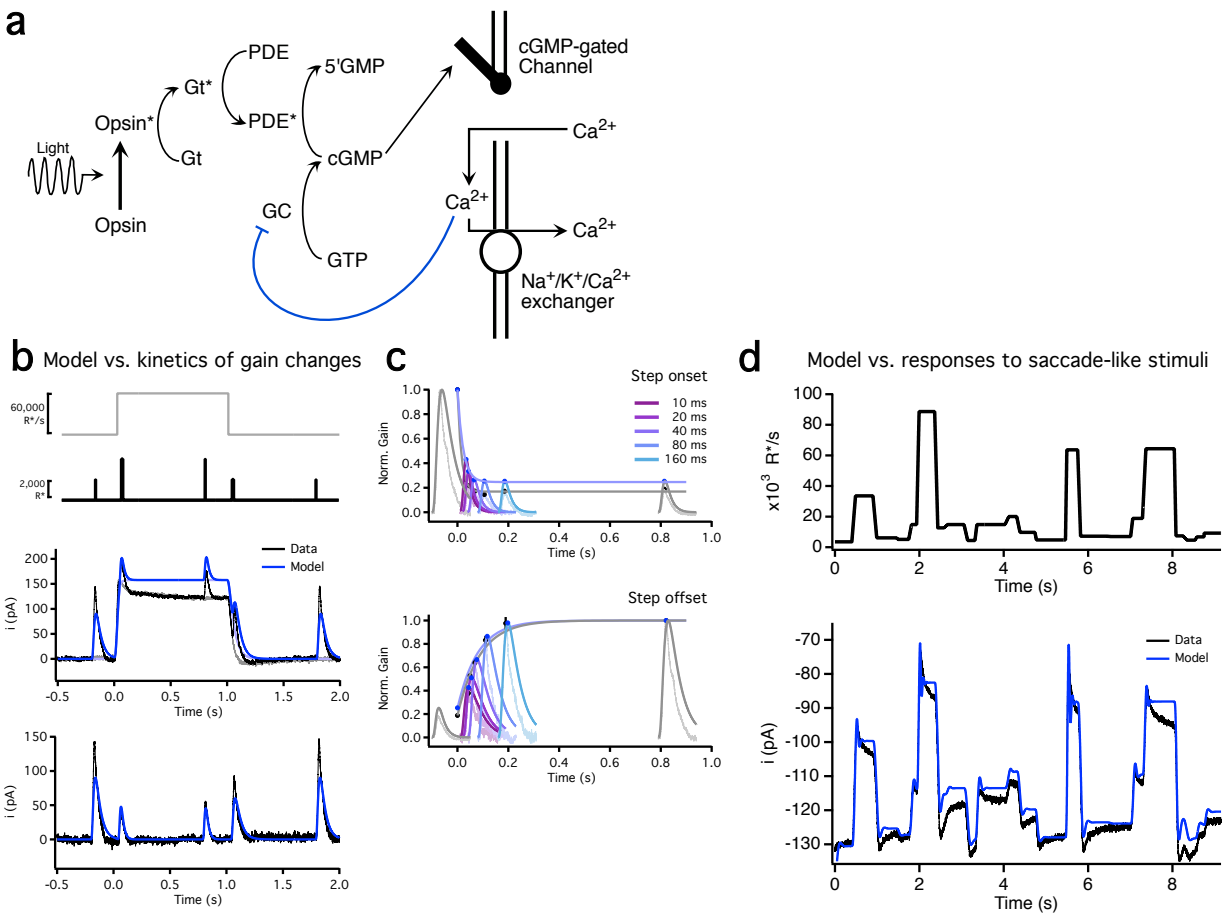

Figure 3.4. A biophysical model with a single feedback mechanism is unable to capture cone responses

a. Schematic of phototransduction cascade and corresponding components of the biophysical model: cyclic-GMP (cGMP) is constantly synthesized by guanylate cyclase (GC), opening cGMP-gated channels in the membrane. Light-activated opsin (Opsin*) activates the G-protein transducin (Gt*) which then is able to relieve inhibition from phosphodiesterase (PDE*) and decreases the cGMP concentration, producing closing of the cGMP-channels. Calcium ions (Ca^{2+}) flow into the cone outer segment through the cGMP-gated channels and are extruded through $Na^{+}/K^{+}/Ca^{2+}$ exchangers in the membrane. In this model, the main feedback mechanism (blue line) arises from Ca^{2+}-dependence in the rate of cGMP-synthesis through GC.

b. Model fit to responses to step and flashes shown in figure 3.2. Model was able to produce similar gain changes but did not capture the slower kinetics of step response, and the flash responses had slow recovery to baseline. See table 3.1 for fit parameters.

c. Kinetics of model gain changes are well matched to the data. Kinetics of gain changes estimated as in figure 3.2 had a time constant of 22 ms at step onset and of 80 ms at step offset.

d. Model fit to cone response to the saccade-like stimulus shown in figure 3.1, shows improvement over the linear and LN models, but is still unable to capture the currents at the end of fixations and has an oscillating light response to steps and flashes. See table 3.1 for fit parameters.

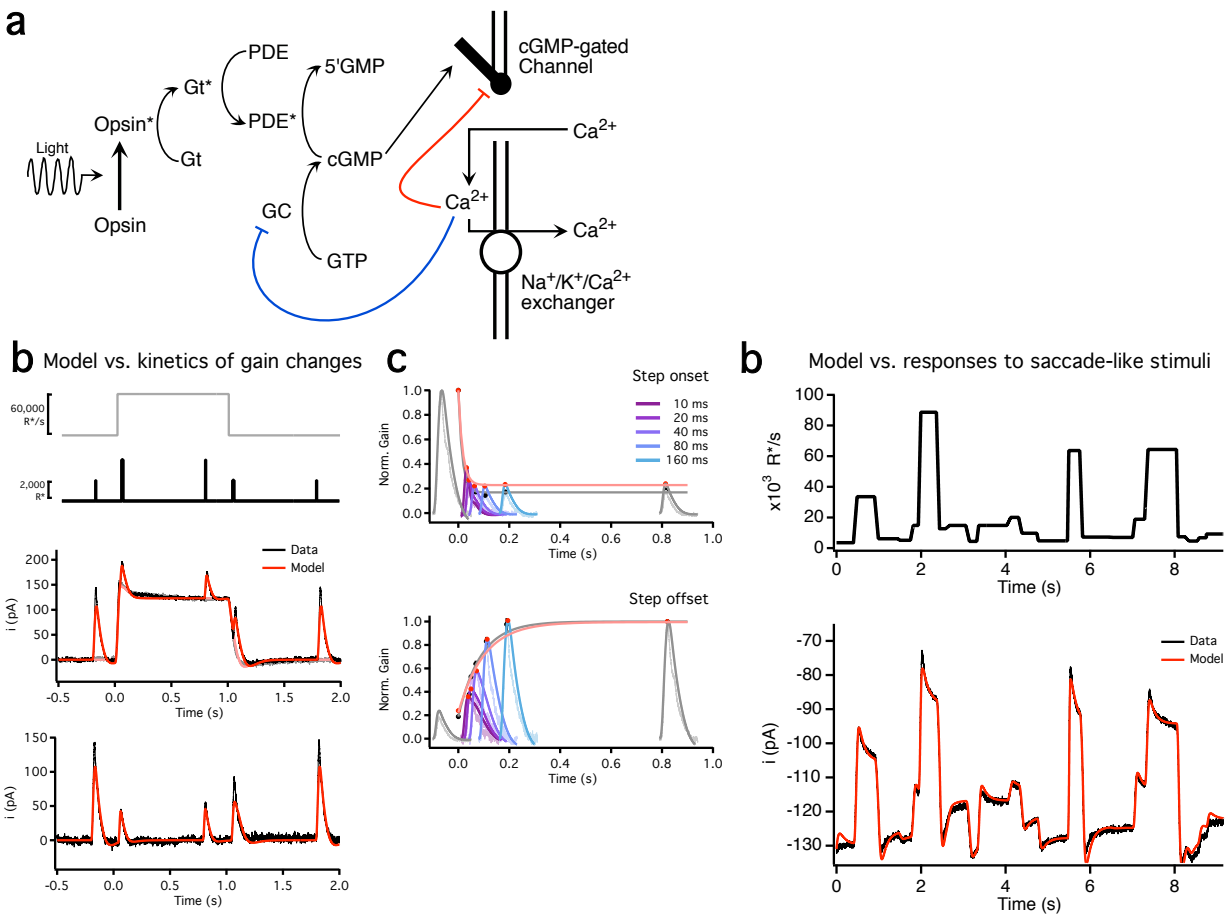

Figure 3.5. A biophysical model with two distinct feedback mechanisms is able to capture cone responses

a. Schematic of phototransduction cascade and corresponding components of the biophysical model. The second and slower feedback mechanism (red line) is arises from calcium feedback to the cGMP-gated channels.

b. Model fit to responses to step and flashes shown in figure 3.2. Model was able to simultaneously replicate the step and flash responses and the gain changes. See table 3.1 for fit parameters.

c. Kinetics of model gain changes are also well matched to the data, with a time constant of 17 ms at step onset and 100 ms at step offset.

d. Model fit to cone response to the saccade-like stimulus shown in figure 3.1. This model is able to capture currents at all fixations, with correct dynamic changes and history dependence. See table 3.1 for fit parameters.

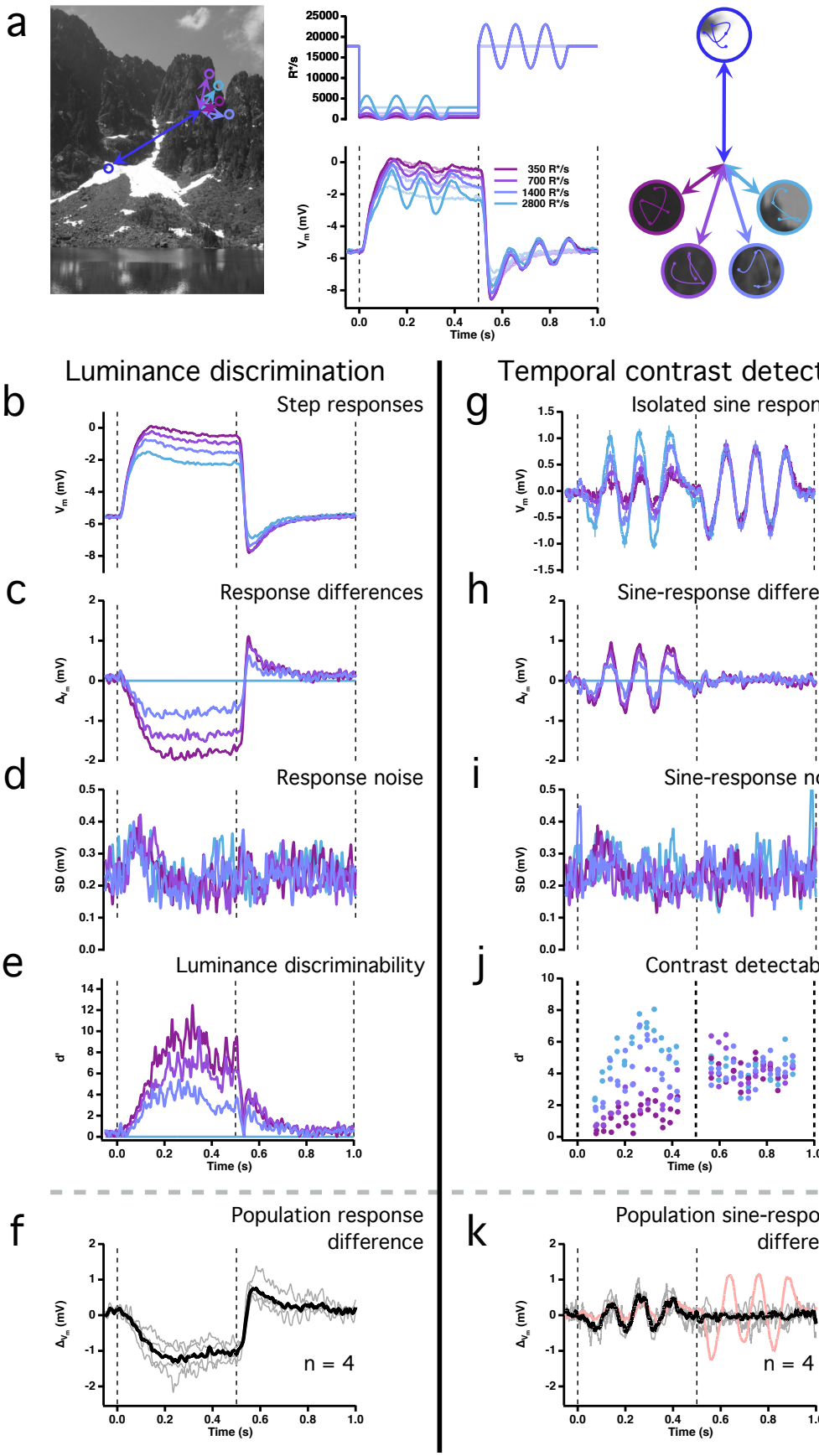
a
R*/s
25000
20000
15000
10000
5000
0
V_m (mV)
0
-2
-4
-6
-8
350 R*/s
700 R*/s
1400 R*/s
2800 R*/s
0.0
0.2
0.4
0.6
0.8
1.0
Time (s)
Luminance discrimination
b
Step responses
c
Response differences
d
Response noise
e
Luminance discriminability
f
Population response difference
n = 4
Temporal contrast detection
g
Isolated sine responses
h
Sine-response difference
i
Sine-response noise
j
Contrast detectability
k
Population sine-response difference
n = 4

Figure 3.6. Discrimination of luminance and detection of temporal contrast during eye movements follow different time courses

a. Schematic of experiment design: **(left)** During exploration of natural scenes, saccades are frequently made from a bright region (blue circle) to darker regions (purple and light blue circles), and back to a bright region, producing abrupt changes in the mean luminance experienced by cones . **(middle)** We emulated the luminance changes experienced in these conditions as steps that begin at a relatively high light intensity (18,000 R*/s) and abruptly decrease to one of four lower light intensities (350 R*/s, 700 R*/s, 1,400 R*/s or 2,800 R*/s) and back to the high light intensity, and recorded cone voltage responses to such stimuli (light colors). **(right)** During fixations at any of these regions, fixational eye movements paired with the fine spatial structure of natural images cause dynamic changes in contrast. **(middle)** This was emulated as a 5 Hz sinusoidal modulation to the luminance changes; we tested 4 different sinusoid phases (only 1 shown) and sinusoid contrast was 100% at the lower light intensities and 30% at the high light intensity to produce similar responses (bright colors).

(**b-f)** Luminance discrimination

b. Mean cone voltage responses to the luminance steps in (a) ($n_{trials} = 5$). Abrupt decreases to different low light-intensities produce responses that rise similarly in the first ~50 ms and slowly diverge; upon return to the high light intensity, the peak responses differ depending on the previous light intensity to then reach the same steady-state value.

c. Each response was subtracted from the response to 2,800 R*/s, highlighting that the larger differences between responses are reached after the voltage responses have settled and that upon return to the high light intensity, the differences decay slowly, over the course of ~200 ms.

d. Noise across the mean responses in (a) is flat with little stimulus-dependence and equal magnitude at all light intensities.

e. The time course of discrimination across luminances (measured as d' and taking the response to 2,800 R*/s as reference) closely follows (c), with largest discrimination across low luminances beyond 200 ms (when responses have reached steady-state).

Upon return to the high light intensity, discriminability (i.e. hysteresis) also decays slowly over the course of ~200 ms.

f. Mean response difference as in (c) for a population of cells (black line, n = 4). Individual cells are shown in gray. All cells display a slow build-up at the low light intensities and a slowly decaying difference upon return to the high light intensity.

(g-k) Temporal contrast detection

g. The response to the sinusoidal stimulation was isolated by subtracting the response to the steps alone. At each low light intensity only the peak response to the first half cycle differed from the rest, with a steady state response already reached by the peak of the second half cycle (which occurred before 200 ms); upon return to the high light intensity, steady state was even reached before the peak response to the first half-cycle.

h. Each sinusoidal response was subtracted from the response to modulation at the 2,800 R*/s light intensity, showing that at the low light intensities, the amplitude of the responses to 100% Weber-contrast sinusoidal modulation is directly related to light intensity; upon return to the high light intensity, no differences across responses could be found, even when there are clear differences in the underlying response to the luminance steps (compare to (c)).

i. As in (d), noise across responses has little stimulus dependence.

j. The detection of temporal contrast (measured as d' respect to the underlying step response) was evaluated at the peak of the sine responses across 4 different phases and showed the same time course as in (g). The most notable effect was that, upon return to the high light intensity, detection was high even by the first peak of the sine response irrespective of the previous low luminance (i.e. sine responses did not show history-dependence).

k. Mean differences in sine responses (black trace) and individual cells (gray trace) as in (g) for the same population of cells as in (f). No differences were found upon return to the high light level, even though there was a robust response to the sinusoidal modulation itself (red trace).

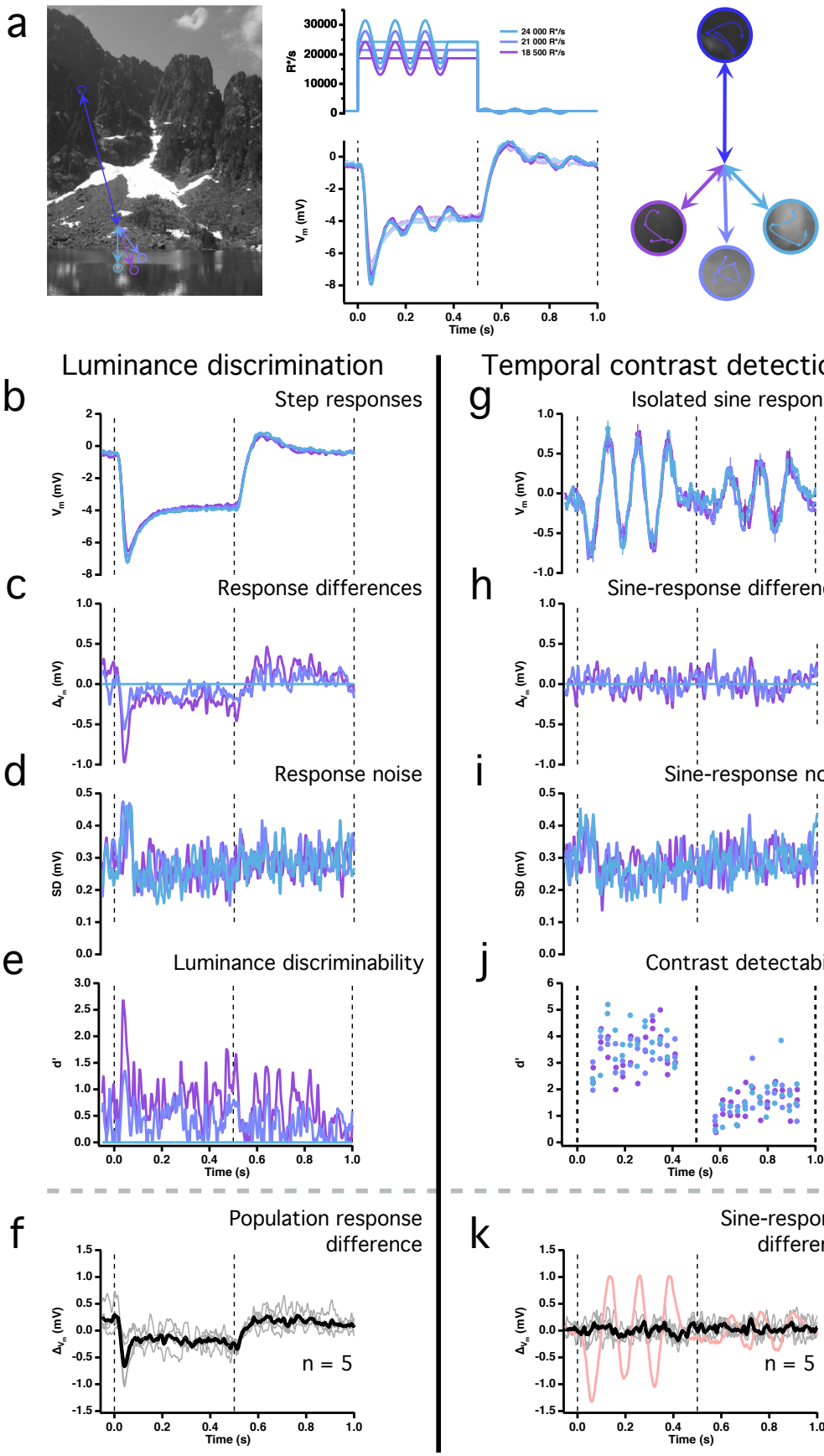
a
30000
20000
10000
0
R*/s
24 000 R*/s
21 000 R*/s
18 500 R*/s
0
-2
-4
-6
-8
V_m (mV)
0.0
0.2
0.4
0.6
0.8
1.0
Time (s)
Luminance discrimination
Temporal contrast detection
b
Step responses
g
Isolated sine responses
c
Response differences
h
Sine-response differences
d
Response noise
i
Sine-response noise
e
Luminance discriminability
j
Contrast detectability
d'
f
Population response difference
k
Sine-response difference
n = 5
n = 5

Figure 3.7. Discrimination of luminance and detection of temporal contrast during eye movements have different sensitivities

a. Schematic of experiment design: **(left)** During exploration of natural scenes, saccades are frequently made from a dark region (blue circle) to brighter regions (purple and light blue circles), and back to a dark region, producing abrupt changes in the luminance experienced by cones . **(middle)** We emulated the luminance changes experienced in these conditions as steps that begin at a low light intensity (700 R*/s) and abruptly increase to one of three high light intensities (18,500 R*/s, 21,000 R*/s or 24,000 R*/s) and back to the low light intensity, and recorded cone voltage responses to such stimuli (light colors). **(right)** During fixations at any of these regions, fixational eye movements paired with the fine spatial structure of natural images cause dynamic changes in contrast. **(middle)** We superimposed a 5 Hz sinusoidal modulation to the luminance changes and tested 4 different sinusoid phases (only 1 shown); sinusoid contrast was 100% at the low light intensity and 30% at the higher light intensities (bright colors).

(b-f) Luminance discrimination

b. Mean cone voltage responses to the luminance steps in (a) (n_{trials}=5). Abrupt increases to different high light-intensities produce very similar responses with noticeable differences only at the response peak.

c. Each response was subtracted from the response to 24,000 R*/s, highlighting the differences in peak response at light-intensity increase and the small differences in the rest of the responses.

d. Noise across the mean responses in (a) has a brief increase at the peak of the response then becomes flat and of equal magnitude at all light intensities.

e. Discrimination across luminances (measured as d' and taking the response to 24,000 R*/s as reference) is only briefly noticeable at the peak of the response in the first 50 ms.

f. Mean response difference as in (c) for a population of cells (black line, n = 5). Individual cells are shown in gray. All cells display clear differences only at the peak of the response, suggesting that 29% differences in bright light-intensities are difficult to discriminate.

(g-k) Temporal contrast detection

g. The response to the sinusoidal stimulation was isolated by subtracting the response to the luminance steps alone. At the high light intensities, the 30% contrast sinusoidal modulation produced robust responses, with steady-state reached before the peak response to the first half-cycle; at luminance decrease, the peak response to the first half-cycle of the 100% contrast modulation was inhibited.

h. Each sinusoidal response was subtracted from the response to modulation at the 24,000 R*/s light intensity, showing negligible differences across luminances, even though in absolute values, the sinusoidal modulation differed by 14% and 29% (in other words, the sine responses were constant respect to contrast).

i. As in (d), noise across responses is flat except briefly at the step response peak..

j. The discrimination of contrast (measured as d' respect to the underlying step response) was evaluated at the peak of the sine responses across 4 different phases and showed the same time course as in (g).

k. Mean differences in sine responses (black trace) and individual cells (gray trace) as in (g) for the same population of cells as in (f), highlighting the contrast constancy of the responses by the negligible differences across light intensities (red trace). At the high light intensities, the 30% Weber-contrast sinusoidal modulation produced robust responses while 29% modulation in mean luminance produced small differences in mean response, suggesting that contrast discrimination has a higher sensitivity.

Chapter 4
Concluding remarks

I consider the main strength of work presented in this dissertation stems from rooting the study of phototransduction through the perspective of visual function. In chapter 2, I estimated the dark noise in single cones, finding a close agreement with behavioral estimates of dark noise. I also quantified how cone signals and cone noise change as the background illumination increases and showed that the signal-to-noise ratio in cones follows the same shape as the behavioral signal-to-noise ratio for the detection of dim flashes. In chapter 3, I explored how cones respond to stimuli that emulate the changes in input encountered during eye movements, uncovering the relevance of two distinct adaptation mechanisms within the phototransduction cascade. The different kinetics and sensitivities of these mechanisms impose specific constraints on the encoding of information performed by cones; to help with the exploration of how the downstream circuit is able to decode and recode this information, I provided a model able to capture cone responses to a wide array of stimuli.

4.1 Filling a gap in our current understanding: sources of noise in primate cones

The fact that cone noise in primates is not dominated by spontaneous opsin activation was shown more than a decade ago (Schneeweis and Schnapf, 1999), but the issue was left untouched since then and has still not fully permeated the field for several reasons. First, sources of noise in phototransduction have been extensively studied in rods, where spontaneous rhodopsin activation is a dominant source of noise (Baylor *et al.*, 1980, Baylor *et al.*, 1984) and traditionally cones have been considered less sensitive rods. Second, M- and L-opsins are less stable and have higher predicted rates of spontaneous activation (Barlow, 1956). And third, previous quantifications of cone noise (Lamb and Simon, 1977, Schneeweis and Schnapf, 1999) exceed noise measured behaviorally, detracting from the relevance of these physiological studies (Donner, 1992, Koenig and Hofer, 2011). The work presented in chapter 2 was designed to tackle these issues at their root, by first identifying mechanistically how noise arises in cones, in the hope that this would lead to a resolution between the physiological and

behavioral discrepancies. It is important to point out that the light responses presented in this dissertation are quite different from previous publications, with major improvements in sensitivity (the peak amplitude of estimated single-photon responses in Schnapf *et. al*, 1990 is ~30fA/R* *vs.* ~150fA/R* for figure 1.4 in this dissertation) and a decrease in the biphasic nature (compare with responses in Schnapf *et. al*, 1990). We think these differences may arise from improvements in the dissection procedure, and from changes in the storage and recording solutions and temperatures (Azevedo and Rieke, 2011); similar results have also been obtained independently in other laboratories (Cao *et al.*, 2014).

4.2 Providing a tool for the retina and vision community: cone biophysical model

The work presented in chapter 3 started as a search for a model that would capture the responses of cones to arbitrary stimuli. I considered this to be an important endeavor as most of the current models used to describe the responses in retinal ganglion cells treat photoreceptors as a simple linear filter and fail to generalize to responses to naturalistic stimuli. Perhaps, some of these failures stem from an inadequate treatment of cones and the subsequent lack of adaptation and other non-linearities at small spatial scales, and may change the interpretations of computations performed (or not) by the retinal circuitry.

In our first attempts, we built LN-models using stimulation with low-contrast gaussian white noise (Chichilnisky, 2001) finding that a purely linear model was accurate. Nevertheless, linear and LN-models proved insufficient at capturing responses at high contrasts or any other condition capable of modulating the light-adaptation mechanisms (Figure 3.1). It was this realization that led, not only to study cone responses during eye movements, where light-adaptation would be modulated strongly, but also to explore biophysical models. As demonstrated, the biophysical model proposed in this dissertation is able to capture cone responses to our naturalistic stimuli (Figure 3.5), but many issues are still unresolved. First, none of the parameters I used for the model fitting have been directly measured in primate cones, and instead I relied on measurements from either rod or cone photoreceptors from a variety of species to constrain or fix the different parameters. Second, the fits of the biophysical

model are not unique, such that very different sets of parameters are able to capture the responses of cones. Third, it is difficult to find sets of model-parameters that generalize well, as I have found significant variations in dark-current (compare figures 2.2, 2.3 and 2.4 for example) and sensitivity (measured by the peak amplitude of the estimated single-photon response) across cells. The analysis and interpretations in this dissertation have been restricted to cones with high-sensitivity and stable responses during recording, hoping to mitigate some of the experimental variability, and to better reflect the *in vivo* responses, which are still expected to contain real biological variability (Harmening *et al.*, 2014).

Several improvements can be made in this model. First, measurement of parameters included in the model would provide better constraints and more importantly more insights on the inner working of phototransduction in cones. Second, to address biological variability and generalization of the model, it will be important to not only measure single parameters but also provide a sense on their variability from cone to cone. Third, although the stimuli presented above explore a wide range of light-intensities, accumulation of bleached opsin is low (given maximal light-intensities of $\sim 10^5$ R*/s, recording durations of less than 10 min and estimated concentration of opsin of $\sim 10^9$/cone, bleaching in our recording is less than 1%). It will be important to explore how cone responses change at higher light-levels, where bleaching is an issue, and include additional components of opsin regulation to the present model. Fourth, to capture voltage responses in cones, we added a simple linear current-to-voltage conversion, still obtaining good fits; nevertheless, nonlinearities in current-to-voltage conversion have been described and modeled previously (Detwiler *et al.*, 1980). Similar measurements could be directly made in primate cones and subsequently implemented in the model. In the future, extending our knowledge and modeling efforts into the cone synapse and horizontal-cell feedback will be valuable.

4.3 Detection of mean luminance vs. detection of luminance modulation

One of the most interesting findings presented in this dissertation is the slower speed in the discrimination of mean luminance compared to the detection of modulations about this mean luminance (Chapter 3). It is possible that such dichotomy

may be inherited by the downstream retinal circuitry and could be present even behaviorally. Preliminary experiments in ganglion cells stimulated with the same stimulus paradigm (luminance steps with or without sinusoidal modulation) show a similar result in ON-midgets. Experiments to explore this psychophysically are currently underway.

4.4 Insights provided by noise analysis

As a final concluding remark, I want to highlight how powerful noise analysis is. Noise analysis in the past has provided deep insight into the gating of ion channels (Conti *et al.*, 1976, Neher and Stevens, 1977), into the underlying mechanism mediating long-term potentiation in hippocampus (Andrasfalvy and Magee, 2004) and into the coupling and noise sources of phototransduction at a time where its actual components had not been discovered (Yau *et al.*, 1979). With considerably more knowledge about the phototransduction cascade, I was still able to use a similar approach to identify the different sources of noise in cone phototransduction. Additionally, the independence of channel noise to gain changes during light-adaptation was the first suggestion of the relevance of a second light-adaptation mechanism in the phototransduction cascade. For these reasons, I consider that a similar approach would be extremely helpful to revolve some of the current controversies on the mechanism of horizontal-cell feedback: (for example Wang *et al.*, 2014 *vs.* Vroman *et al.*, 2013 and Vroman *et al.*, 2014) or, similarly, to explore less well-known transduction cascades, such as the metabotropic glutamate-receptor cascade in ON-bipolar cells.

Bibliography

Abrams, A. B., Hillis, J. M. & Brainard, D. H. The relation between color discrimination and color constancy: when is optimal adaptation task dependent? *Neural Comput* **19**, 2610-2637 (2007).

Ala-Laurila, P., Greschner, M., Chichilnisky, E. J. & Rieke, F. Cone photoreceptor contributions to noise and correlations in the retinal output. *Nat Neurosci* **14**, 1309-1316 (2011).

Andrasfalvy, B. K. & Magee, J. C. Changes in AMPA receptor currents following LTP induction on rat CA1 pyramidal neurones. *J Physiol* **559**, 543-554 (2004).

Angueyra, J. M. & Rieke, F. Origin and effect of phototransduction noise in primate cone photoreceptors. *Nat Neurosci* **16**, 1692-1700 (2013).

Azevedo, A. W. & Rieke, F. Experimental protocols alter phototransduction: the implications for retinal processing at visual threshold. *J Neurosci* **31**, 3670-3682 (2011).

Banks, M. S., Geisler, W. S. & Bennett, P. J. The physical limits of grating visibility. *Vision Res* **27**, 1915-1924 (1987).

Barlow, H. B. Retinal noise and absolute threshold. *J Opt Soc Am* **46**, 634-639 (1956).

Baylor, D. A., Matthews, G. & Yau, K. W. Two components of electrical dark noise in toad retinal rod outer segments. *J Physiol* **309**, 591-621 (1980).

Baylor, D. A., Nunn, B. J. & Schnapf, J. L. The photocurrent, noise and spectral sensitivity of rods of the monkey Macaca fascicularis. *J Physiol* **357**, 575-607 (1984).

Baylor, D. A., Nunn, B. J. & Schnapf, J. L. Spectral sensitivity of cones of the monkey Macaca fascicularis. *J Physiol* **390**, 145-160 (1987).

Bialek, W. & Setayeshgar, S. Physical limits to biochemical signaling. *Proc Natl Acad Sci U S A* **102**, 10040-10045 (2005).

Bloomfield, S. A. & Volgyi, B. The diverse functional roles and regulation of neuronal gap junctions in the retina. *Nat Rev Neurosci* **10**, 495-506 (2009).

Borghuis, B. G., Sterling, P. & Smith, R. G. Loss of sensitivity in an analog neural circuit. *J Neurosci* **29**, 3045-3058 (2009).

Bowen, R. W., Pokorny, J. & Smith, V. C. Sawtooth contrast sensitivity: decrements have the edge. *Vision Res* **29**, 1501-1509 (1989).

Burkhardt, D. A. Light adaptation and photopigment bleaching in cone photoreceptors in situ in the retina of the turtle. *J Neurosci* **14**, 1091-1105 (1994).

Cao, L. H., Luo, D. G. & Yau, K. W. Light responses of primate and other mammalian cones. *Proc Natl Acad Sci U S A* **111**, 2752-2757 (2014).

Carde, R. T. & Willis, M. A. Navigational strategies used by insects to find distant, wind-borne sources of odor. *J Chem Ecol* **34**, 854-866 (2008).

Chichilnisky, E. J. A simple white noise analysis of neuronal light responses. *Network* **12**, 199-213 (2001).

Chichilnisky, E. J. & Kalmar, R. S. Functional asymmetries in ON and OFF ganglion cells of primate retina. *J Neurosci* **22**, 2737-2747 (2002).

Conti, F., Hille, B., Neumcke, B., Nonner, W. & Stampfli, R. Measurement of the conductance of the sodium channel from current fluctuations at the node of Ranvier. *J Physiol* **262**, 699-727 (1976).

Curcio, C. A. & Sloan, K. R. Packing geometry of human cone photoreceptors: variation with eccentricity and evidence for local anisotropy. *Vis Neurosci* **9**, 169-180 (1992).

De Valois, R. L. & Jacobs, G. H. Primate color vision. *Science* **162**, 533-540 (1968).

Demb, J. B. Functional circuitry of visual adaptation in the retina. *J Physiol* **586**, 4377-4384 (2008).

Detwiler, P. B., Hodgkin, A. L. & McNaughton, P. A. Temporal and spatial characteristics of the voltage response of rods in the retina of the snapping turtle. *J Physiol* **300**, 213-250 (1980).

Donner, K. Noise and the absolute thresholds of cone and rod vision. *Vision Res* **32**, 853-866 (1992).

Donner, K., Copenhagen, D. R. & Reuter, T. Weber and noise adaptation in the retina of the toad Bufo marinus. *J Gen Physiol* **95**, 733-753 (1990).

Dunn, F. A., Lankheet, M. J. & Rieke, F. Light adaptation in cone vision involves switching between receptor and post-receptor sites. *Nature* **449**, 603-606 (2007).

Endeman, D. & Kamermans, M. Cones perform a non-linear transformation on natural stimuli. *J Physiol* **588**, 435-446 (2010).

Fechner, G. T. Elemente dur Psychophysik. (1860).

Fettiplace, R. & Ricci, A. J. Adaptation in auditory hair cells. *Curr Opin Neurobiol* **13**, 446-451 (2003).

Field, G. D. & Rieke, F. Mechanisms regulating variability of the single photon responses of mammalian rod photoreceptors. *Neuron* **35**, 733-747 (2002).

Field, G. D., Sampath, A. P. & Rieke, F. Retinal processing near absolute threshold: from behavior to mechanism. *Annu Rev Physiol* **67**, 491-514 (2005).

Frazor, R. A. & Geisler, W. S. Local luminance and contrast in natural images. *Vision Res* **46**, 1585-1598 (2006).

Fu, Y., Kefalov, V., Luo, D. G., Xue, T. & Yau, K. W. Quantal noise from human red cone pigment. *Nat Neurosci* **11**, 565-571 (2008).

Fu, Y. & Yau, K. W. Phototransduction in mouse rods and cones. *Pflugers Arch* **454**, 805-819 (2007).

Geisler, W. S. Contributions of ideal observer theory to vision research. *Vision Res* **51**, 771-781 (2011).

Graham, N. & Hood, D. C. Quantal noise and decision rules in dynamic models of light adaptation. *Vision Res* **32**, 779-787 (1992).

Harmening, W. M., Tuten, W. S., Roorda, A. & Sincich, L. C. Mapping the perceptual grain of the human retina. *J Neurosci* **34**, 5667-5677 (2014).

Harris, C. M., Hainline, L., Abramov, I., Lemerise, E. & Camenzuli, C. The distribution of fixation durations in infants and naive adults. *Vision Res* **28**, 419-432 (1988).

Harris, C. M. & Wolpert, D. M. The main sequence of saccades optimizes speed-accuracy trade-off. *Biol Cybern* **95**, 21-29 (2006).

Holcman, D. & Korenbrot, J. I. The limit of photoreceptor sensitivity: molecular mechanisms of dark noise in retinal cones. *J Gen Physiol* **125**, 641-660 (2005).

Hornstein, E. P., Verweij, J., Li, P. H. & Schnapf, J. L. Gap-junctional coupling and absolute sensitivity of photoreceptors in macaque retina. *J Neurosci* **25**, 11201-11209 (2005).

Kawamura, S. & Tachibanaki, S. Rod and cone photoreceptors: molecular basis of the difference in their physiology. *Comp Biochem Physiol A Mol Integr Physiol* **150**, 369-377 (2008).

Kefalov, V. J. et al. Breaking the covalent bond--a pigment property that contributes to desensitization in cones. *Neuron* **46**, 879-890 (2005).

Kelliher, K. R., Ziesmann, J., Munger, S. D., Reed, R. R. & Zufall, F. Importance of the CNGA4 channel gene for odor discrimination and adaptation in behaving mice. *Proc Natl Acad Sci U S A* **100**, 4299-4304 (2003).

Klein, S. A. & Levi, D. M. Hyperacuity thresholds of 1 sec: theoretical predictions and empirical validation. *J Opt Soc Am A* **2**, 1170-1190 (1985).

Koenig, D. & Hofer, H. The absolute threshold of cone vision. *J Vis* **11**, (2011).

Komban, S. J. et al. Neuronal and perceptual differences in the temporal processing of darks and lights. *Neuron* **82**, 224-234 (2014).

Korenbrot, J. I. Speed, sensitivity, and stability of the light response in rod and cone photoreceptors: facts and models. *Prog Retin Eye Res* **31**, 442-466 (2012).

Korenbrot, J. I., Mehta, M., Tserentsoodol, N., Postlethwait, J. H. & Rebrik, T. I. EML1 (CNG-modulin) controls light sensitivity in darkness and under continuous illumination in zebrafish retinal cone photoreceptors. *J Neurosci* **33**, 17763-17776 (2013).

Korenbrot, J. I. & Rebrik, T. I. Tuning outer segment Ca2+ homeostasis to phototransduction in rods and cones. *Adv Exp Med Biol* **514**, 179-203 (2002).

Kremkow, J. et al. Neuronal nonlinearity explains greater visual spatial resolution for darks than lights. *Proc Natl Acad Sci U S A* **111**, 3170-3175 (2014).

Krizaj, D. & Copenhagen, D. R. Calcium regulation in photoreceptors. *Front Biosci* **7**, d2023-44 (2002).

Kuang, X., Poletti, M., Victor, J. D. & Rucci, M. Temporal encoding of spatial information during active visual fixation. *Curr Biol* **22**, 510-514 (2012).

Lamb, T. D. & Pugh, E. N. J. Dark adaptation and the retinoid cycle of vision. *Prog Retin Eye Res* **23**, 307-380 (2004).

Lamb, T. D. & Simon, E. J. Analysis of electrical noise in turtle cones. *J Physiol* **272**, 435-468 (1977).

Lee, B. B., Dacey, D. M., Smith, V. C. & Pokorny, J. Dynamics of sensitivity regulation in primate outer retina: the horizontal cell network. *J Vis* **3**, 513-526 (2003).

Lorach, H., Marre, O., Sahel, J. A., Benosman, R. & Picaud, S. Neural stimulation for visual rehabilitation: advances and challenges. *J Physiol Paris* **107**, 421-431 (2013).

Luo, D. G., Yue, W. W., Ala-Laurila, P. & Yau, K. W. Activation of visual pigments by light and heat. *Science* **332**, 1307-1312 (2011).

Mante, V., Frazor, R. A., Bonin, V., Geisler, W. S. & Carandini, M. Independence of luminance and contrast in natural scenes and in the early visual system. *Nat Neurosci* **8**, 1690-1697 (2005).

Najemnik, J. & Geisler, W. S. Simple summation rule for optimal fixation selection in visual search. *Vision Res* **49**, 1286-1294 (2009).

Neher, E. & Stevens, C. F. Conductance fluctuations and ionic pores in membranes. *Annu Rev Biophys Bioeng* **6**, 345-381 (1977).

Neitz, J. & Neitz, M. The genetics of normal and defective color vision. *Vision Res* **51**, 633-651 (2011).

Neumann, S., Vladimirov, N., Krembel, A. K., Wingreen, N. S. & Sourjik, V. Imprecision of adaptation in Escherichia coli chemotaxis. *PLoS One* **9**, e84904 (2014).

Nikonov, S., Engheta, N. & Pugh, E. N. J. Kinetics of recovery of the dark-adapted salamander rod photoresponse. *J Gen Physiol* **111**, 7-37 (1998).

Nikonov, S., Lamb, T. D. & Pugh, E. N. J. The role of steady phosphodiesterase activity in the kinetics and sensitivity of the light-adapted salamander rod photoresponse. *J Gen Physiol* **116**, 795-824 (2000).

Nirenberg, S. & Pandarinath, C. Retinal prosthetic strategy with the capacity to restore normal vision. *Proc Natl Acad Sci U S A* **109**, 15012-15017 (2012).

Pokorny, J. & Smith, V. C. Wavelength discrimination in the presence of added chromatic fields. *J Opt Soc Am* **60**, 562-569 (1970).

Pugh, E. N. J. & Lamb, T. D. Amplification and kinetics of the activation steps in phototransduction. *Biochim Biophys Acta* **1141**, 111-149 (1993).

Rebrik, T. I., Botchkina, I., Arshavsky, V. Y., Craft, C. M. & Korenbrot, J. I. CNG-modulin: a novel Ca-dependent modulator of ligand sensitivity in cone photoreceptor cGMP-gated ion channels. *J Neurosci* **32**, 3142-3153 (2012).

Rieke, F. & Baylor, D. A. Molecular origin of continuous dark noise in rod photoreceptors. *Biophys J* **71**, 2553-2572 (1996).

Rieke, F. & Baylor, D. A. Origin of reproducibility in the responses of retinal rods to single photons. *Biophys J* **75**, 1836-1857 (1998).

Rieke, F. & Baylor, D. A. Origin and functional impact of dark noise in retinal cones. *Neuron* **26**, 181-186 (2000).

Rieke, F. & Rudd, M. E. The challenges natural images pose for visual adaptation. *Neuron* **64**, 605-616 (2009).

Rovamo, J., Raninen, A. & Donner, K. The effects of temporal noise and retinal illuminance on foveal flicker sensitivity. *Vision Res* **39**, 533-550 (1999).

Rucci, M., Edelman, G. M. & Wray, J. Modeling LGN responses during free-viewing: a possible role of microscopic eye movements in the refinement of cortical orientation selectivity. *J Neurosci* **20**, 4708-4720 (2000).

Schnapf, J. L., Nunn, B. J., Meister, M. & Baylor, D. A. Visual transduction in cones of the monkey Macaca fascicularis. *J Physiol* **427**, 681-713 (1990).

Schneeweis, D. M. & Schnapf, J. L. The photovoltage of macaque cone photoreceptors: adaptation, noise, and kinetics. *J Neurosci* **19**, 1203-1216 (1999).

Schneeweis, D. M. & Schnapf, J. L. Noise and light adaptation in rods of the macaque monkey. *Vis Neurosci* **17**, 659-666 (2000).

Segall, J. E., Block, S. M. & Berg, H. C. Temporal comparisons in bacterial chemotaxis. *Proc Natl Acad Sci U S A* **83**, 8987-8991 (1986).

Sharpe, L. T., Stockman, A., Knau, H. & Jagle, H. Macular pigment densities derived from central and peripheral spectral sensitivity differences. *Vision Res* **38**, 3233-3239 (1998).

Shevell, S. K. *The Science of Color* (Elsevier, Oxford, UK, 2003).

Smith, V. C., Pokorny, J., Lee, B. B. & Dacey, D. M. Primate horizontal cell dynamics: an analysis of sensitivity regulation in the outer retina. *J Neurophysiol* **85**, 545-558 (2001).

Soo, F. S., Detwiler, P. B. & Rieke, F. Light adaptation in salamander L-cone photoreceptors. *J Neurosci* **28**, 1331-1342 (2008).

Stiles, W. S. Visual properties studied by subjective measurements on the colour-adapted eye. *Br Med Bull* **9**, 41-49 (1953).

Stiles, W. S. & Wyszecki, G. Colour-matching data and the spectral absorption curves of visual pigments. *Vision Res* **14**, 195-207 (1974).

Swarup, G. & Garbers, D. L. Stimulation of rhodopsin phosphorylation by guanine nucleotides in rod outer segments. *Biochemistry* **22**, 1102-1106 (1983).

Tranchina, D., Gordon, J. & Shapley, R. M. Retinal light adaptation--evidence for a feedback mechanism. *Nature* **310**, 314-316 (1984).

van Hateren, H. A cellular and molecular model of response kinetics and adaptation in primate cones and horizontal cells. *J Vis* **5**, 331-347 (2005).

van Hateren, J. H. & Lamb, T. D. The photocurrent response of human cones is fast and monophasic. *BMC Neurosci* **7**, 34 (2006).

van Hateren, J. H. & van der Schaaf, A. Independent component filters of natural images compared with simple cells in primary visual cortex. *Proc Biol Sci* **265**, 359-366 (1998).

Vroman, R. et al. Extracellular ATP hydrolysis inhibits synaptic transmission by increasing ph buffering in the synaptic cleft. *PLoS Biol* **12**, e1001864 (2014).

Vroman, R., Klaassen, L. J. & Kamermans, M. Ephaptic communication in the vertebrate retina. *Front Hum Neurosci* **7**, 612 (2013).

Wang, T. M., Holzhausen, L. C. & Kramer, R. H. Imaging an optogenetic pH sensor reveals that protons mediate lateral inhibition in the retina. *Nat Neurosci* **17**, 262-268 (2014).

Westheimer, G. Spatial frequency and light-spread descriptions of visual acuity and hyperacuity. *J Opt Soc Am* **67**, 207-212 (1977).

Yau, K. W., Matthews, G. & Baylor, D. A. Thermal activation of the visual transduction mechanism in retinal rods. *Nature* **279**, 806-807 (1979).

Yeh, T., Lee, B. B. & Kremers, J. The time course of adaptation in macaque retinal ganglion cells. *Vision Res* **36**, 913-931 (1996).

Younger, J. P., McCarthy, S. T. & Owen, W. G. Light-dependent control of calcium in intact rods of the bullfrog Rana catesbeiana. *J Neurophysiol* **75**, 354-366 (1996).

Zhaoping, L., Geisler, W. S. & May, K. A. Human wavelength discrimination of monochromatic light explained by optimal wavelength decoding of light of unknown intensity. *PLoS One* **6**, e19248 (2011).

Vita

Juan Manuel Angueyra Aristizábal was born in Bogotá, Colombia, son of Hernando Angueyra, anesthesiologist and Chantal Aristizábal, specialist in internal medicine. In 2006, Juan received his medical degree from the School of Medicine of Colombia's National University (Facultad de Medicina de la Universidad Nacional de Colombia), Bogotá, Colombia. He spent several summers in Woods Hole, MA working in a variety of invertebrate and prechordate photoreceptors, mentored by Enrico Nasi and Maria Gómez, and returned to Woods Hole in 2010 to attend the Neurobiology Summer Course and in 2011 as a teaching assistant for the same course. He received his doctorate in Physiology and Biophysics in August 2014.